

## ABSTRACT

STANO, KELLY LYNN. Optimizing CNT Array Growth and Functionalization for a Novel Method of CNT/Copper Composite Fabrication. (Under the direction of Dr. Philip Bradford.)

Carbon nanotubes (CNTs) are an attractive material for reinforcement in composites due to their advanced mechanical, electrical and thermal properties. While their integration into polymer matrix composites has been readily adopted and studied, techniques for producing metal matrix composites are lacking. Traditional metallurgical techniques can be complicated, time and energy consuming, and only modest property enhancement is achieved due to the inability to incorporate long, aligned, or dispersed CNTs. It is not uncommon for the resulting composite's properties to actually be degraded due to the insufficiencies of current processing routes. This thesis demonstrates a simple and novel processing route that results in the formation of a copper matrix composite with high mass fraction, two millimeter long, aligned CNTs as reinforcement.

A low-pressure chemical vapor deposition (LP CVD) reactor was designed and fabricated in-house which allowed for precise, digital control of experimental parameters during CNT synthesis, ensuring the minimization of unnecessary variability. Vertically aligned, CNT arrays were grown using a floating catalyst CVD method known as chlorine-mediated LP CVD. Rapid throughput of large-scale arrays was made possible due to the dual catalytic activity of iron(II) chloride, which rapidly dehydrogenates acetylene while also catalyzing CNT nucleation and growth. Experimental parameters were optimized to establish a growth procedure for the consistent growth of 2-millimeter tall, high quality arrays, which would be the precursor for reinforcement in CNT-reinforced copper nanocomposites.

The reinforcement efficiency of CNTs in composites is often limited by poor interfacial adhesion due to their low surface reactivity and non-wetting behavior. Atmospheric pressure plasma treatment using oxygen as an etchant was used to controllably functionalize the CNT arrays with polar compounds. In as few as 5 seconds, hydrophobic CNT arrays were made wettable with little to no permanent damage to the CNT walls or their vertical alignment. Analysis of the Raman spectra and contact angle as a function of time revealed that the effects of the plasma treatment could be reversed by exposure to atmosphere. Array hydrophobicity was completely recovered in 72 hours with negligible change from the original measured value.

To ensure the structural and dimensional stability of the CNT arrays during and after composite fabrication, the effect of amorphous carbon deposition was investigated. Amorphous carbon was shown to deposit conformally on individual CNTs. This resulted in the radial growth of their diameter, as well as mechanical enhancement. The compressive strength of treated arrays increased significantly as a function of increasing deposition times. CNT arrays treated in excess of 5 minutes were found to exhibit foam-like recovery upon removal of the compressive load.

To fabricate the composites, heated, super-saturated solutions of copper nitrate, sulfate and chloride were prepared. The post-treated arrays were infiltrated with solution and slowly dried. The salt-CNT composites were then dehydrated and heated in hydrogen to reduce the copper compounds to pure, metallic copper. Depending on the precursor, copper was found to nucleate into nanoparticles or deposit as thin-film coatings on the CNT surfaces. The resulting copper content varied as a function of the salt precursor's solubility in aqueous solution. Additionally, increasing the length of amorphous carbon deposition yielded higher Cu content due to increased dimensional stability of the array. This prevented array shrinking and leaching-out of the copper salt solution. CNT concentrations ranged from 7 - 15 wt%. The compressive strength of CNT-Cu composites was also shown to generally increase as a function of Cu content.

© Copyright 2012 by Kelly Lynn Stano  
All Rights Reserved

Optimizing CNT Array Growth and Functionalization for a Novel Method of CNT/Copper  
Composite Fabrication

by  
Kelly Lynn Stano

A thesis submitted to the Graduate Faculty of  
North Carolina State University  
in partial fulfillment of the  
requirements for the degree of  
Master of Science

Textile Engineering

Raleigh, North Carolina  
2012

APPROVED BY:

---

Dr. Russell Gorga

---

Dr. Yuntian Zhu

---

Dr. Philip Bradford  
Committee Chair

## **BIOGRAPHY**

Kelly Lynn Stano was born in Anchorage, Alaska on June 26, 1987 to Gene and Lynn Stano. She is the older of two children, having a younger sister, Megan. In 1995, Kelly's family moved to Little Switzerland in the mountains of North Carolina where she spent her childhood. After graduating from Mitchell High School in 2005, she enrolled at North Carolina State University to pursue a degree in Textile Engineering. In the fall of her freshman year, Dr. Russell Gorga sponsored her submission for an Undergraduate Research Award, which she won the following spring. This began a three-year tenure where she worked with many aspects of the electrospinning process in the development of polymer-carbon nanotube composite nanofibers.

In 2007, Kelly had the opportunity to travel abroad to the University of Cambridge as a Visiting Scientist where she worked in the Macromolecular Materials Group, lead by Professor Alan Windle. While there she studied the mechanical properties of carbon nanotube fibers formed via their continuous spinning technique. It was here that her fascination for carbon nanotubes was fueled, as was her desire to attend graduate school. It was also during this time that she traveled to Montpellier, France to the NT08 conference where she met Sumio Iijima, the man often credited with "discovering" the carbon nanotube!

In the summer of 2010 after receiving her B.S. in Textile Engineering, she began work in the Carbon Nanotube Textile Group under the direction of Dr. Philip Bradford at North Carolina State University. Here, she rounded out her carbon nanotube experience to help develop, build and optimize a growth reactor. With Dr. Bradford's encouragement, Kelly applied for the National Science Foundation's Graduate Research Fellowship with a proposal on carbon nanotube - ceramic matrix composites. In late 2011, she was notified that she had been awarded the prestigious fellowship to continue her work under Dr. Bradford while pursuing a dual PhD in Materials Science and Engineering and Fiber and Polymer Science.

## ACKNOWLEDGMENTS

The culmination of this work would not have been possible without the support, advice and guidance of so many. I am sincerely grateful to my advisor, Dr. Philip Bradford, for providing me with this opportunity to develop as a researcher and a hopeful academic. I am so thankful for your enthusiasm and unwavering support through the ups and downs that are research.

I am also thankful for Dr. Bradford's excellent selection of group members. I could not have picked a better lab mate than Can Tang to spend all those long hours in the lab with. I am also delighted to have been able to work with Murphy Carroll over the last year. Your hard work and attention to detail was invaluable to the success of this research. I would also like to thank all of my lab members: Can, Murphy, Ozkan, Shaghayegh, Hardik, James, Omar and Victor. You all are so great; I've decided to stay 3 more years!

I would like to thank Dr. Russell Gorga, who got me started in this whole research-gig. You are a brilliant teacher and mentor, and a role model for my own teaching aspirations. Many thanks to Seth McCullen as well, for your excellent mentorship at the start of my research career, and unfailing support ever since. I would also like to thank Dr. Yuntian Zhu for serving on my committee. He and his lab group have been invaluable resources throughout this work.

There are several individuals whose assistance made this work possible, if not more enjoyable along the way. I would like to thank Josh Nowak for coming in early, even on Saturdays, to conduct 5 second long plasma treatments. You are a saint. Thank you to Dr. Marian McCord as well for allowing me to use the plasma equipment. Thanks to Chuck Mooney, Dale Batchelor, Fred Stevie, Roberto Garcia, and the rest of AIF for their characterization expertise. You all say my samples are really cool to look at, but even if you are paid extra to say that to weary graduate students, I appreciate it nonetheless. I would like to thank Dr. Julie Willoughby, Birgit Anderson, and Judy Elson for the use of and training on their equipment. Sincere thanks to Dr. Rust and the TECS department for investing in my education and development as a researcher.

Thank you, Tyler, for your unconditional love and support. I owe special thanks to my friends, Sarah, Karen, Richard, Jordan...the last two years would have been pretty boring without you all. Thank you to my thesis-writing companion, Sasha Ormond.

Finally I would like to thank my family, especially my Mom, Dad, and sister. You all got me to where I am today, and I cannot thank you enough for your love, support, funny jokes, cute pictures of kittens and puppies...I love you guys.

# TABLE OF CONTENTS

<b>LIST OF TABLES.....</b>	<b>vi</b>
<b>LIST OF FIGURES.....</b>	<b>vii</b>
<b>1 Introduction.....</b>	<b>1</b>
<b>2 Literature Review .....</b>	<b>3</b>
2.1 Carbon Nanotube Properties .....	3
2.2 Carbon Nanotube Synthesis .....	5
2.2.1 Chemical Vapor Deposition .....	5
2.3 Carbon Nanotube Reinforced Composites.....	10
2.3.1 Carbon Nanotube - Metal Matrix Composites .....	12
2.3.2 Processing Routes for Carbon Nanotube - Copper Matrix Composites.....	14
2.4 Copper and Copper Compounds .....	34
2.4.1 Copper(II) Sulfate.....	36
2.4.2 Copper(II) Nitrate.....	39
2.4.3 Copper(II) Chloride.....	42
2.5 Wetting & Surface Tension.....	45
2.5.1 Wetting Behavior of Rough Surfaces.....	45
2.5.2 Controlling the Wetting Behavior of Carbon Nanotube Arrays.....	46
<b>3 Experimental.....</b>	<b>52</b>
3.1 Equipment Preparation.....	52
3.1.1 Construction of Low Pressure Chemical Vapor Deposition Reactor .....	52
3.1.2 Establishing Growth-Run Procedure .....	53
3.1.3 Growth Parameter Optimization.....	56
3.2 Material Preparation.....	57
3.2.1 Carbon Nanotube Array Growth .....	57
3.2.2 Post-Treatments .....	58
3.2.3 Processing of Copper Salts.....	59
3.2.4 Carbon Nanotube - Copper Composite Fabrication .....	60
3.3 Material Characterization.....	61
3.3.1 Chemical Structure Analysis .....	61
3.3.2 Micro-Structural Analysis .....	61
3.3.3 Thermal Properties Analysis .....	62
3.3.4 Mechanical Analysis.....	62
3.3.5 Wetting Properties Analysis .....	62

<b>4</b>	<b>Controlling the Wetting Behavior of Carbon Nanotube Arrays.....</b>	<b>63</b>
4.1	Background .....	63
4.2	Experimental Procedure .....	64
4.3	Results and Discussion.....	65
4.3.1	Achieving Array Wettability .....	65
4.3.2	Effect of Treatments on Carbon Nanotube and Array Structure .....	69
4.3.3	Effect of Time on Array Wetting Properties .....	75
4.4	Conclusions .....	78
<b>5</b>	<b>Method for Fabrication of High Mass Fraction, Aligned Carbon Nanotube - Copper Composites .....</b>	<b>79</b>
5.1	Background .....	79
5.2	Experimental Procedure .....	81
5.3	Results and Discussion.....	82
5.3.1	Effect of Amorphous Carbon Deposition on Composite Fabrication .....	84
5.3.2	Compression Properties of CVD Post-Treated Arrays and Cu-CNT Composites .....	89
5.3.3	Chemical Validation of Powdered Salt Reduction to Copper .....	93
5.3.4	Copper Content Based on Salt Properties.....	94
5.4	Conclusions .....	103
	<b>REFERENCES .....</b>	<b>105</b>
	<b>APPENDIX.....</b>	<b>115</b>
	Appendix A. Chemical Structure Validation of Copper(II) Sulfate and Copper(II) Chloride using Energy Dispersive Spectroscopy (EDS).....	116

## LIST OF TABLES

<b>Table 2.1</b>	Measured physical properties of hydrated and anhydrous forms of copper sulfate, chloride and nitrate [70], [71]. .....	36
<b>Table 5.1</b>	The measured physical properties of CNT-Cu composites during fabrication from copper nitrate solution. Four samples were tested to compare effectiveness of amorphous carbon deposition in maintaining CNT array stability during processing. ....	88
<b>Table 5.2</b>	The density and maximum specific stress were calculate for each CNT array and CNT-Cu composites to determine the affect of amorphous carbon deposition duration. ....	92
<b>Table 5.3</b>	Measured and calculated values for determination of theoretical and actual copper content based on salt precursor. ....	96
<b>Table 5.4</b>	Physical parameters used in copper content calculation. ....	97

## LIST OF FIGURES

<b>Figure 2.1</b>	Number of publications on polymer, ceramic and metal matrix - CNT composites from 1997 to 2007 (taken from Bakshi et al [34])......	11
<b>Figure 2.2</b>	Number of publications on different metal matrix-CNT composites from 1997 to 2007 (taken from Bakshi et al. [34]). .....	12
<b>Figure 2.3</b>	Increasing the volume fraction of CNTs in Cu results in changes in composite A) hardness and porosity and B) coefficient of friction (taken from Tu et al. [39]). .....	15
<b>Figure 2.4</b>	A) Micrograph showing the pull out length of Ni-coated SWNTs in a copper matrix on a tensile test fracture surface, and B) the thermal and electrical conductivities of many common electrical contact materials (taken from C. Kim et al. [42]). .....	16
<b>Figure 2.5</b>	High-energy ball milled composites do not exhibit a homogenously dispersed CNTs, instead forming A) two distinct phases, and B) two separate yield strengths (taken from Kim et al. [43]). .....	17
<b>Figure 2.6</b>	The microhardness and grain size of CNT reinforced Cu composites was enhanced and consistent across the surface of the samples (taken from Li et al. [44])......	19
<b>Figure 2.7</b>	A) Table of thermal resistance values for control CNT film and CNT-Cu composite samples and, B) SEM micrographs of composite samples before and after compressive thermal resistance measurement (taken from Ngo et al. [46]). .....	21
<b>Figure 2.8</b>	SEM images of SWNT buckypaper-Cu nanoparticle bi-layer composites containing A) 31 wt% Cu; B) 39 wt% Cu (taken from Ferrer-Anglada et al. [48])......	22
<b>Figure 2.9</b>	A) Schematic of thermal management component architecture with integrated Cu-CNT composite; B) process flow for fabricating CNT via structure; C) electrical and thermal resistance as a function of copper content; SEM images of D) CNT via; and E) and F) Cu-CNT composite vias with different copper loadings (taken from Chai et al. [49]). .....	23
<b>Figure 2.10</b>	A) Crystallite size and micro-strain of SWNT-Cu composites; B) dependence of electrical resistivity of SWNT-Cu composites and pure Cu and; C) micro-hardness of SWNT-Cu composites (taken from Yang et al. [50])......	24
<b>Figure 2.11</b>	Schematic process for Cu-MWNT composite fabrication method using pulse-reversed electrodeposition (taken from Arai et al. [52]). .....	25
<b>Figure 2.12</b>	Physical properties of composites produced with electroless plated CNTs including A) electrical conductivity; B) hardness; C) stress-strain and; D) elastic modulus and yield strength (taken from Daoush et al. [53]). .....	27
<b>Figure 2.13</b>	A) Schematic depicting the functionalization of CNTs and dissociation of Cu salts onto CNT surfaces and; B) TEM micrograph and schematic of CNT/CuO powder showing implantation of CNT within CuO particles (taken from Cha et al. [54])......	28

<b>Figure 2.14</b>	Mechanical properties of CNT-Cu composites formed via molecular level mixing: A) stress-strain curves of CNT-Cu composites obtained by compression testing and; B) yield strength and Young’s modulus of CNT-Cu composites with increasing concentration of CNTs (taken from Cha et al. [54]). .....	29
<b>Figure 2.15</b>	Schematic of modified molecular level mixing procedure, which utilizes gelatin wrapping to “lock” copper ions onto the CNT surface (taken from Xu et al. [56])....	30
<b>Figure 2.16</b>	A) SEM image of CNT/Cu nanocomposites; B) EDX spectrum where the electron beam was focused on areas a, b, and c; C) TEM image showing the embedded CNT in Cu matrix and; D) FTIR spectrum for CNT/CuO and CNT/Cu powders (taken from Kim et al. [57]). .....	32
<b>Figure 2.17</b>	In aqueous solution, Cu <sup>2+</sup> ions form an octahedral metal aquo complex with six water molecules.....	34
<b>Figure 2.18</b>	The dehydration/decomposition (left) and reduction (right) profiles of hydrated copper sulfate salts (taken from Hegedus et al. [77]). .....	38
<b>Figure 2.19</b>	Metallic copper film thickness as a function of deposition temperature and duration of hydrogen pulse (taken from Martensson et al. [97]). .....	44
<b>Figure 2.20</b>	A) FTIR spectra of MWNT arrays with various degrees of oxidation showing oxygen-containing functional groups; B) high-resolution XPS spectra of C 1s peak of UV/ozone treated MWNT array (taken from Aria et al. [113]). .....	49
<b>Figure 2.21</b>	A) XPS survey scan of as-grown and treated vertically aligned CNT arrays; B) high-resolution XPS C 1s peak of as-grown and plasma treated vertically aligned CNT arrays and; C) Raman spectra of pristine and treated arrays (taken from Ramos et al. [116]). .....	51
<b>Figure 3.1</b>	Picture of low-pressure chemical vapor deposition reactor built in-house for chlorine-mediated carbon nanotube synthesis. ....	52
<b>Figure 4.1</b>	The change in static contact angle as a function of thermal oxidation treatment. Lower contact angles are measured for samples treated at higher temperatures and longer durations. Absence of a data point for a particular time and temperature indicates that wetting occurred. ....	66
<b>Figure 4.2</b>	Static contact angles were measured for thermally oxidized and plasma treated CNT arrays. Wetting was achieved at temperatures of 575°C and 600°C, but not at 550°C. Plasma treating CNTs for 5 seconds yielded wettable arrays. ....	66
<b>Figure 4.3</b>	XPS was used to detect chemical changes in CNT arrays before and after treatment: A) 575°C for 30 minutes; B) 600°C for 10 minutes and; C) atmospheric oxygen plasma for 5 seconds. Oxygen was detected for both thermally treated samples, but not for the plasma treated sample. ....	67
<b>Figure 4.4</b>	High-resolution XPS scans of the O 1s peaks for the thermally treated samples show the presence of C=O (531 eV) and surface adsorbed CO (536.5 eV) on the CNT arrays. ....	68
<b>Figure 4.5</b>	EDS spectra of vertically aligned CNT array after plasma treatment shows an increased concentration of oxygen compared to a pristine sample. ....	69

<b>Figure 4.6</b>	Low and high magnification (left and right, respectively), SEM images of the top surface of CNT arrays: A,B) untreated; C,D) 575°C for 30 minutes; E,F) 600°C for 10 minutes and; G,H) atmospheric oxygen plasma for 5 seconds. ....	70
<b>Figure 4.7</b>	Raman spectra were taken for all thermally oxidized samples to analyze the changes in CNT structure. The average $G_1/D_1$ ratio generally decreases as a function of temperature and treatment time. ....	71
<b>Figure 4.8</b>	The kinetics of the oxidation of several carbon compounds were studied by monitoring the $CO_2$ evolution profile as a function of temperature (taken from Brukh et al. [124]). ....	72
<b>Figure 4.9</b>	Thermogravimetric analysis (TGA) was used to compare mass loss as a function of treatment temperature (550, 575 and 600°C), and time. ....	73
<b>Figure 4.10</b>	Raman spectra were taken for all plasma treated samples to determine the effect of treatment time on CNT structure. A virtually constant $G_1/D_1$ ratio signifies no change in defect density. ....	74
<b>Figure 4.11</b>	Raman spectra were collected to compare average $G_1/D_1$ ratios for all treatments that successfully yielded a wettable CNT array. ....	75
<b>Figure 4.12</b>	CNT array wettability achieved via plasma treatment will last for 72 hours if left exposed to atmosphere. The measured contact angle after 72 hours was 143°, only 3° lower than the pristine array before treatment. ....	76
<b>Figure 4.13</b>	Raman spectra taken before plasma treatment (horizontal grey line), are compared to spectra taken after treatment as a function of time. The $G_1/D_1$ ratios increase linearly over 72 hours, when hydrophobicity was restored to the array. ....	77
<b>Figure 4.14</b>	Raman spectra taken before thermal oxidation treatment (horizontal grey line), are compared to spectra taken after treatment as a function of time. The $G_1/D_1$ ratios remain unchanging after 72 hours of testing. ....	77
<b>Figure 5.1</b>	Pristine and CVD post-treated arrays were dipped in pure DI water to show the effects from surface tension and capillary forces on the physical morphology of the sample. Both samples were destroyed by capillary drying forces. ....	83
<b>Figure 5.2</b>	After amorphous carbon CVD an opaque black film formed on the inner and outer tube walls of the LP CVD reactor (A). Analysis of the Raman spectrum of the film scraped from the tube wall revealed the presence of graphitic C-C bonding (B). ....	84
<b>Figure 5.3</b>	Cross-section SEM micrographs of A) pristine CNT array and, B) CNT array with 30 minutes of CVD amorphous carbon deposition. ....	85
<b>Figure 5.4</b>	Linear relationships between mass of deposited amorphous carbon (left axis) and array density (right axis) as a function of treatment duration. ....	86
<b>Figure 5.5</b>	Raman analysis of CNT post-treated arrays as a function of deposition time. The ratio of graphitic signal to disorder ( $G_1/D_1$ ), decreased from 1.99 for a pristine array to 0.97 for an array treated for 60 minutes. ....	86
<b>Figure 5.6</b>	CNT arrays with varying amounts of amorphous carbon deposition: A) 60 min; B) 30 min; C) 5 min and; D) 0 min (pristine array), after dipping in supersaturated copper(II) nitrate - DI water solution. ....	87

<b>Figure 5.7</b>	The effect of amorphous carbon deposition is evident throughout all steps of composite fabrication: wetting, drying, dehydration, and reduction. ....	88
<b>Figure 5.8</b>	An Instron operating in compression mode was used to measure the mechanical properties of arrays treated with amorphous carbon as well as Cu-CNT composites. ....	89
<b>Figure 5.9</b>	Values for density were calculated based on array volume and weight after CVD treatment and composite fabrication. Array density varied as a function of CVD treatment time and copper content. ....	90
<b>Figure 5.10</b>	The compression properties of CNT arrays treated were measured as a function of A) amorphous carbon deposition time, and B) combined amorphous carbon deposition and copper content. ....	90
<b>Figure 5.11</b>	Comparison of compression stress-strain curves for CNT arrays with and without copper and amorphous carbon. ....	92
<b>Figure 5.12</b>	EDS spectra and accompanying SEM micrograph insets for the three processing steps for copper(II) nitrate: A) hydrated salt, B) copper oxide, and C) metallic copper. ....	94
<b>Figure 5.13</b>	Copper composites were fabricated using a modified molecular level mixing processing route using $\text{Cu}(\text{NO}_3)_2$ , $\text{CuSO}_4$ , and $\text{CuCl}_2$ as precursors. Images were taken after drying (left), and hydrogen reduction (right). ....	95
<b>Figure 5.14</b>	A Cu-CNT composite made from copper(II) nitrate was characterized with SEM. Micrographs show A) cross-section with low magnification inset and; B) top surface. ....	98
<b>Figure 5.15</b>	A Cu-CNT composite made from copper(II) sulfate was characterized with SEM. Micrographs show A) cross-section with low magnification inset and; B) top surface. ....	98
<b>Figure 5.16</b>	A Cu-CNT composite made from copper(II) chloride was characterized with SEM. Micrographs show A) cross-section with low magnification inset and; B) top surface. ....	99
<b>Figure 5.17</b>	SEM micrograph taken using a back-scattered electron (BSE) detector. Bright areas correspond to high Z elements (copper), while low contrast corresponds to low Z elements (carbon). ....	100
<b>Figure 5.18</b>	SEM micrographs of A) large copper structure with highlighted areas of copper coated CNTs and CNT bundles, and B) fibrous copper-CNT structures. ....	101
<b>Figure 5.19</b>	EDS spectra taken from the top surfaces (A, C, E) of each composite (nitrate, sulfate and chloride) were used to confirm the presence of pure copper. Additionally, spectra were taken from the cross-section (B, D, F) at the top, middle and bottom of each sample to probe the relative distribution of copper throughout the thickness of the composite. ....	103

# 1 Introduction

Contrary to popular belief, the existence of carbon nanotubes (CNTs) predates the 20<sup>th</sup> century by millennia. In fact, scientists have found naturally occurring CNTs in prehistoric glacial samples [1] and also synthetically produced CNTs in the tail pipes of cars [2]. The first evidence of their formation in a controlled environment dates back to the 1950s [3], [4] and 1970s [5], [6], but the microscopy capabilities for imaging these revolutionary particles were limited. Following Iijima's infamous characterization of the “helical microtubules of graphitic carbon” in 1991 there has been an explosion of research activity [7]. Since then, interest in this field has grown exponentially, with 7000 papers being published in 2006 alone [8]. The reason for the intense activity stems from the extraordinary physical properties of CNTs. Not only do they exhibit great strength, stiffness and toughness [9–11], but they also possess metal-like electrical conductivity [12], [13], and thermal conductivity superior to metals [14], [15]. All of this combined with their ultra-low density makes CNTs an attractive reinforcement in composite matrices for a wide variety of applications.

The realization today however, is that CNTs have not yet begun to demonstrate their full potential in terms of material enhancement. The causes of this shortcoming lie in the difficult tasks of CNT production as well as processing. In order for CNTs to be a viable reinforcement in composite materials, a synthesis method that rapidly produces massive quantities of high-quality CNTs must be used. With their large aspect ratios, CNTs exhibit high anisotropy of physical properties along their axis. Therefore, this growth method must also be capable of producing long, vertically aligned arrays for their properties to be best utilized. The benefit of using arrays in composites is two-fold in that it also addresses the issues of bundling and agglomeration, which are common in all areas of CNT processing. Relative to CNT powders, there is great potential for the use of aligned CNT arrays as a reinforcement phase in composites, but there is also a shortage of work in this area. This thesis describes research relating to the synthesis and functional enhancement of CNT arrays, as well as the development of composite fabrication techniques utilizing the arrays while maintaining their delicate alignment and superior physical properties.

In Chapter 3, a relatively new growth method for rapidly producing large-scale quantities of aligned CNT arrays is explored and optimized. A custom low-pressure chemical vapor deposition reactor was designed and fabricated in-house to allow for superior parameter control and monitoring. To accompany the reactor, detailed lab and growth procedures were developed to ensure that all

possible sources of variation were kept to a minimum while allowing maximum customization of experimental parameters. A thorough characterization of produced CNT arrays is also reported.

Pristine CNT arrays must be treated post-growth in order to best prepare them for eventual incorporation into composite materials. Without post-treatment CNT arrays are fragile and difficult to wet due to their high surface roughness. In the field of composites, mutual wetting of phases is crucial for establishing an effective interface for energy transfer. In Chapter 4, methods for manipulating the surface properties of the CNT arrays to allow for wetting were investigated. Various procedures for creating hydrophilic arrays are demonstrated and characterized to determine the side effects on CNT structure.

Many researchers have sought to develop CNT-enhanced copper materials for thermal management applications. The synergistic effects of these two materials working together has great potential, but has found limited success. Traditional metallurgical processing techniques for producing metal matrix composites do not address the common issues in CNT composite fabrication: agglomeration and bundling, poor alignment, low volume fractions, and poor interfacial adhesion. Chapter 5 outlines a novel processing route for the production of large-scale, aligned CNT-copper nanocomposites. Utilizing aqueous copper salt solutions, the arrays were infiltrated and then reduced to leave behind pure copper throughout the array structure. The process was optimized for maximum copper incorporation while enhancing the stiffness and compressive properties of the CNT arrays. The chemical, morphological and structural properties of the produced composites were fully characterized and evaluated.

## 2 Literature Review

### 2.1 Carbon Nanotube Properties

Carbon nanotubes (CNTs) are widely regarded as being a material that will change the face of an untold number of technologies. Researchers studying catalysis, composites, tissue engineering, energy harvesting and storage, nanofluidics and even sensors for detecting the ripeness of fruit have been inspired by their superior physical properties and recognize their impact potential.

The superior properties of CNTs can be directly extracted from chemical structure and bonding. The carbon atom, with an electron configuration of  $1s^2 2s^2 2p^2$ , has four valence electrons in its available for bonding. When two atoms' electrons come sufficiently close and are mutually stabilized, covalent bonding will occur. This bonding can take several forms, dependent on whether these electrons occupy the  $sp^3$  (diamond),  $sp^2$  (graphite), or  $sp$  (acetylene) orbital. In the case of graphite, an electron from the 2s shell is promoted to and combined with two of the 2p orbitals to form three  $sp^2$  orbitals and one unhybridized, delocalized p orbital. The three  $sp^2$  orbitals are in the same plane with an equal spacing of  $120^\circ$  between them, and the p orbital is situated perpendicular to the plane.

Each  $sp^2$ -hybridized atom combines with three other  $sp^2$ -hybridized carbon atoms, thus forming the familiar hexagonal arrangement in parallel planes. The delocalized  $\pi$  electrons can readily move from one side of the plane to the other, but cannot move between adjacent planes. These delocalized electrons are what account for the enhanced electrical and thermal conductivity of graphite over diamond, which is electrically insulating and has four  $\sigma$  bonds. This is also the basis for the anisotropy of physical properties that is seen in  $sp^2$ -bonded materials. The covalent bonds formed between the atoms are strong due to the large amount of overlap allowed by the lopsided-shaped  $sp^2$  orbital, and also due to the small size of the carbon atom.

Rolled sheets of  $sp^2$ -bonded graphite comprise CNTs. Whereas graphite planes have perfectly symmetrical  $\pi$  delocalization, the rolled morphology exhibited in CNTs causes the  $\pi$  orbitals to deform, due to quantum confinement. This causes rehybridization of  $sp^2$  towards  $sp^3$ , thus delocalizing the electrons outside the tube surface even more. This is what gives CNTs their enhanced electronic, thermal and reactive properties over graphite.

One cylinder makes a single walled nanotube (SWNT), two concentric rolls are known as double walled nanotubes (DWNTs), while three or more are called multiwalled nanotubes (MWNTs). Between walls there is  $3.4 \text{ \AA}$  of free space, which is characteristic of graphite plane spacing. The

number of walls has some effect on the resulting physical properties. Due to the decreased likelihood for bonding defects, SWNT and DWNTs generally have more desirable properties, though realistically they are more difficult to produce and process.

One additional parameter that can influence the properties of CNTs is their rolling structure, or chirality. The chirality of a CNT can be identified by a set of two integers ( $n, m$ ) that correspond to graphite vectors. By rolling the graphite sheet in different directions, different nanotubes can be obtained: zigzag ( $n>0, m=0$ ), armchair ( $n=m$ ), or chiral ( $n>m>0$ ). Zigzag and chiral tubes are both semiconductors while armchair are metallic. This is attributed to the highly regular quantum confinement and thus electron delocalization exhibited by armchair CNTs. Until recently, little was understood about how to control the chirality of CNTs. There has been some recent success in the synthesis of armchair (thus metallic) SWNTs [16], [17]. There is little extrapolation of this work to the growth of MWNTs because of their added complexity of many walls. Due to the mixed chirality of the concentric walls, MWNTs are semiconducting.

Due to the highly regular structure of CNTs and their small size, they exhibit ballistic conduction of electrons along their length. Very small concentrations of CNTs can be added to non-conducting matrices to achieve percolation, thus enhancing electrical conductivity. Additionally, due to their high thermal conductivity, increasing heat does not as drastically affect the electronic transport properties as it would in other conductors.

Though difficult to achieve experimentally, theoretical calculations predict values for thermal conductivity as high as 6000 W/mK [15]. This result is due to a combination of factors: 1) the high axial stiffness allows for a high velocity of phonon modes, 2) the highly confined 1D structure restricts the space for phonon-phonon (Umklapp) collisions, and 3) the highly perfect atomic structure minimizes the likelihood of elastic phonon scattering due to defects. Because the conduction mechanism is lattice and vibration based as opposed to metals that rely on valence electrons to transfer heat energy, the thermal conductivity of CNTs does not significantly degrade with increasing temperature. Additionally, due to the potential for dual conduction mechanisms, there is significant interest in developing a CNT-Cu composite material for advanced heat dissipation. This topic will be discussed in greater detail in Section 2.3 of this thesis.

As mentioned before, the superior strength and stiffness of CNTs is derived from the strength of the carbon-carbon covalent bond, as well as the highly regular and symmetric structural morphology, which reduces the potential for stress concentrations. This is of course assuming a perfect, defect free CNT, but some physical experiments have actually probed individual CNTs. By

analyzing the thermal vibrations of a single cantilevered MWNT the Young's modulus was measured to be 1.0 to 1.8 TPa [9]. A more realistic test that actually pulled and bent individual CNTs yielded more conservative values. The modulus and strength were measured to be 0.8 and 150 GPa respectively [18]. MWNTs are considered to be weaker in tension compared to SWNTs because of slippage and pullout of the concentric walls, but due to their relative ease of synthesis, they are generally the reinforcement of choice for composites researchers.

## **2.2 Carbon Nanotube Synthesis**

There are many methods by which carbon nanotubes can be grown, and depending on the desired application there are benefits to each method. Arc discharge and laser ablation tend to produce CNTs with fewer structural defects. A result of this is very consistent material that has predictable properties as well as great structural integrity. On the other hand, metal catalyzed chemical vapor deposition (CVD) is capable of producing large quantities of CNTs, though they may not be as pristine as those grown by other methods. As CVD is the method used in this research, the details of the method will be discussed further.

### ***2.2.1 Chemical Vapor Deposition***

Chemical vapor deposition (CVD) is a highly utilized synthesis technique in modern industrial and research processes. It has been around for over a century, with its pioneering application to improve the strength of incandescent bulb filaments through carbon or metal coatings [19]. Since then it has found many applications in an array of disciplines due to its ability to deposit a variety of materials including metals, non-metals like carbon and silicon, and even carbides, nitrides and oxides.

In short, CVD involves a series of physical and chemical steps that result in the deposition of a solid material onto a solid surface. In all processes, temperature and pressure are crucial parameters that must be closely monitored and controlled throughout growth. Understanding the physical mechanisms of CVD requires knowledge of many fundamental disciplines such as thermodynamics, chemistry, fluid dynamics and kinetics. The CVD process can be explained by a series of events: 1) Reactant gases enter the reactor via forced flow, 2) gases diffuse through the boundary layer, 3) gases come into contact with the surface of the substrate, 4) deposition reaction takes place on the surface of the substrate, and 5) gaseous by-products of the reaction are diffused away from the surface, back

through the boundary layer. Nearly all CVD methods use a quartz tube and tube furnace as the reactor. The furnace must have precise temperature control over a considerable length of the tube. The method can be used at atmospheric or low pressure, and the method will dictate the nature of the set-up. Mass flow controllers are used to precisely monitor and control the flow of growth and reactive gases.

In this process, deposition of solid material occurs as a result of a chemical reaction, which takes place in the vapor phase. The possible types of chemical reactions are as varied as the materials the CVD process can produce. They include thermal decomposition or pyrolysis, reduction, hydrolysis and many others. In the case of CNT synthesis, the pertinent chemical reactions are generally thermal decomposition of hydrocarbons or disproportionation of carbon monoxide, although there are many other less prominent methods. The latter is primarily used for the synthesis of SWNTs and will not be discussed in this review of literature.

#### *2.2.1.1 Chemical Vapor Deposition of Carbon Nanotubes and Arrays*

As previously mentioned, CNT of CNTs is unique because it allows for controlled or patterned growth of various CNT structures. In a typical growth run a substrate (usually silicon or quartz), is loaded into a quartz tube and the system is purged to remove atmospheric impurities. Then the furnace is ramped to a desired temperature, at which point the carbon feedstock is flowed into the system to react with a catalyst. The reaction is allowed to continue for the desired amount of time. Then the tube is once again purged to remove leftover growth gases, and cooled to room temperature. Catalysts that can be used for CNT synthesis include Fe, Ni, Co and Mo. Common carbon sources include CO, methane, ethane, acetylene and ethylene.

There are two types of catalyst systems used in thermal CVD of CNTs - supported catalyst and floating catalyst. In the supported catalyst method, a reactive catalyst layer is pre-deposited on the growth substrate using evaporation, magnetron or ion-beam sputtering, or pulsed laser deposition. Although the layers are applied as thin films (< 20nm), they form small particles due to surface tension at elevated temperature. There are correlations between the film thickness and particle size, with thinner films yielding smaller particles, and thus smaller diameter CNTs [20], [21]. The introduction of a non-reactive "buffer layer" between the catalyst and substrate can also have an effect on the catalyst particle size [22]. At elevated temperatures solid solutions or alloys of the catalyst and non-catalyst layers will form surface clusters with many small reactive sites for CNT growth. Materials that have been demonstrated as effective buffers include Al, Ir, Ti, Ta, and W [23].

Floating catalyst CVD is thought to be a viable route for the scale-up of CNT growth because it allows for the continuous feeding of catalyst particles or compounds through the feedstock. Sen et al. [24], first demonstrated this method with the pyrolysis of benzene in the presence of metallocenes such as ferrocene, cobaltocene, and nickelocene to form MWNTs. At high temperature the metallocene vaporizes to leave behind metal nanoclusters. The size of the cluster will ultimately depend on the thermodynamic conditions inside the reactor. Smaller clusters are unstable and will quickly evaporate while larger ones will break apart until an equilibrium size has been met [25]. Control and understanding of this method is limited, but tunable process parameters include temperature and residence time, which is influenced by gas flow rate and feedstock injection rate.

A typical growth using either catalyst approach would result in the synthesis of a tangled web of carbon nanotubes, each extending from its respective catalyst particle. As an individual CNT grows longer, it can no longer support its own weight without buckling and falling over. Alternative morphologies, such as vertically aligned forests, are possible however. Just as the thickness of the catalyst and buffer layers affects particle size, it also affects the nucleation density and spacing of the particles on the substrate. At an optimized spacing the CNTs will grow upward and be mutually supported by surrounding CNTs, preventing them from falling back onto the substrate. The resulting structure can grow millimeters tall before termination, and has a variety of properties that make it an attractive material for researchers.

Due to their aligned nature, arrays can be processed in unique ways to alleviate some common issues in their utilization. In this morphology, the array is relatively fixed so that the anisotropic properties can be exploited without losing alignment. For example, arrays can be infiltrated with liquids [26] or polymers [27] while still in their aligned state. This greatly reduces the propensity of the CNTs to agglomerate and form bundles. This in turn allows for the fabrication of high volume fraction composites. Only in high concentrations will the potential of CNTs become a reality. More recently, CVD methods have been developed which allow for one-step growth of larger samples [28]. In chlorine mediated CVD (CM-CVD), the time-involved steps of buffer and catalyst layer deposition are replaced with a one step method. As this is the specific synthesis method used, it will be discussed in greater detail below.

#### *2.2.1.2 Chloride Mediated Chemical Vapor Deposition of Carbon Nanotube Arrays*

Chlorine-mediated chemical vapor deposition is more closely related to floating catalyst CVD than supported catalyst. The catalyst, iron(II) chloride ( $\text{FeCl}_2$ ), reacts directly with the carbon source

in the gaseous phase. This can be completed at relatively low temperatures (500°C), which is below the thermal decomposition temperature of FeCl<sub>2</sub>.

The first instance of FeCl<sub>2</sub> being used for CNT growth was in 2004 [29], although iron(III) chloride was used as a floating catalyst for large-scale, aligned CNT growth previously [30]. FeCl<sub>2</sub> has also been used as a catalyst for the growth of "moustache-like" carbon fibers [31]. In this experiment FeCl<sub>2</sub> powders were heated to 500°C in argon. After 15 minutes, acetylene was introduced in the chamber and allowed to react for 40 minutes. SEM and TEM characterization showed the formation of fibers that were typically 10-100 microns long and 0.1-1 micron in diameter. Interestingly, each fiber had an iron-rich "belt" around its middle, which was easily removed with heat treatment.

The group found that excessive amounts of FeCl<sub>2</sub> vapor saturated the reaction atmosphere and limited the reaction with carbon. Additionally, excessive carbon suffocated the catalyst and caused premature termination of growth. Though inconclusive, the origin of the Fe rings was thought to be due to the direct reaction of FeCl<sub>2</sub> (foiled hexagonal solid) with carbon radicals to form iron (cubic crystal) and chlorine (as chloro-carbons).

The translation of this process from atmospheric pressure to vacuum yielded significant improvements in the regulation of relative FeCl<sub>2</sub> - carbon concentrations. Inoue et al. [28] demonstrated the rapid (0.1 mm/min), growth of large-scale, aligned CNT arrays using only FeCl<sub>2</sub> and acetylene. The catalyst was heated to 820°C and vaporized in a quartz tube under vacuum. In this step, the catalyst vapor is constantly colliding with and depositing on surfaces within the chamber. The deposition is temporary in vacuum however, and it immediately re-evaporates. This cycle continues until the growth gas, acetylene, is released causing the condensation of Fe-containing particles on all heated surfaces. Acetylene flow was managed using a mass flow controller, and the pressure was maintained at 10 Torr. Growth was allowed to continue for 20 minutes, which yielded 2.1 mm tall arrays. TEM characterization showed that the CNTs formed were MWNTs with diameters of 30 - 50 nm. Decreasing the growth pressure from 10 Torr to 4 Torr did not change the length of the arrays, but they were attached less strongly to the quartz substrate. Arrays grown at 4 Torr could be spun into macroscopic yarns using tweezers.

One reason for the rapid growth rate attained using this method is the high dehydrogenation activity of FeCl<sub>2</sub> on acetylene, which is not seen with traditional supported catalysts. High dehydrogenation activity increases the amount of carbon available for reaction. What results is rapid, ultra-long, vertically aligned CNT array growth, covering all surfaces of the reactor tube and

substrates. These arrays can be harvested, and subsequently customized and post-treated for a variety of applications. Due to the elimination of time-consuming pre-deposition steps and quick growth time, CM-CVD is considered to be a viable option for economical mass production of CNT arrays.

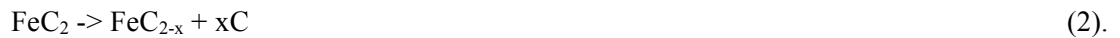
In this method, FeCl<sub>2</sub> powder was used both as a catalyst for nucleation, but also propagation of CNT growth. At the growth temperature of 760°C, the catalyst is completely vaporized. When acetylene is let into the reactor, the following reaction takes place:



The low vapor pressure of FeC<sub>2</sub> allows for vapor phase collisions to take place until it collides with the surface of the quartz where a catalyst nanoparticle forms. The morphology of FeC<sub>2</sub> particles was characterized by Kosugi et al. [32]. In their work, the reaction produced Fe nanocrystals with a carbon skin. Independent of the size of the Fe nanoparticle, the carbon skin that formed around the particle measured 3.5 nm. The presence of the characteristic 002 graphite peak confirmed that the carbon skins had a graphitic structure which grew parallel with the iron lattice axis.

Interestingly, the group also found that the carbon skin is valently bonded to the iron particle. Due to the similarity in Fe-Fe and C-C bonding in graphitic structures, (2.866 Å and 2.842 Å respectively), there was “accidental matching” which allowed for the growth of the graphitic plane. This coincidence is unique for the graphitic carbon and iron system as it does not occur in cobalt or nickel systems which are common catalysts used in CNT growth [32].

At high temperatures iron nanoparticles are liquid and carbon is free to migrate through the iron structure. As more carbon is added to the system, the graphitic layers form on the outside of the particle. As more layers form, the innermost layers apply pressure to the catalyst particle due to the constraining volume, and the metal particle is eventually expelled from the newly formed graphitic tube [33]. This represents the initiation of growth of the CNTs. The segregation of the graphene layers from the Fe particle is shown in the following reaction:



The formation of graphene layers continues as the catalyst reacts with acetylene. When the carbon concentration in and around the catalyst particle falls below a certain threshold, growth is terminated. Periodic changes in the carbon concentration within the iron catalyst particle results in changes of the inner diameter of the MWNT. By keeping the carbon concentration consistent throughout the growth process, more consistent CNTs can be grown.

In CM-CVD, there is the added benefit of the dehydrogenation activity of chlorine on acetylene [31]. This aids in maintaining a constant supply of carbon at the nanoparticle surface.

Additionally, remaining iron(II) chloride vapor in the system as well as the reaction-produced HCl can react with iron nanoparticles according to the following reaction:



Then, acetylene will be rapidly decomposed at the nanoparticle surface. The reaction takes place as follows:



Here again, carbon will rapidly segregate and form graphene layers on the catalyst particle, following Equation 2 from above. This cycle is thought to repeat quickly, resulting in the rapid growth of ultra long CNTs. It is easy to see how the rate of growth would be greatly decreased without the added catalyst activity provided by the  $\text{FeCl}_2$ .

### **2.3 Carbon Nanotube Reinforced Composites**

Composite materials, which can be naturally occurring or man-made, comprise two phases - the matrix, and the filler or reinforcement. Composites are classified by the type of material used for the matrix: polymer (PMCs), ceramic (CMCs) or metal (MMCs). The reinforcement material is chosen based on the desired application or material performance. These could include strength, stiffness, thermal or electrical conductivity, wear resistance, toughness and many others. In an ideal scenario the separate phases will work together synergistically to yield an enhanced multifunctional composite.

Carbon nanotubes are a highly desirable reinforcement material because they are multifunctional in nature and possess extraordinary physical properties. All classes of materials have the potential to be enhanced through utilization of CNT reinforcement. Polymers can be made conductive, ceramics toughened and metals lightened with minimal CNT additive. Because of their small size and large aspect ratio, ~1 wt% concentrations of CNTs form integrated networks capable of electrical, thermal and even mechanical energy transfer. Due to ease of processing and composite manufacture, research studies using polymer matrices are the most prevalent as shown in Figure 2.1. In all cases, CNT concentrations above 10 wt% are rare even though significant material enhancement can be realized by using higher volume fractions.

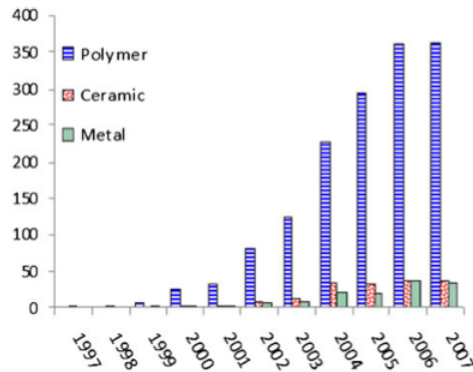


**Figure 2.1** Number of publications on polymer, ceramic and metal matrix - CNT composites from 1997 to 2007 (taken from Bakshi et al [34]).

The reasons for this are varied. Most current CNT synthesis techniques must strike a balance between high throughput capacity and CNT purity and quality. Techniques that satisfy both criteria are limited, thus making large amounts of high quality CNTs expensive. CNTs are also notoriously difficult to process due to their surface properties. Chemically inert C-H bonds cover the outermost wall creating a non-reactive interface between the matrix and reinforcement phases. Additionally, C-H bonds are strongly hydrophobic which makes mutual wetting of the two phases difficult [35–37].

The large specific surface area of CNTs ( $>200 \text{ m}^2/\text{g}$ ) certainly makes them attractive for many applications, but their large aspect ratios also create strong van der Waals attractions between adjacent tubes. This leads to bundling and agglomeration of CNTs, which is extremely difficult to reverse without causing damage to the structure. The inhomogeneous dispersion of reinforcement within a matrix creates stress concentrations, which diminish mechanical enhancement, often yielding a composite even weaker than the starting material. This concept applies to electrical and thermal enhancement as well.

These issues are common to each class of composites, though traditional ceramic and metal processing techniques have additional associated incompatibilities due to high processing temperatures. Despite the difficulties, there is a considerable amount of research focused on the development of novel fabrication techniques for ceramic and metal matrix composites. Polymer and ceramic matrix composites fall outside the scope of this thesis, so the following investigation will focus on metal matrix systems.

### 2.3.1 Carbon Nanotube - Metal Matrix Composites

Metals and their alloys have dominated the structural landscape for decades but increasing energy demands and declining oil supplies have motivated researchers toward developing lighter structural materials. Compared to PMCs, metals and their composites have superior high temperature stability, excellent thermal and electrical conductivity, and are impenetrable to laser, UV and nuclear radiation.

Early development of MMCs combined ductile but strong metals with a stiff reinforcement material. The resulting composite possessed both strength and stiffness while also decreasing density. These materials are employed today in the automobile and aerospace industries where they have increased both payload capacity and fuel efficiency. Composites with low coefficients of thermal expansion (CTE) and high thermal conductivity are attractive for electronics packaging and thermal management applications.

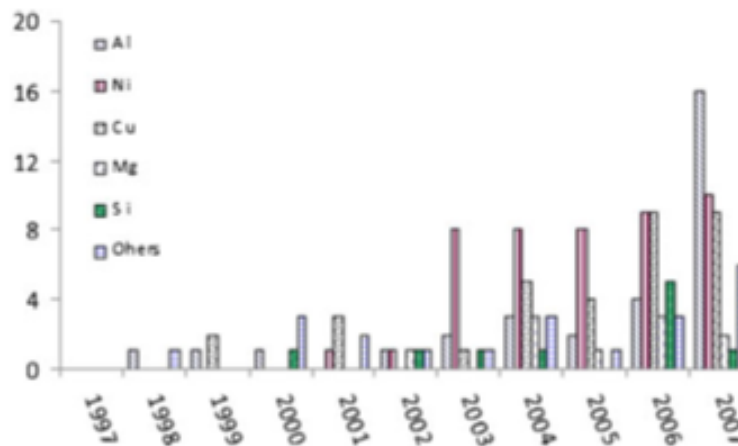


**Figure 2.2** Number of publications on different metal matrix-CNT composites from 1997 to 2007 (taken from Bakshi et al. [34]).

As shown in Figure 2.2, interest in using CNTs as reinforcement in MMCs has steadily increased over the last decade, with aluminum, copper and nickel being the most studied. Though Cu-CNT composites are the subject of this thesis, the processing routes are common for all metals as many are derived from traditional metallurgical techniques. These processing methods include

powder metallurgy, electrochemical deposition, thermal spraying, melt processing, as well as more novel techniques such as molecular level mixing, sputtering, CVD, and nanoscale dispersion via ultrasonication.

There are three main challenges associated with processing CNT reinforced MMCs, and the degree to which these challenges are overcome vary with each method. First, a homogenous dispersion of CNTs in the metal matrix must be achieved and maintained in the final product. Inhomogeneous structures, which are caused by CNT agglomeration, create porosity and discontinuity in a composite. They result in stress concentrations and act as barriers to electrical and thermal energy transfer throughout the bulk. Another processing challenge is controlling interfacial bonding between the metal matrix and CNT reinforcement. Dujardin et al. found that CNTs could be wet by substances that have low surface tension, with an upper limit of 200 mN/m [38]. Copper, with a surface tension of 1270 mN/m, will not naturally wet the surface of CNTs, so alternate routes for promoting wetting between composite phases must be investigated. Lastly, the chemical and structural stability of CNTs must be maintained during composite processing. In air excessive temperature causes oxidation of the CNT walls, which greatly degrades physical properties. Processing routes must minimize this potential in order to achieve material enhancement.

It should be noted here that for certain applications it is desirable to align the CNTs within the matrix. Due to the anisotropic nature of their properties, the capacity for matrix enhancement is greater when the CNTs are axially aligned in the direction of energy transfer - whether mechanical, thermal or electrical. Finally, according to the rule-of-mixtures the capacity for property enhancement increases with increasing volume fraction of reinforcement. It follows then, that increasing the fraction of CNTs in the composite should result in a higher performing material. High volume fractions of CNTs are notoriously difficult to achieve however, and successfully doing so has proven elusive for many researchers in the field. Regardless, CNT alignment and increased volume fraction are certainly challenges, though secondary to those listed above. Their importance is end-use driven, but they should remain a driving goal in CNT-MMC development.

## ***2.3.2 Processing Routes for Carbon Nanotube - Copper Matrix Composites***

### *2.3.2.1 Powder Metallurgy*

Powder metallurgy is the oldest and most-used MMC processing route. At the most basic level, it is the conversion of metal powders to densified solid through the use of heat and pressure. To make a composite, the matrix and reinforcement materials must be intimately blended which is often accomplished via simple mixing or ball milling. Once mixed, a precise amount of powder is either hot or cold compacted into a die of the desired shape. The resulting sample is partially densified, but must undergo further processing to remove unwanted porosity. Common consolidation techniques include conventional sintering, hot pressing, spark plasma sintering and deformation processing.

Conventional sintering is the most basic method, relying on thermal energy to encourage atomic diffusion and surface tension to bond adjacent metal particles. Care must be taken when using this method to prevent sample oxidation and grain growth; both of which degrade material properties. The same is true of hot pressing, as it also requires heating to consolidate the sample. Hot pressing equipment simultaneously heats the sample while also applying pressure. Again, the process must be carried out in vacuum or inert atmosphere to prevent sample oxidation. Spark plasma sintering (SPS) was developed more recently as a method to quickly heat the powder particles. Instead of using electrically resistive coils, induction or radiation to heat the sample (as in sintering or hot pressing), a DC current is pulsed through the powder sample. Rapid heating occurs due to electrical spark discharge between particles. Heating rates up to 1000K/second are achievable using this method, making it more desirable to prevent grain growth as well as sample oxidation. Deformation processing includes hot and cold rolling, and extrusion. These methods apply shear force to the composite sample inducing grain refinement while also decreasing density. Additionally, due to the large shear forces applied during processing, the shell structure of the CNT clusters is disrupted and CNTs are aligned in the direction of shear. Because of this, good mechanical properties can be expected from composites formed in this manner.

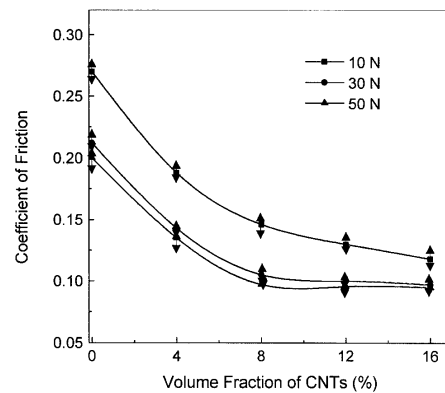
Dispersion of CNTs in metal powder is achieved by feeding the materials in a rotating drum along with hardened steel or ceramic balls. The rotation causes repeated impact of the drum walls, powder and balls that causes mechanical deformation and welding of the metal powder particles. Simultaneously, CNTs are trapped between welded particles, thus creating an intimate blend of phases.

Control of material and process parameters affects the quality of the blend. By starting with smaller metal particles, a more homogenous blend can be achieved, but there are increased health risks associated with small diameter particles as well as increased potential for oxidation. Therefore, researchers have adopted more novel methods to promote bonding including the coating of CNTs [39–41]. Using electroless plating, CNTs were first coated with Ni before being ball milled with Cu powder and consolidated via pressing and sintering. This was said to improve the bonding strength between matrix and reinforcement. Five samples were made with increasing concentrations of CNTs (0, 4, 8, 12 and 16 vol%), and Cu powder (particle diameter 70 $\mu$ m) by mixing for 30 minutes in a ball mill. The powder mixtures were pressed at 600 MPa and 100°C, and then sintered for 2 hours at 800°C. The porosity, hardness, coefficient of friction and wear rate of the samples were characterized. It was determined that the porosity of the composites remained stable at lower volume fractions, but then increased at 12 vol% CNTs. This was attributed to CNT clustering and agglomeration. Because of this the hardness of the composites first increased within increasing volume fraction, and then decreased above 12 vol% CNTs. Conversely, the coefficient of friction and wear rate both decreased initially, and then increased with higher concentrations of CNTs. The results from these experiments can be seen in Figure 2.3.

Table 2  
Hardness and porosity of unreinforced copper alloy and carbon nanotube–copper composites.

Specimen	Average hardness (HRB)	Porosity (%)
Cu alloy	10.2	2.41
Cu–4 vol% CNTs	15.4	2.56
Cu–8 vol% CNTs	20.2	2.47
Cu–12 vol% CNTs	21.5	3.08
Cu–16 vol% CNTs	19.8	4.92

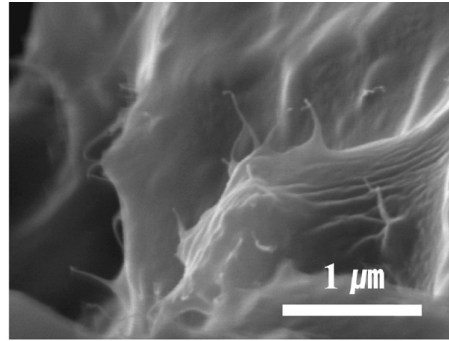
A



B

**Figure 2.3** Increasing the volume fraction of CNTs in Cu results in changes in composite A) hardness and porosity and B) coefficient of friction (taken from Tu et al. [39]).

C. Kim et al. compared the properties of composites made with both nickel-coated and pristine CNTs. Additionally the electrical and thermal conductivities were characterized. The nickel-coated SWNTs were first sonicated in ethanol before adding Cu powder particles (10-15 $\mu$ m) and sonicated at 50°C until most of the ethanol was evaporated. They claimed to have achieved a homogenous dispersion via mechanical mixing due to the similar densities of nickel and copper. The blended powders were hot-pressed in vacuum at a pressure of 45 MPa while the temperature ramped to 600°C over 40 minutes and then was left to dwell for an additional 30 minutes.



A

No	Sample	$R$ ( $\Omega$ cm)	Std. Dev.	No	Sample	$R$ ( $\Omega$ cm)
1	Pure Cu [24-27]	$1.72 \times 10^{-6}$		5	Beryllium copper [25,27]	$9.07 \times 10^{-6}$
2	Sintered Cu	$1.76 \times 10^{-6}$	$8.47 \times 10^{-7}$	6	Manganese bronze [24,26,27]	$2.30 \times 10^{-5}$
3	Sintered Cu(83%) + Ni(17%)	$1.03 \times 10^{-5}$	$6.54 \times 10^{-7}$	7	Stainless steel 304 [27]	$7.2 \times 10^{-5}$
4	Sintered Cu(83.27%) + Ni(16.65%) coated SWNT(0.08%)	$1.43 \times 10^{-5}$	$1.16 \times 10^{-6}$			

B

**Figure 2.4** A) Micrograph showing the pull out length of Ni-coated SWNTs in a copper matrix on a tensile test fracture surface, and B) the thermal and electrical conductivities of many common electrical contact materials (taken from C. Kim et al. [42]).

The mechanical and tribological properties of the Ni-SWNT reinforced composites were significantly improved over the pure copper and copper-Ni controls. Due to the extended pull out length of the CNTs in tested samples they concluded that good interfacial strength as a result of dissolution of Cu and Ni at the matrix-reinforcement interface. Although they did not find that the electrical and thermal conductivities of the CNT-reinforced composites increased, they noted that

their performance was on par with other electrical contact materials. These findings are shown in Figure 2.4.

In an attempt to improve the dispersion of CNTs in Cu, Kim et al. [43] used smaller Cu particles ( $\sim 10\mu\text{m}$ ) and high-energy ball milling. This process involves the use of higher rpm and longer duration. The samples were spark plasma sintered at  $700^\circ$  for one minute in vacuum under a pressure of 50MPa and then cold rolled to a 50% reduction. Finally the samples were annealed at  $650^\circ\text{C}$  for three hours. Even after extensive processing, the composites exhibited poor CNT dispersion. Two regions were formed, one with and the other without CNTs. This was confirmed through tensile testing due to the presence of both primary and secondary yield strengths. Though mechanical improvement was seen its extent was hindered due to the inhomogeneous distribution of CNTs in the Cu matrix as shown in Figure 2.5.

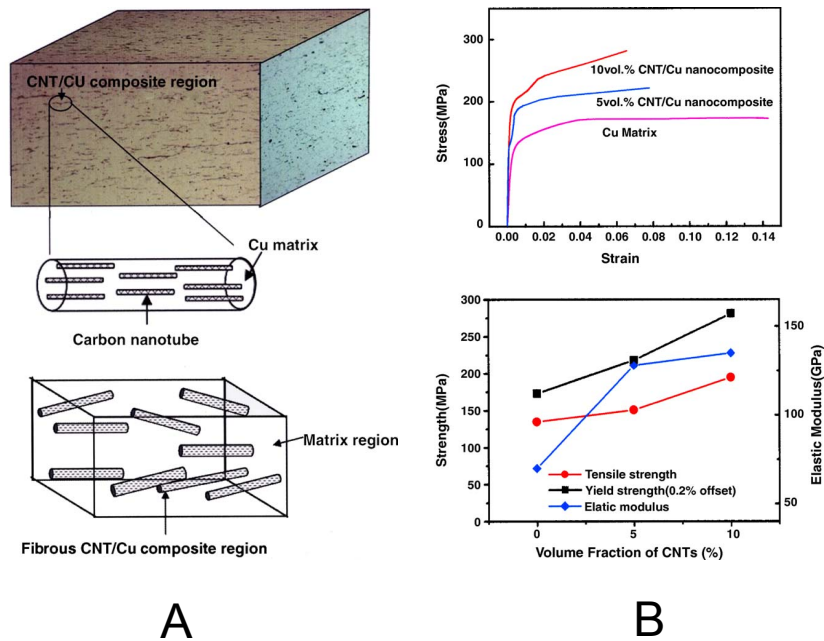


**Figure 2.5** High-energy ball milled composites do not exhibit a homogeneously dispersed CNTs, instead forming A) two distinct phases, and B) two separate yield strengths (taken from Kim et al. [43]).

Li et al. [44] used a combination of ball milling, consolidation and high pressure torsion (HPT) to fabricate MWNT-Cu composites. The use of HPT avoids the high-temperature sintering step to prevent CNT damage as well as Cu grain growth, both of which hinder mechanical performance.

Cu powders (0.5-1.5 $\mu$ m) and pristine MWNTs were high-energy ball milled in an argon environment for 5 hours. 1wt% CNT-Cu and pure Cu composite powders were compacted at a pressure of 500 MPa in air at room temperature. Finally, the composite discs were further consolidated using HPT under 6 GPa for 5 revolutions, also at room temperature. HPT is a type of severe plastic deformation technique that has been shown to refine grain sizes and improve mechanical properties of metals and their nanocomposites.

Ball milling caused metal particles to cold weld together to form larger particles with diameters ranging from 10 to 50 microns. High resolution SEM of powder particles did not show a presence of CNTs on the particle surfaces, meaning that the CNTs were fully combined throughout the Cu. The grain size for the Cu-CNT and pure Cu composites were 22 and 29 nm respectively. Additionally, the grain size distribution was much tighter for the Cu-CNT composite sample. TEM observations showed CNTs inside and also traversing between nanocrystalline grains, which is important for property enhancement. These qualities yielded composites with microhardness values higher than that of pure Cu, as shown in Figure 2.6.

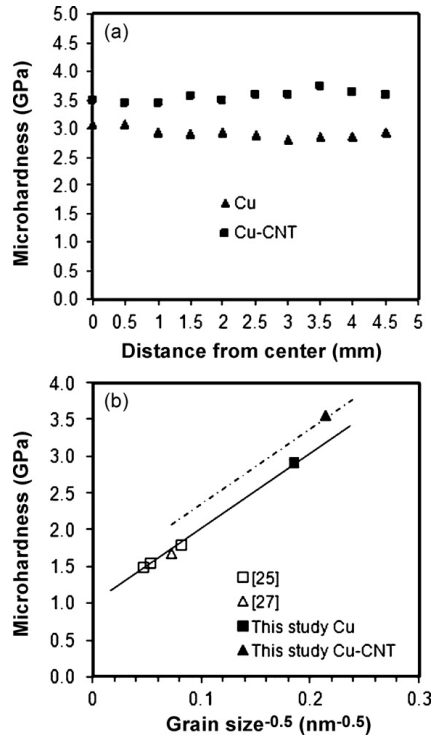


**Figure 2.6** The microhardness and grain size of CNT reinforced Cu composites was enhanced and consistent across the surface of the samples (taken from Li et al. [44]).

This paper is a strong example of the potential of powder metallurgy techniques. For tribological applications, compacted composite pellets are ideal, but without CNT alignment, electrical and thermal performance are lacking. Also, this technique does not lend itself to the incorporation of high concentrations of CNTs nor long CNTs. In all papers reviewed, the length of CNTs did not exceed a few microns. These inadequacies have lead researchers to explore other composite fabrication routes.

### 2.3.2.2 *Electrochemical Methods*

Electrochemical methods are the second most popular composite processing route, behind powder metallurgy. They are primarily used for depositing thin films or coatings of metal onto the CNT surface. The thickness of the coating is process dependent, but there is an upper limit of 200 $\mu\text{m}$ . Therefore it is not feasible to make a free standing composite with this method, but it is still very

effective at creating high quality coatings. Additionally, variations of these methods are capable of coating aligned arrays, which increase homogeneity and dispersion.

The two processes used in this type of method are electrodeposition and electroless deposition. The former is a deposition process that uses electrical current to reduce metal cations from a salt solution and then coat a conductive object. In a similar process called electrophoretic deposition, colloidal metal particles are used instead of ions. Metal nanoparticles are suspended in liquid media and an electric field is applied. The particles migrate due to electrophoresis and deposit onto an electrode. A hybrid of these two methods, known as co-deposition, uses a suspension of CNTs in an ion-salt solution. CNTs and metal particles are simultaneously deposited onto a substrate. This technique can also be utilized in electroless deposition, which is similar to electrodeposition but does not require an electrical current. Instead solutions of metal salts are thermochemically decomposed to release ions, which then deposit onto CNTs. Though less energy intensive, electroless deposition is slower and not able to achieve the same deposition thickness when compared to electrodeposition.

The earliest examples of using electrodeposition for Cu-CNT systems established a viable procedure for filling gaps in aligned CNT and carbon nanofiber (CNF) arrays with Cu [45], [46]. The motivation was the fabrication of a suitable heat-sink material for electronic devices, so the interfacial heat conduction and mechanical properties of the composites were investigated. Aligned CNT arrays with length  $\sim 7.5\mu\text{m}$  were filled with Cu using an electrodeposition set-up where the CNT array was the working electrode. Chloride ions and polyethylene glycol (PEG) were added to the electrochemical bath to encourage "bottom up" assembly of Cu into the voids. In the presence of  $\text{Cl}^-$ , PEG molecules adsorb on the top of the array structure, preventing Cu from top filling and sealing the gap. Bis(2-sulfopropyl) disulfide (SPS) and Janus green B were added to accelerate deposition in the voids. They found that the quality of the deposition was influenced by a variety of factors such as electropotential, time, type of seed layer metal, as well as the length distribution and density of the array. Control of these parameters resulted in a material with 30% void space and the deposition rate averaged 430 nm/minute. As-deposited Cu created a very rough surface on top of the arrays, which made it difficult to establish a large contact area for electrical and thermal testing. To smooth the surface the top of the array was etched for 45 seconds in 85% ortho-phosphoric acid.

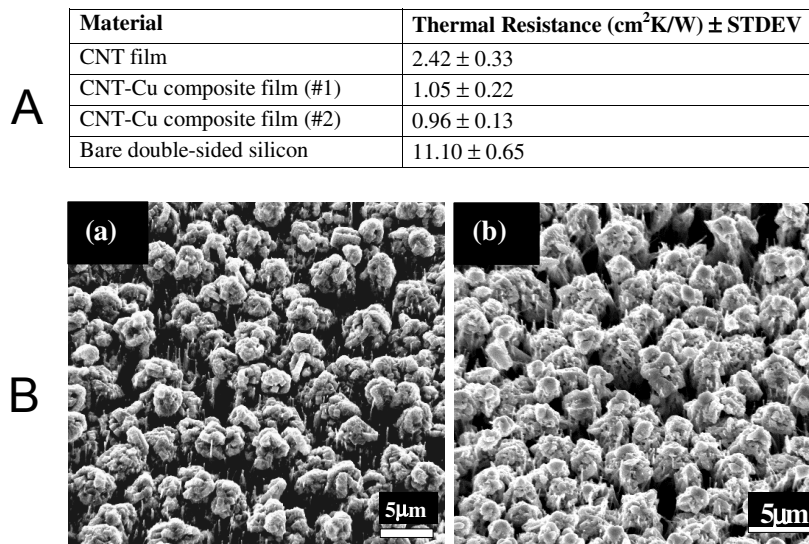


**Figure 2.7** A) Table of thermal resistance values for control CNT film and CNT-Cu composite samples and, B) SEM micrographs of composite samples before and after compressive thermal resistance measurement (taken from Ngo et al. [46]).

The thermal resistance of the resulting composites was lower than CNT films, decreasing from  $2.42 \text{ cm}^2\text{K/W}$  to  $0.96 \text{ cm}^2\text{K/W}$ . Additionally; the arrays were stable in moderate compression, exhibiting no change in morphology before and after measurement. These results are shown in Figure 2.7.

When the CNTs are not in array form, measures to ensure homogenous dispersion of CNTs throughout the deposited metal must be taken. Male et al. [47] electrodeposited CNTs and Cu nanoparticles onto glassy carbon electrodes for detection of carbohydrates. Cu nanoparticles and SWNTs were mixed with Nafion, a perfluorosulfonated, negatively charged polymer to promote dispersion. The charge interactions made it possible to deposit Cu particles evenly onto the SWNTs. TEM characterization and cyclic voltammetry were used to confirm even distribution and adequate electrical contact between the Cu nanoparticles and SWNTs.

Ferrer-Anglada et al. [48] neglected a mixing step altogether. A thin film was composite was fabricated by using a thick SWNT buckypaper as the working electrode. Not surprisingly, Cu deposition was significant (55 wt% Cu), but the distribution was very inhomogeneous. Figure 2.8 shows the bi-layer composite that was formed. There is minimal interfacial area between phases, existing only where implantation of Cu particles into the buckypaper occurred.

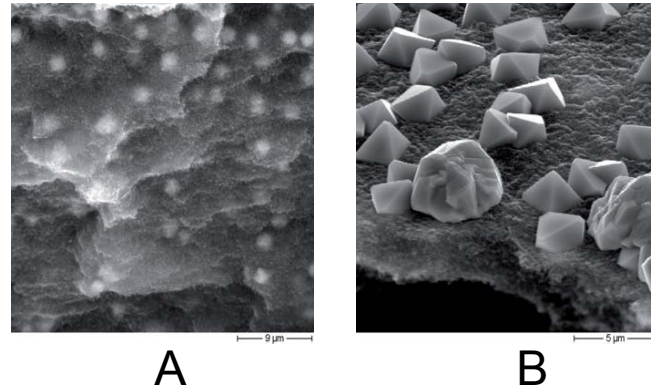


**Figure 2.8** SEM images of SWNT buckypaper-Cu nanoparticle bi-layer composites containing A) 31 wt% Cu; B) 39 wt% Cu (taken from Ferrer-Anglada et al. [48]).

Similar to earlier work [45], [46], Chai et al. [49] used electrodeposition to fill voids between aligned CNTs. They expounded on the concept by comparing two different aligned CNT systems. The first was an as-grown array and the second used patterned catalyst deposition prior to CNT growth. This formed a hierarchical array structure that they termed "CNT via". These vias would serve as controlled pathways for electrical and thermal conduction.

Photolithography was used to pattern vias in a 1 μm thick thermal SiO<sub>2</sub> layer on top of a Si wafer. Ti was then sputtered to act as the bottom electrode for eventual electrodeposition, and finally a Ni catalyst layer was deposited via e-beam evaporation. CNTs were grown in the newly patterned vias using thermal CVD. SEM analysis showed that they average spacing between adjacent CNTs was 50nm. Copper deposition was carried out using CuSO<sub>4</sub> as the ion source and mounting the CNT covered wafer on the cathodes of the electrochemical cell. Controlling the current density and deposition time yielded nearly complete filling of the air voids. Effectiveness of the technique for filling voids in a pristine array was first demonstrated. Then Cu was deposited on the patterned array. Again, significant filling was achieved in excess of 40% Cu.

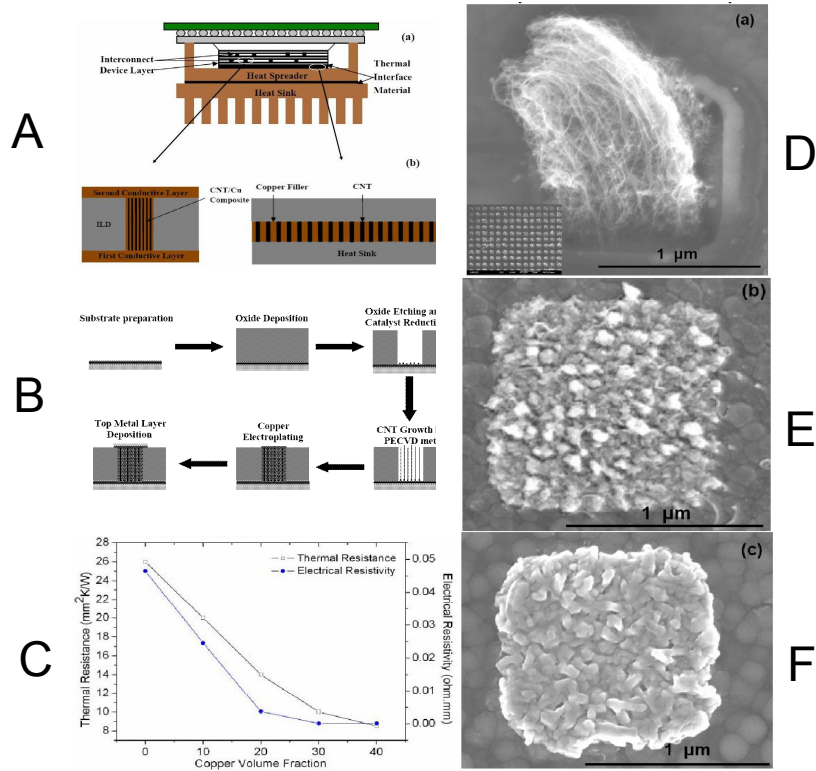


**Figure 2.9** A) Schematic of thermal management component architecture with integrated Cu-CNT composite; B) process flow for fabricating CNT via structure; C) electrical and thermal resistance as a function of copper content; SEM images of D) CNT via; and E) and F) Cu-CNT composite vias with different copper loadings (taken from Chai et al. [49]).

Figure 2.9 shows the results from compressive resistance characterization of the Cu filled, patterned composite. It exhibited lower electrical resistance compared to pristine CNTs and decreasing thermal resistance with increasing Cu content. These results are attributed to the increased contact area of the samples to the electrode. The purpose of patterning is purely to demonstrate the applicability of the technique and that the resulting material is viable as a material for interconnect devices. A side benefit is the increased performance, which was attributed to the higher statistical probability of more perfect alignment of CNTs due to the volume constraints of the vias.

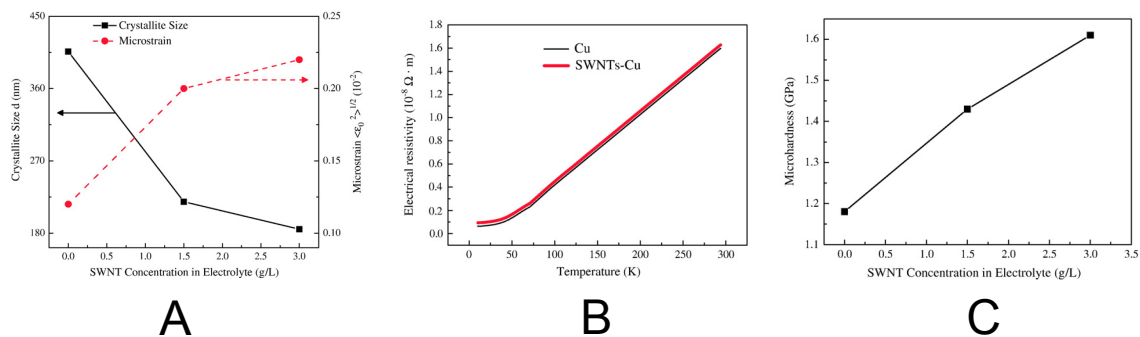


**Figure 2.10** A) Crystallite size and micro-strain of SWNT-Cu composites; B) dependence of electrical resistivity of SWNT-Cu composites and pure Cu and; C) micro-hardness of SWNT-Cu composites (taken from Yang et al. [50]).

Yang et al. [50] improved the mechanical performance of pure copper by electrochemically depositing SWNT-Cu coatings in an ultrasonic field. This simply means that instead of a stagnant electrochemical bath, ultrasonication was used to maintain a stable dispersion throughout the duration of the deposition. The composite coatings retained high electrical conductivity, comparable to pure Cu. The strengthening, (shown in Figure 2.10), was attributed to a decrease in crystallite size and increase in lattice micro-strain, in addition to the homogenous dispersion of SWNTs in Cu from ultrasonication.

The tensile properties of Cu-CNT composites were characterized by electrodepositing films onto a previously fabricated mold. CNTs of various diameters were used to determine the effect on strength. Smaller CNT diameters yielded greater tensile strengths due to the increased interfacial bonding with greater surface area. The highest measured strength was 670 MPa, which is three times higher than pure copper [51].

Increasing the concentration of CNTs in a composite will yield greater performance. The maximum attainable concentration is limited, however by the ability to maintain a stable dispersion of CNTs within the electrolyte solution. Higher CNT concentrations have a greater potential for agglomeration and bundling and concentrations above 10 vol% are rare.

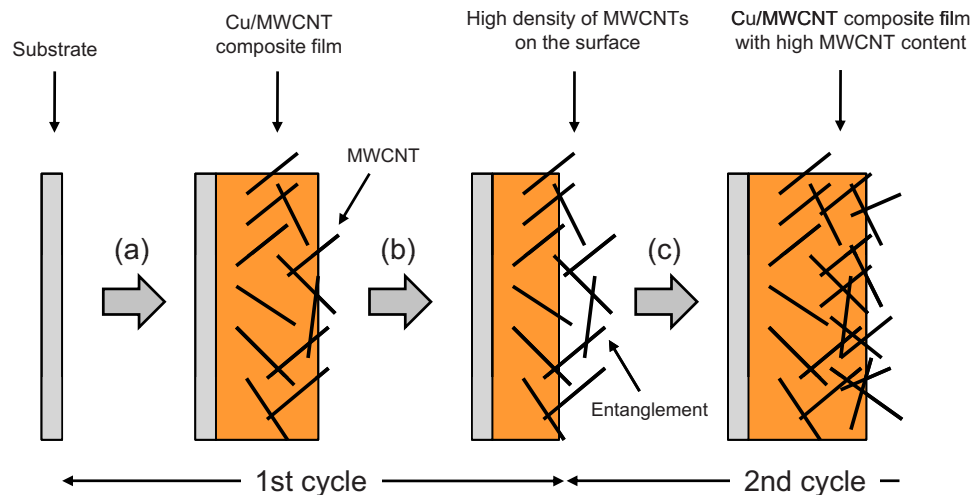


**Figure 2.11** Schematic process for Cu-MWNT composite fabrication method using pulse-reversed electrodeposition (taken from Arai et al. [52]).

Instead of increasing the CNT concentration in the electrochemical bath, Arai et al. [52] used a pulse-reversed electrodeposition method to increase the final resulting amount of CNTs in the composite. Pulse-reversed technology is generally used to smooth the morphology of deposited films. When a film is pulsed, granular or spherical shaped particles are removed from the surface due to the low level of interaction area between the particle and deposited film. CNTs are not granular or spherical and have a relatively large level of "entanglement" due to interaction area with the film. This mechanism, shown in Figure 2.11, then makes it possible to remove granular Cu particles, leaving CNTs behind.

Optimization of process parameters such as pulse duration and current density lead to an increase in MWNT content within the composite. The maximum attained density was 0.59 mass % compared to 0.42 mass % CNTs in a sample prepared with traditional electrodeposition. Although this is a 40% relative improvement, the concentrations attained are still low. The group reported that this modified deposition procedure also resulted in smoother surface films.

Studies using electroless deposition are far less prevalent. This is likely due to the additional complexities that stem from the deposition mechanism. The thermochemistry of the system must be well understood and controlled for successful deposition. This means that the bath temperature and pH must be carefully controlled, and even the, minimal film thickness can be achieved.

CNTs were coated with nanometer-thin films of Cu using electroless plating for eventual incorporation via powder metallurgy into Cu-CNT composites [53]. This step is similar to work mentioned earlier where CNTs were first coated with Ni before ball milling and composite formation. This increases the density of the CNTs, making it easier to achieve a homogenous dispersion. Before commencing deposition, there are several steps involved in preparing the CNTs. First, they were cleaned and functionalized in HCl, nitric and sulphonic acids through various sonication, stirring, soaking and drying steps over the course of 40 hours. Then the CNTs were sensitized with stannous chloride and water for 2 hours at a pH of 1-3, and then catalyzed by stirring in CuSO<sub>4</sub> for an additional 2 hours.

The copper deposition was completed by first adjusting the pH to 11.5, and then adding trisodium citrate dihydrate to act as a complexing agent to the Cu ions. Formaldehyde was subsequently added, which acts as a reducing agent. Composite powders were prepared with 5, 10, 15, and 20 vol% CNTs along with a pure Cu sample as well. The powders were spark plasma sintered at a compaction pressure of 50 MPa for one minute at 550°C in vacuum. A summary of these results can be found in Figure 2.12.

Coating the CNTs prior to composite fabrication yielded a homogenous distribution throughout the composite with decreased agglomerations at grain boundaries. The density and electrical conductivity decreased with CNT volume fraction, while hardness and yield strength generally increased. Though material improvement was realized, the extensive procedure used for preparing the composite powders was extremely time, energy, and resource consuming. The precise control of a wide range of pH is difficult and prone to failure. The general consensus in the field is that this procedure is not viable for large-scale implementation due to these difficulties.

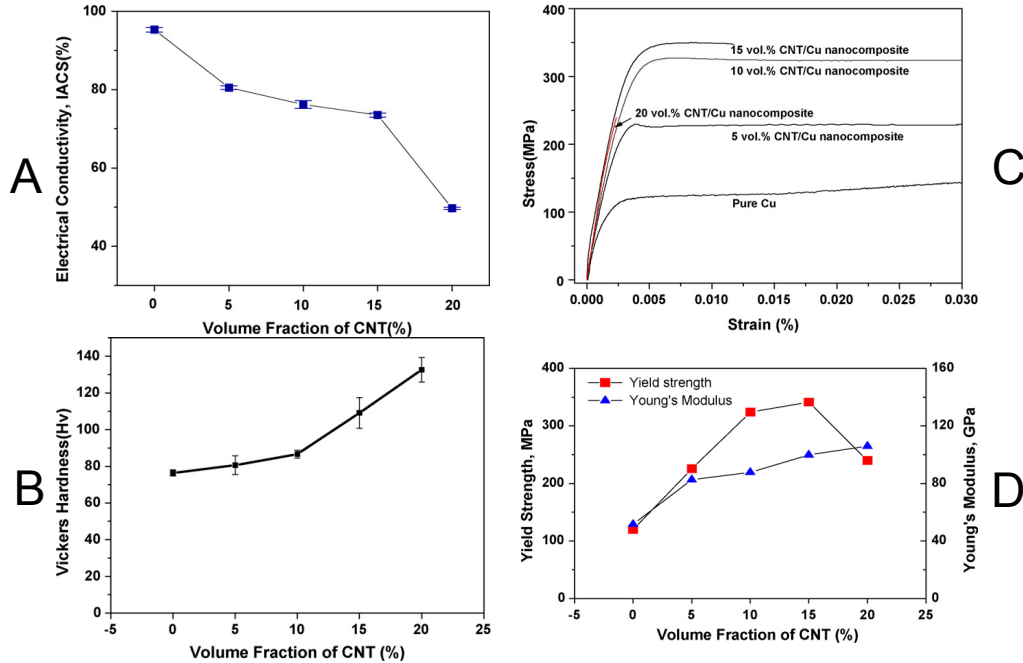


**Figure 2.12** Physical properties of composites produced with electroless plated CNTs including A) electrical conductivity; B) hardness; C) stress-strain and; D) elastic modulus and yield strength (taken from Daoush et al. [53]).

### 2.3.2.3 Molecular Level Mixing

One example of a novel processing route that is particularly popular for Cu composite fabrication is molecular level mixing (MLM). This method is used to deposit coatings onto CNTs to form composite powders or 1D nanostructures. The CNTs are first acid treated to functionalize the surface, and then mixed into a metal-salt bath. The metal cations associate with the functionalized CNTs that, along with sonication, aids in eventual metal deposition. The CNT-metal ion system is dried, calcinated and finally reduced to produce a metal-CNT composite powder. The powders are then used in a variety of powder metallurgy processes to form a consolidated composite.

The earliest demonstration of this method was completed by Cha et al. in 2005 [54]. Here MWNTs were stirred in HF for 24 hours and then rinsed in a mixture of  $H_2SO_4/HNO_3$ . The CNTs were then sonicated in ethanol for two hours. Once stable, copper acetate was added to the suspension, and then sonicated for an additional two hours. The solution was dried while stirring on a

hot plate at 100°C, and then the powder was calcinated at 300°C in air. Figure 2.13 shows a schematic of the MLM process as well as a TEM micrograph of the resulting composite powders.

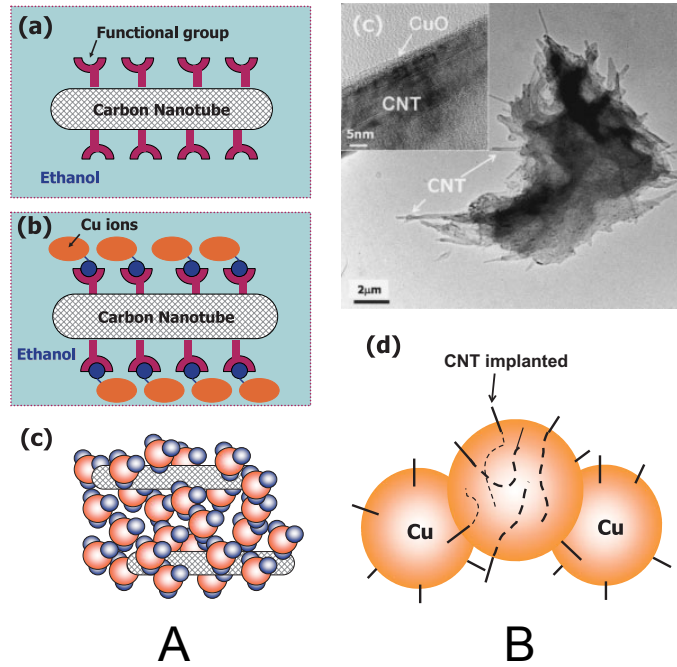
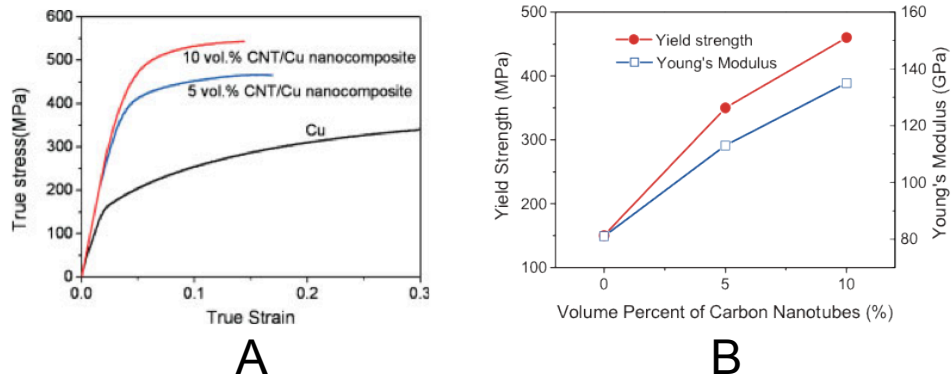


**Figure 2.13** A) Schematic depicting the functionalization of CNTs and dissociation of Cu salts onto CNT surfaces and; B) TEM micrograph and schematic of CNT/CuO powder showing implantation of CNT within CuO particles (taken from Cha et al. [54]).

The powders obtained in these steps are generally a mixture of CuO and Cu<sub>2</sub>O, and once calcinated are fully converted to CuO. When exposed to a hydrogen atmosphere, CuO reduces to form pure Cu and water vapor. The resulting CNT concentrations of the composite powders were 1 and 2.2 wt%. Using SEM and TEM, the microstructures of the composite powders were found to be homogeneously distributed, with CNTs implanted in the Cu matrix instead of on the surface.

To consolidate the powders, they were compacted in a graphite mold under 10 MPa of pressure and then spark plasma sintered at 550°C for one minute in vacuum. The resulting composites retained their homogeneity post-sintering as confirmed by SEM and TEM. TEM also showed that the CNTs form a network within the Cu grains, which show a low dislocation density due to the reinforcement they provide.

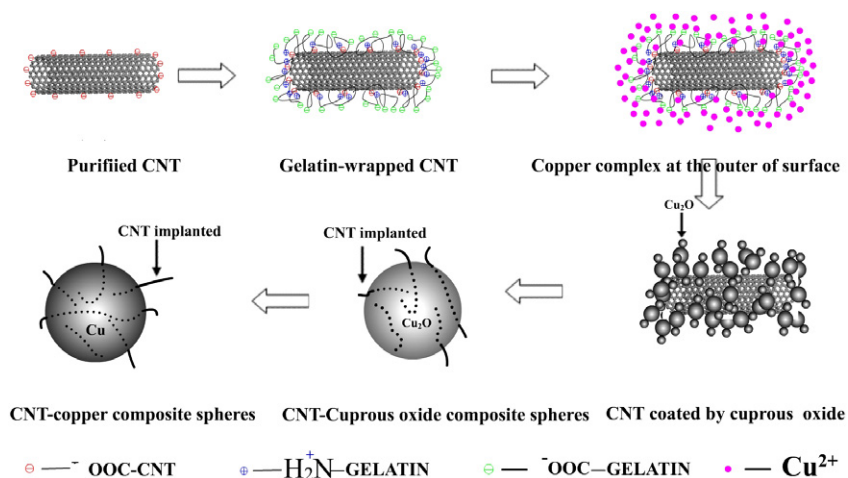
Compression tests on the composites showed increased yield strength and Young's modulus of both composites compared to pristine Cu. Due to high load transfer efficiency, the 2.2 wt% CNT-Cu composite exhibited a yield strength of 455 MPa--more than three times that of Cu. Figure 2.14 shows the results of the mechanical characterization.



**Figure 2.14** Mechanical properties of CNT-Cu composites formed via molecular level mixing: A) stress-strain curves of CNT-Cu composites obtained by compression testing and; B) yield strength and Young's modulus of CNT-Cu composites with increasing concentration of CNTs (taken from Cha et al. [54]).

In following work [55], Cha and colleagues studied the hardness and wear resistance of composites made with this procedure. They found that the composites were fully densified following spark plasma sintering with a relative density of 98.9% for 10 vol% CNTs. Hardness for the composites increased linearly with increased CNT content, reaching 1.1 GPa--1.8 times higher than pristine Cu. The nanocomposite also exhibited three times greater wear resistance compared to pure Cu due to the pinning of Cu by CNTs, which prevented the peeling of Cu grains. All of these improvements are attributed to the homogenous dispersion of CNTs in the Cu matrix and efficient load transfer.

Based on the MLM route, Xu et al. [56] set out to overcome the segregation of CNTs within MMCs due to the high differential in density between the matrix and reinforcement phases. To further enhance the resultant composite density additional factors such particle size uniformity, flowability and compressibility were also addressed.



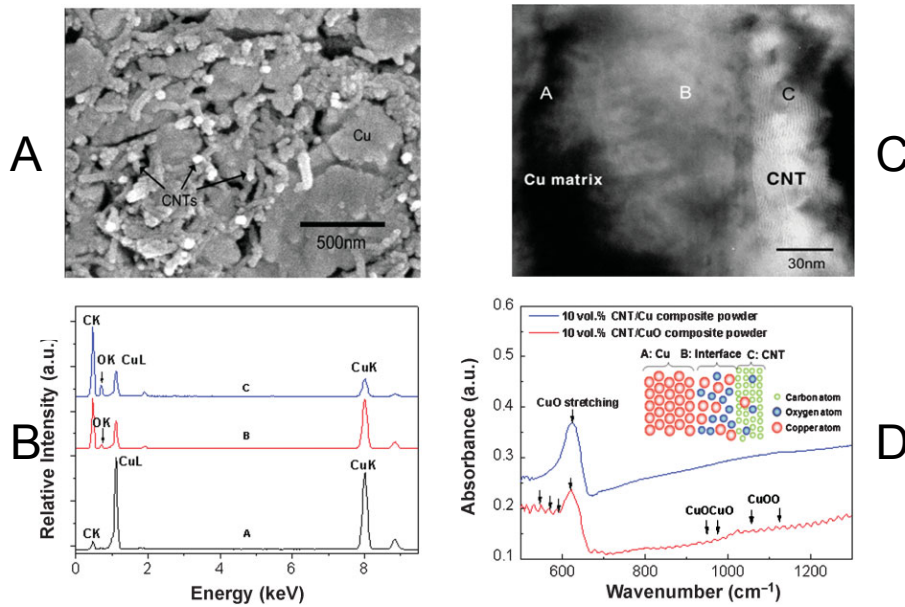
**Figure 2.15** Schematic of modified molecular level mixing procedure, which utilizes gelatin wrapping to “lock” copper ions onto the CNT surface (taken from Xu et al. [56]).

Figure 2.15 illustrates the modified MLM processing route used in that research. Following a functionalization process similar to Cha et al. [54], the CNTs were left with an excess of carboxylic acid groups covering the surface. They were then sonicated in gelatin for 30 minutes and due to electrostatic attraction, the amine groups of the gelatin associated with the negatively charged acid groups. This encouraged chain wrapping of the gelatin around individual CNTs. Following sonication,  $\text{CuSO}_4$  and glucose were added to the solution in that order, and then sonicated further. The gelatin that surrounds the CNTs acts as a ligand to the  $\text{Cu}^{2+}$  ions in solution, forming a complex. The hydroxyl groups of the glucose reduce the ions to form  $\text{Cu}^+$  and small  $\text{Cu}_2\text{O}$  particles nucleate on the CNT surface. PEG was added and the solution was heated. Precipitation of  $\text{Cu}_2\text{O}/\text{CNT}$  particles was completed via NaOH titration. The particles were removed using centrifugation, and then dried in vacuum. Particles were reduced in a hydrogen atmosphere for three hours.

The resulting particles had a spherical shape and clearly showed implanted CNTs throughout in TEM and SEM characterization. They found that they size of the particles was controlled by the titration rate of NaOH. Faster rates yield smaller particles due to rapid nucleation and ripening, and then subsequent encapsulation by PEG, thus restricting grain growth. Unfortunately the group did not choose to follow their powder synthesis with composite fabrication, though they mention that the powder would be an excellent candidate for MWNT-reinforced Cu composites.

Although achieving a stable suspension and homogenous distribution of CNTs within the composite are of primary importance for enhanced properties, further material improvements are possible by optimizing other aspects of the MLM processing route. Shock wave compaction (SWC) was used to fabricate 90% dense CNT-reinforced Cu composites, and the resulting microstructures were characterized. SWC is a high-energy process that occurs on the microsecond time scale, and is commonly used to consolidate metal powders. After using the previously established MLM procedure [54], the powders were statically pressed in a capsule to achieve 50% compaction. A 5mm thick steel flyer plate was accelerated using a propellant gun. The final speed of impact was ~1000 m/sec, after which the steel plate was lathed from the composite surface. The stress on the compact powder was calculated to be 15 GPa, which would be strong enough to not only consolidate the powder, but also cause melting, grain dislocations and distortion. Under SEM, nano-sized grains were found in addition to pores. Measurements showed that 90% densification was achieved. Even with 10% porosity, the microhardness of the composites increased beyond the Hall-Petch predicted value for a grain size of 79nm.

The nature of interfacial bonding between the CNT reinforcement and Cu matrix has been investigated more recently. In an effort to understand the strengthening mechanism of composites formed from MLM produced powders, Kim et al. investigated the role of oxygen at matrix-reinforcement interface [57]. As a result of the MLM process, there are two types of oxygen atoms present in the CNT/CuO powders: one is the oxygen stemming from functional groups and the other is the oxygen in the CuO matrix. Even after reduction in hydrogen, EDS and other techniques detected small amounts of oxygen in Cu-only samples, as well as increasing amounts with high concentrations of CNTs. Using TEM, three regions were analyzed with EDS to determine the elemental composition of each phase. They found that the interface contains a relatively higher concentration of oxygen atoms compared to pure Cu matrix or pure CNTs. FTIR spectra taken before and after reduction both indicated the presence of CuO in the composites. Other chemical bonds between Cu and O (CuOCuO and CuOO), which can only be found at the interface where functional groups were attached, disappeared after reduction. A summary of these results is shown in Figure 2.16.



**Figure 2.16** A) SEM image of CNT/Cu nanocomposites; B) EDX spectrum where the electron beam was focused on areas a, b, and c; C) TEM image showing the embedded CNT in Cu matrix and; D) FTIR spectrum for CNT/CuO and CNT/Cu powders (taken from Kim et al. [57]).

The group observed that the yield strength of a nanocomposite with 10 vol% CNT was 3 times higher than pure copper, and that the elastic modulus increased from 100 GPa for pure copper to 138 GPa. Experimental values obtained for moduli fell between calculated values using both the shear-lag [58], and Eshelby [59], models, which generally provide upper and lower bounds respectively, for strengthening due to composite reinforcement. This agreement between the estimated and measured values indicates that the stiffening and strengthening of the composite is primarily due to efficient load transfer between matrix and reinforcement. The covalent bonding of oxygen from the CNT surface to Cu matrix is the avenue through which load transfer takes place.

Several commonalities exist among the reviewed composite fabrication techniques. First, achieving a stable, homogenous dispersion of CNTs is the primary task for any processing route. With the exception of the work carried out by Ngo et al. [46] and Chai et al. [49], CNT powders were mixed, functionalized, polymer wrapped or Ni-coated before any composite fabrication took place. Not only is this process time consuming, but in the event a homogenous dispersion is in fact achieved, it is highly unstable and temporary. For thermal conductivity applications, polymer wrapping greatly increases the interfacial resistance. According to molecular dynamics simulations,

one physical nanometer of polymer coating on CNTs creates a 10-20 nanometer gap for thermal transport, effectively inhibiting phonon transport along CNTs [60].

In all of the literature surveyed in this thesis, the length of CNTs did not exceed 10s of microns. This is all in part due to the inability to achieve a stable dispersion of longer CNTs. Increasing length further increases surface area, and consequently, the strength of van der Waals forces which cause agglomeration. Additionally, very few methods allowed for the alignment of the CNTs within the composite.

This is unfortunate for those attempting to realize increased mechanical, thermal or electrical enhancement in composite materials. Short, unaligned, low concentration and agglomerated CNTs are not the reinforcement capable of producing radical property improvement. The yield strength of a MMC can be approximated as:

$$\sigma = \sigma_m (1 + V_f R) \quad (5),$$

where  $\sigma_m$  is the yield strength of the matrix,  $V_f$  and  $R$  are the volume fraction and strengthening efficiency of the reinforcement phase respectively. According to the generalized shear lag model,  $R$  can be approximated as  $S/2$ , where  $S$  is the ratio between the diameter and length of reinforcement, or the aspect ratio. According to this model, the aspect ratio of reinforcement is a very important in achieving rule of mixtures levels of strength. Though obviously there is great improvement to be had by incorporating longer CNTs, there is a caveat. The generalized shear lag model assumes perfect alignment of reinforcement within the matrix. Instead, most procedures reviewed exhibit randomly aligned networks of short CNTs in a Cu matrix, which means that even the short aspect ratio case is inflated.

It is apparent that other processing routes must be explored in order to achieve further property enhancement. This thesis details a novel processing route for the fabrication of CNT-reinforced Cu composites where the CNTs are dispersed, aligned and nearly 2 mm tall. In addition, the process is aqueous based and does not require intensive acid treatment or electrochemical equipment. This process involves functionalizing CNT arrays with atmospheric oxygen plasma, saturating the arrays with a highly concentrated copper salt in DI water solution, and then drying, calcination and reduction in hydrogen. The entire process, when completed at a lab scale, takes less than 24 hours including the growth of the CNT arrays, and the resulting composites show promising results in characterization.

## 2.4 Copper and Copper Compounds

Copper (Cu) is a transition metal that exhibits a characteristic red-orange color, and also has a unique set of physical and chemical properties. These defining qualities can be derived from the electronic arrangement,  $[\text{Ar}]3d^{10}4s^1$ . The energy difference of electron transitions between the filled d-shell and half empty s-shell corresponds to that of orange light, thus creating copper's defining hue. Compared to metals with incomplete d-shells, there is little covalent nature to copper's interatomic interactions. Instead the s-shell electron participates in weak metallic bonding, which leads to a material that has very high ductility and low hardness.

The low hardness of copper has great benefits for electrical and thermal conductivity, with copper having the second highest among pure metals at room temperature. For soft metals thermal vibrations of the lattice are very weak. As a result, resistance due to electron scattering on thermal vibrations is kept to a minimum and current densities up to  $3.1 \times 10^6 \text{ A/m}^2$  are achievable. Though metallic copper can be found in a pure state, it is more often found in a variety of compounds.

Copper primarily exists in two main oxidation states, +1 and +2. Copper(I) compounds are not only difficult to synthesize, but many are stable in water and therefore insoluble in aqueous solutions. Due to this fact, these compounds fall outside the scope of this thesis. Copper(II) compounds on the other hand are more easily abundant and have a variety of interesting properties and applications. The majority of these compounds exhibit square planar or distorted octahedral configurations about the copper ion, but distorted tetrahedral and five-coordinate systems can also be found. Due to the copper(II) ion's electronic state,  $[\text{Ar}]3d^9$ , the unpaired 3d electrons result in magnetic properties. In this thesis, focus has been placed specifically on copper salts because of their high solubility in aqueous solution and ease of manufacture.

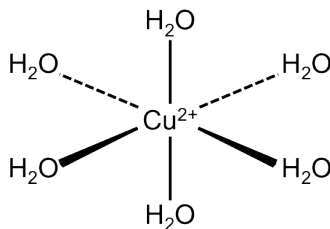


**Figure 2.17** In aqueous solution,  $\text{Cu}^{2+}$  ions form an octahedral metal aquo complex with six water molecules.

Like all metals, Cu forms coordination complexes with ligands in solution. In aqueous solutions, copper(II) salts exhibit high solubility while they dissociate and form complex ions with water. The complex ions are known as metal aquo complexes, and in the case of  $\text{Cu}^{2+}$ , six water molecules will form dative covalent bonds (where the oxygen donates both electrons to the bond) to the central atom. These primary molecules are H-bonded to secondary water molecules in the “bulk solution”, but they can also be rapidly exchanged. The octahedral structure that is formed is shown in Figure 2.17. Solutions made with copper(II) salts are generally blue or green in color as a result of the electronic interactions between the Cu ions and coordinating water molecules.

A solid product can be obtained from drying the Cu salt solution, and allowing it to crystallize. During drying, bulk water will evaporate, but the coordinated water molecules will remain to stabilize the newly formed crystal structure. This is known as water of crystallization and in the case of metal salts, water of hydration. Hydrated compounds are prevalent in nature as well as the laboratory. During crystal growth, lone pairs from a water molecule coordinate with cations, thus decreasing the effective charge of the compound and forming a more stable crystal structure. The degree of hydration for a particular compound is a definite stoichiometric ratio. Depiction of the chemical and crystal structures can be quite complex due to the competing covalent and H-bonding associations between the water and metal compound.

Water of hydration can be removed from the crystal lattice without a change in the chemical composition by controlling the temperature and/or pressure of the system in a process known as dehydration. Due to the water being trapped inside a crystalline solid, cracks and fissures are formed as a pathway for the water molecules to escape. Upon removal however, the crystal structure can potentially reorganize and recrystallize to form a new crystalline solid. The process of dehydration can cause changes in the stability and reactivity of the resulting material, but the anhydrous material will revert back to the hydrated structure once re-solubilized. Dehydration reactions are known to follow a nucleation and growth mechanism [61].

In addition to high solubility in aqueous solutions, most copper salts have the added benefit of being a suitable precursor for reduction to form pure, metallic copper powders. Various reducing agents such as carbon compounds have been used [62], but the prospect of using pure hydrogen is of recent interest to researchers [63–69]. High purities and fast reaction rates can be achieved due to the improved contact between a gas and solid as compared to solid-solid. Additionally, pure, uncontaminated hydrogen is largely abundant. In general, the procedure is to first dehydrate the

copper salt to remove water, and then flow hydrogen gas on the sample to allow for the reduction to take place.

According to the thermodynamic simulations of Luidold and Antrekowitsch [69], it is possible to obtain pure copper powders from copper oxides, chlorides, sulfides and fluorides, though literature detailing the procedure to do so is scarce. The precursors used for experiments in this thesis were chosen based on these findings, in addition to the extent of the salts' solubility in water.

The salts included copper sulfate pentahydrate ( $\text{CuSO}_4 \cdot 5\text{H}_2\text{O}$ ), copper nitrate hemipentahydrate ( $\text{Cu}(\text{NO}_3)_2 \cdot 2.5\text{H}_2\text{O}$ ), and copper chloride dihydrate ( $\text{CuCl}_2 \cdot 2\text{H}_2\text{O}$ ). General physical properties for each compound can be found in Table 2.1. An important piece of information on this table is the solubility of each compound in aqueous solutions, and how the solubility changes with increasing temperature. In the case of copper sulfate, the solubility increases over three times from 25°C to 100°C. This is an important fact for maximizing the copper content in solution, and thusly composites fabricated using the modified MLM procedure.

**Table 2.1** Measured physical properties of hydrated and anhydrous forms of copper sulfate, chloride and nitrate [70], [71].

Copper Salt	Degree of Hydration	Density g/cm <sup>3</sup>		Molar Mass (g/mol)		Mass % Solute in Aqueous Solution		
		Hydrate	Anhydrous	Hydrate	Anhydrous	0° C	25° C	100° C
Copper(II) Sulfate	5	2.284	3.603	249.7	159.62	12.4	18	43.5
Copper(II) Chloride	2	2.51	3.386	170.48	134.45	40.8	43.1	52.7
Copper(II) Nitrate	2.5	2.32	3.05	241.6	187.56	45.2	59.2	71

#### 2.4.1 Copper(II) Sulfate

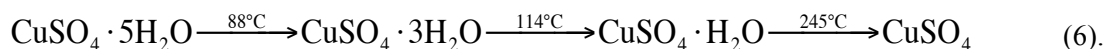
Of the three salts used in this thesis, copper(II) sulfate ( $\text{CuSO}_4$ ) was the most widely documented in terms of dehydration and reduction procedures. Copper(II) sulfate is a metal salt that can exist in various forms of hydration depending on environmental conditions. There are five water molecules in the fully hydrated form of copper sulfate. Four coordinate with each  $\text{Cu}^{2+}$  cation while one occupies space within the structure and is supposedly hydrogen bonded to the  $(\text{SO}_4)^{2-}$  anion, to form  $[\text{Cu}(\text{H}_2\text{O})_4]\text{SO}_4 \cdot 4\text{H}_2\text{O}$ , or more succinctly,  $\text{CuSO}_4 \cdot 5\text{H}_2\text{O}$ .

The earliest study on the dehydration kinetics of copper hydrates dates back to 1924 when Crowther and Coutts [72], utilized the new-fangled Oden-Keen Automatic Recording Balance for their work [73]. The scientists were able to put a known quantity of hydrated salt on the balance and

examine the rate of evaporation under high temperature. What they found were distinct changes in the evaporation rate, which they correlated to the existence of different hydration states of copper sulfate pentahydrate. Though revolutionary in its time, this study was fraught with uncontrollable experimental parameters due to the underdeveloped technology of vacuum science. Additionally, uncontrolled formation of dehydration centers on the crystal surface led to uncertainty in calculating the actual surface area that was contributing to evaporation.

In 1930, with the advent and improvement in vacuum science, Garner and Tanner [74], were able to replicate the early experiment in a more controlled environment. By continuously removing evaporated moisture from the sample chamber, a more accurate relationship between temperature and rate of evaporation was established. Interestingly, the group also found that rubbing the surface of a hydrated copper sulfate crystal with its anhydrous counterpart yielded a crystal surface with consistent nucleation of dehydration sites. This eliminated the difficulty and variability in the determination of crystal surface area so that a more exact relationship between the rate of evaporation and temperature could be established.

Less than a year later Hume and Colvin [75], tested the effects of pressure and water vapor on the dehydration and decomposition of copper sulfate. They too found that the decomposition rate was majorly linear from pentahydrate to monohydrate, but even still they did not discount the possibility of multiple reaction stages. Today's thermal analysis techniques have revealed the following decomposition profile:



At 88°C two water molecules are lost to form the trihydrate. Increasing the temperature further to 114°C yields the monohydrate, and the anhydrous salt is finally formed at 245°C. Continuing the heat the salt will yield that formation of CuO between 600 and 650°C [76].

Research in the reduction of copper sulfate began in 1956 when Hegedus and Fukker [77], studied both the dehydration steps and reduction steps of the hydrated salt. Samples were heated in atmosphere and continuously weighed to develop dehydration and decomposition profiles, which were in agreement with the previously mentioned work. Then hydrated salts were in an atmosphere of hydrogen to allow for the reduction reaction to take place. At 235°C the reaction commenced, forming SO<sub>2</sub> gas, and at 340°C the reaction was complete forming metallic Cu. The dehydration, decomposition and reduction profiles from this work can be found in Figure 2.18. Unfortunately, this

work was published in German and did not receive due attention by fellow researchers in the field until 1985 [66] even though work continued through the following decades.

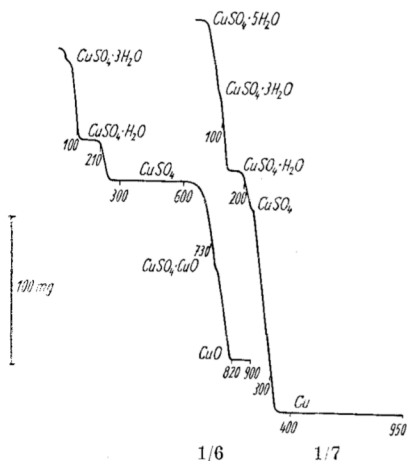


**Figure 2.18** The dehydration/decomposition (left) and reduction (right) profiles of hydrated copper sulfate salts (taken from Hegedus et al. [77]).

Almost 20 years later in 1973, Habashi and Dugdale [63], [64], published a procedure aimed to develop a fast, easily automated and compact method for the production of pure copper powders. Leach solution was obtained from copper ores and crystallized before undergoing gaseous reduction with  $H_2$ . Preliminary results showed that high purity metal powders could be obtained at temperatures as low as  $300^\circ C$ , though no pressure was reported. The reduction reaction that was initially reported was:



In this and later work however, it became evident that intermediate compounds were formed during the reduction based on experimental parameters like temperature and pressure.

Vijh and his colleagues [78] attempted to predict the compounds formed during reduction by analyzing the temperature at which reduction commences for a variety of sulfate compounds. Though no definitive correlation was found, a general set of equations showing an example of the wide array of possible products was proposed:



$\text{MSO}_4$  can be considered a general binary sulfate,  $\text{MO}$  is a metal oxide and  $\text{MS}$  is a metal sulfide.

Jacinto [65] and his colleagues theoretically and experimentally predicted intermediate and final reaction products for a wide range of temperatures. For all temperatures tested, X-ray diffraction analysis of the reaction products showed leftover reaction ( $\text{CuSO}_4$ ), and with the exception of 833 and 923K,  $\text{Cu}_2\text{SO}_4$  was found in all samples as well. Metallic Cu was successfully synthesized between 473 and 773K.

Sohn and Kim [66] used a nonisothermal technique to determine the kinetics of the hydrogen reduction reaction as a function of several parameters such as particle size, dehydration temperature, and hydrogen partial pressure. They found that the rate at which the reaction progresses is largely based on the partial pressure of  $\text{H}_2$ , as well as the amount of unreacted copper sulfate.

#### 2.4.2 *Copper(II) Nitrate*

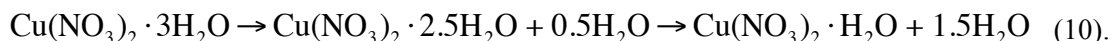
Copper(II) nitrate occurs in five different hydrated forms with tri- and hexahydrate being the most common. The hydrate is unique in that, unlike most copper(II) complexes which exhibit Jahn-Teller distortion of the Cu-O bonds, copper nitrate does not. Instead all bond lengths are equal due to the strong H-bonding in the complex, which limits the elasticity of the bonds.

Years of experimentation have determined that the nature of thermal decomposition of copper(II) nitrate depends greatly on experimental conditions, namely the system pressure. Earlier studies conducted in atmospheric pressure found it impossible to form the anhydrous salt [79–82]. Instead, most observed two or three stages of decomposition: melting of the hydrate (116-152°C), formation of  $\beta\text{-Cu}_2(\text{OH})_3\text{NO}_3$ , otherwise known as basic copper nitrate (199-217°C), and finally decomposition to  $\text{CuO}$  (263-310°C).

More recent experiments [83–87] conducted at reduced pressure utilized residual gas analysis (RGA) and secondary ion mass spectroscopy (SIMS) for spectral analysis of reaction by-products, shedding more light on the thermal profile of copper nitrate. At reduced pressure, thermal decomposition occurs in the solid state. After the initial dehydration, water and nitrogen containing species such as  $\text{NO}$  and  $\text{NO}_2$  were released. Upon release, the copper compound reorganized to form either basic copper nitrate, (also known as copper hydroxonitrate),  $\text{Cu}_2(\text{OH})_3\text{NO}_3$  (167-205°C) [85], or  $3\text{Cu}(\text{NO}_3)_2 \cdot \text{Cu}(\text{OH})_2$  (65-107°C) [83]. The final product of the decomposition was again  $\text{CuO}$ , which was found at a wide temperature range (182-312°C). In general it appeared that the thermal

transitions commenced at lower temperatures when compared to atmospheric pressure experiments. Additionally, although anhydrous copper(II) nitrate was not present as a solid product, researchers reported spectral signals of Cu containing ions, suggesting its presence in gaseous form. Authors proposed that the powder sublimates at high temperature, decomposes in gaseous form, and then re-solidifies at CuO [85].

Morozov and his colleagues went one step further and combined mass spectral analysis of the gas phase during thermal decomposition with X-ray diffraction (XRD) study of the solid intermediates and products [88]. They divided the decomposition into three distinct stages. During *Stage 1* (40-80°C), the as received salt,  $\text{Cu}(\text{NO}_3)_2 \cdot 3\text{H}_2\text{O}$  is dehydrated in a step-wise fashion:



XRD analysis definitively confirmed the presence of both of these hydrates. The dehydration process is accompanied by thermohydrolysis to form copper hydroxonitrate, as well as dissociation of released  $\text{HNO}_3$ :



The resulting copper hydroxonitrate was found both in crystalline ( $\alpha$ ), and amorphous forms. Continuing at higher temperature (80-100°C), results in further dehydration of  $\text{Cu}(\text{NO}_3)_2 \cdot \text{H}_2\text{O}$  to form a mixture of anhydrous  $\alpha$  and  $\beta$ - $\text{Cu}(\text{NO}_3)_2$ . In total, four different Cu-containing compounds were formed in *Stage 1*: amorphous and  $\alpha$ - $\text{Cu}_2(\text{OH})_3\text{NO}_3$ , as well as  $\alpha$  and  $\beta$ - $\text{Cu}(\text{NO}_3)_2$ .

*Stage 2* (100-150°C), of the thermolysis involves the sublimation of anhydrous copper nitrate and also the thermal decomposition of amorphous hydroxonitrate. At 143°C the gas analyzer read higher concentrations of  $\text{H}_2\text{O}$ ,  $\text{NO}_2$ , and  $\text{HNO}_3$  which corresponds to this decomposition:



The formation of CuO at such low temperatures is attributed to the lower system pressure and slow heating rate used for these experiments. The sublimation of anhydrous  $\text{Cu}(\text{NO}_3)_2$  results in the conversion of  $\alpha$  to  $\beta$  polymorphs so that Cu-containing intermediates include CuO and  $\beta$ - $\text{Cu}(\text{NO}_3)_2$  at the end of *Stage 2*.

During *Stage 3* (180-220°C), the majority of  $\text{HNO}_3$  signal is diminished and there are negligible Cu ions in the gas phase. This fact means that instead of the remaining anhydrous copper nitrate sublimating and turning to CuO (as was so in *Stage 2*), a different mechanism is in place. They proposed and confirmed the formation of an unknown oxonitrate:



This intermediate will continue its decomposition to form:



Again, the evolution of this intermediate phase is attributed to the slow heating rate used in experiments.

The thermal analysis of copper(II) nitrate is described as a competition of dehydration and thermohydrolysis processes. Step-wise dehydration, not seen before this article, was made dominate between these competing reactions due to the lowered pressure. Additionally, the complete conversion of hydrated copper nitrate to CuO can be completed at lower temperature.

Successful formation of CuO is important because it can easily be reduced to form pure metallic copper. This compound has been widely studied due to its use as a catalyst in many chemical reactions. Even still, there is much disagreement on the actual mechanism for reduction in whether it is direct or sequential [89],[90]. These discrepancies are likely due to differences in sample preparation and experimental parameters.

The first documented use of this technique dates back to the late 1870s [91],[92], when Wright et al. passed hydrogen gas at a constant rate through a U-tube containing copper oxide powder. By intermittently weighing the tube, they found that there was an "incubation" period where the rate of conversion was close to zero, followed by an increasing rate of reaction until completion. They also found that decreasing the temperature (130-257°C was tested), increased the length of the incubation period. They hypothesized that the incubation period lasted until a nucleus of pure copper was formed, and then the reaction progressed at an increasing rate due to the formation of new Cu-CuO interface.

In 1921, Pease and Taylor confirmed the earlier hypothesis [93]. The incubation period was all but eliminated by adding a metallic Cu "nucleating agent" to the CuO powder. Their findings showed that the reaction was autocatalytic, with Cu acting as the catalyst. Additionally, they found that introducing water vapor into the reaction chamber retarded the formation of an initial Cu nucleus, thus increasing the length of the incubation. Once formed however, water vapor had negligible affect on the rate of the reduction reaction. The introduction of excess oxygen in the system slowed the reaction rate.

Until recently, it was generally agreed that the following reaction dominated the reduction of CuO:



Current work focused on conducting the reaction at reduced pressure however has led to conflicting results. Rodriguez and colleagues conducted a thorough examination of the microscopic mechanism of H<sub>2</sub> reduction of pure CuO powder *in situ* using time-resolved XRD, XPS and Auger electron spectroscopy (AES) [94]. Powder samples were isothermally heated to temperatures between 150-300°C as a mixture of 5% H<sub>2</sub>/95% He gas was flowed in the reaction chamber at a rate of 20 cm<sup>3</sup>/min. After a 15-minute incubation period of no reaction, diffraction lines for metallic Cu began to appear without any sign of intermediate phases. Increasing the temperature only yielded a decrease in incubation time.

Reducing the volume of gas flow however slowed the chemical reaction enough that diffraction lines for Cu<sub>2</sub>O became visible. Here, increasing the temperature (400-600°C) produced more Cu<sup>1+</sup> compounds compared to other processes. Comparing the intensities of the CuO and Cu<sub>2</sub>O signals lead the researchers to conclude that the following reactions take place simultaneously:



and



Here, Equations 17 and 18 are sequential reactions while 19 is the familiar direct reduction.

The direct reduction of CuO to Cu dominates at lower temperatures. It should be noted that this group also found that the previously mentioned nucleation model for atmospheric pressure reductions still applies for reduced pressure reductions due to the presence of an incubation period. The incubation period can however be drastically shortened by introducing defects into the surface of CuO. This allows for high efficiency adsorption and dissociation of H<sub>2</sub> on the oxide surface. When ample H<sub>2</sub> is available for reduction the escape of oxygen from the bulk is a rate-limiting factor.

### 2.4.3 Copper(II) Chloride

Copper(II) chloride dihydrate (CuCl<sub>2</sub> •2H<sub>2</sub>O) is the primary hydrated state of this copper salt. The anhydrous powder is brown and will turn a blue-green color upon rehydration. CuCl<sub>2</sub> •2H<sub>2</sub>O adopts a distorted octahedral geometry where it is surrounded by two water and four chloride ligands,

which bridge asymmetrically due to Jahn-Teller effects. The anhydrous form adopts a distorted cadmium oxide crystal structure due to the strong polar nature of the chloride ions. Copper(II) chloride begins to decompose to copper(I) chloride at 300°C [76].

It is generally accepted that the dehydration of copper(II) chloride takes place in a single step. Using thermogravimetric analysis (TGA), Mohamed and Halawy confirmed that the anhydrous salt could be obtained in a one-step dehydration over a range of heating rates (3, 5, 7, and 10°C/min). As the rate of heating increased, the temperature at which maximum weight loss occurred increased as well [95].

No literature was found that directly reduced copper(II) chloride to metallic Cu. Instead, most studies began with copper(I) compounds (CuCl). This could be due to the fact that CuCl<sub>2</sub> decomposes to CuCl at moderately low temperature (300°C). Due to this fact, the literature presented concerns the use of CuCl as the reduction precursor. The first mention was in 1932 where there was brief mention of the growth of copper filaments using a CuCl precursor and hydrogen [96]. Brenner included the salt in his massive characterization of metal salts that could be reduced to form metal whiskers. They were produced by flowing hydrogen gas over CuCl powder at high temperature (430-850°C) with the optimum temperature identified as 650°C.

There are recent examples of using copper compounds as precursors for copper deposition processes such as atomic layer epitaxy (ALE) [97], and low pressure chemical vapor deposition (LPCVD) [98]. Others demonstrated these processes using volatile Cu<sup>1+</sup> and Cu<sup>2+</sup> organometallic precursors and complex reducing agents, but the hydrogen reduction reaction makes it possible to use simple copper halides to achieve the same results. Bourhila et al. synthesized a gaseous copper compound precursor by chlorination of pure copper foil. From previous work [99], they determined that at low pressure (1 Torr) above 377°C, they achieved a high yield of pure, gaseous Cu<sub>3</sub>Cl<sub>3</sub>. This precursor was flowed into a heated reaction chamber where it was allowed to deposit on a substrate without any reducing agent. By analyzing the XRD spectra for the as-deposited films for a variety of temperatures they determined that pure CuCl and CuCl<sub>2</sub> were deposited at temperatures above 420°C and below 380°C respectively. The following experiments were carried out using CuCl, though there was no mention as to a reason why.

In an excess of H<sub>2</sub> at temperatures above 300°C, the reduction process takes place as follows:



By optimizing the reaction conditions, the group was able to maximize the deposition rate of CuCl and the subsequent reduction to form metallic copper. Decreasing the total pressure of the system

decreased the stability of the CuCl phase, thus leading to more rapid reduction. Other optimized conditions were temperature = 400°C, pressure = 1 Torr, H<sub>2</sub> flow = 500 sccm for 10 minutes. Using these parameters, low impurity films were deposited at a rate of 150 nm/min.

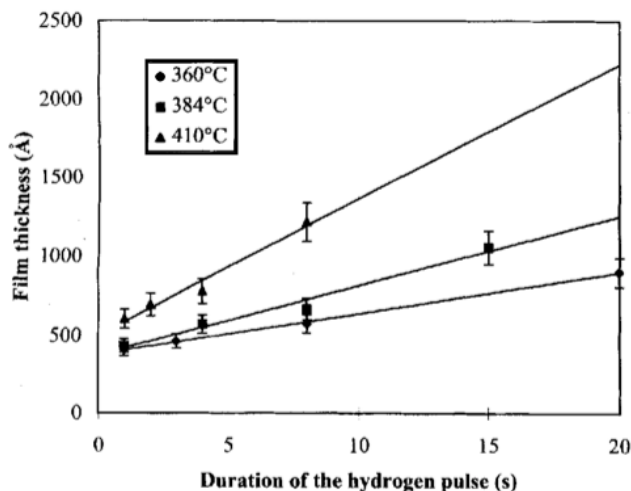


**Figure 2.19** Metallic copper film thickness as a function of deposition temperature and duration of hydrogen pulse (taken from Martensson et al. [97]).

Atomic layer epitaxy (ALE) is the other deposition method that has been used to deposit copper films while utilizing hydrogen reduction of copper compounds [97]. ALE is similar to LPCVD in that it requires a low-pressure atmosphere, but instead of the deposition process being continuous, it progresses in a rapid series of cycles. To perform the deposition, CuCl was evaporated at 350°C and then introduced into a heated reactor. After being allowed to adsorb to a tantalum substrate, the reactor was purged with N<sub>2</sub> gas and then a timed pulse of H<sub>2</sub> gas was introduced to commence the reduction. The reactor was again purged, which ended the cycle. The process was repeated to form 300Å thick layers of metallic copper, averaging 0.8Å/cycle (400Å/hour). Experiments were conducted at 10 Torr with temperatures between 360-410°C and H<sub>2</sub> pulse times of 1-20 seconds. As seen in Figure 2.19, for pulses up to 20 seconds, a linear relationship between the deposition rate and pulse duration was determined. Additionally, the deposition rate was found to increase with increasing temperature and more than doubled from 360 to 410°C.

The copper salts for this research were chosen based on their ability to be easily reduced to metallic copper, but also because of their high solubility in water. CNT arrays can be filled with liquids, but not before undergoing functionalization. The surfaces of pristine CNTs are covered in non-polar, non-reactive C-H terminations [35–37]. Additionally, once assembled in an array structure, the surface roughness is exceedingly high. The combination of these factors yields a chemically and physically hydrophobic structure [100–102]. Without treatment, wetting of the CNT array by an aqueous solution is virtually impossible.

## 2.5 Wetting & Surface Tension

### 2.5.1 Wetting Behavior of Rough Surfaces

In the 1930s and 1940s researchers Wenzel [103], and Cassie and Baxter [104], each proposed models for the wetting of rough surfaces. First, Wenzel established the case for homogenous wetting where the water droplet is fully supported by one and only one “type” of surface. The equation for apparent Wenzel contact angle,  $\theta_w$ , is:

$$\cos\theta_w = r \cos\theta_Y \quad (21),$$

where  $\theta_Y$  is the Young contact angle and  $r$  is the roughness ratio which is a comparison of the actual area of a surface compared to the nominal area as if the surface were modeled as a flat, featureless film. For a surface that is hydrophobic due to chemical structure, an increase in surface area through the creation of roughness will yield a more hydrophobic state.

The Cassie-Baxter model explains what is known as the heterogeneous wetting regime, or when multiple “types” of surfaces support a water droplet. A pertinent example of a heterogeneous surface is CNT tips and air interstices. The equation for apparent Cassie-Baxter contact angle,  $\theta_{CB}$ , is:

$$\cos\theta_{CB} = r_f \cos\theta_Y + f - 1 \quad (22),$$

where  $f$  is the fraction of the surface area that is actually wet by the droplet, and  $r_f$  is the roughness ratio of the wetted area. If the fraction of air interstices decreases, either by changing the system or water filling the air interstices,  $f = 1$  and  $r_f = r$ , making this equation equivalent to Wenzel.

Conversely, increasing the amount of air supporting the droplet or decreasing the actual area of sample in contact with the droplet will push the apparent contact angle towards values of 180°.

### **2.5.2 Controlling the Wetting Behavior of Carbon Nanotube Arrays**

At a basic level, CNTs can be thought of as rolled sheets of graphite. Largely comprised of  $sp^2$  C-C bonds, CNTs grown from hydrocarbon gases using chemical vapor deposition (CVD) have C-H terminations at the surface as well [35], [36]. Although there is considerable debate as to what the exact contact angle of graphite is, it is generally agreed to be below 90°, and certainly not in the superhydrophobic regime. Initially perplexing, but as it turns out chemical structure is only one part of the “Will it wet?” equation. Additional geometrical factors like roughness and porosity play a significant part as well [105]. In many ways, CNT arrays mimic the Lotus flower and exhibit what is called the Lotus effect. This is the ability of water droplets to roll and bounce off the surface of the Lotus leaf, while removing dust particles and debris in the act of “self-cleaning”. The Lotus effect is created from not only the surface chemistry, but also the hierarchical micro and nano-sized features that cover the surface of the leaf, creating a rough, heterogeneous structure [106].

The Cassie-Baxter model most adequately explains the CNT array system. A highly heterogeneous surface with a high roughness ratio, which allows for a great deal of air to be trapped underneath a water droplet while only a small total area of CNT tips are in contact. Many research studies have focused on the superhydrophobic qualities of CNT arrays [102], [106–109], but there is a relative lack of understanding in creating a hydrophilic state, especially while maintaining the integrity of the delicate CNT array. Until the liquid is “coaxed” to replace the air in the system, it will not wet. Developing a full understanding of how CNTs interact with liquids is a fundamental issue that, once realized, has the capacity to greatly benefit any researcher in the field.

It should be noted here that this area is indeed related to the dispersability and solubilization of CNT powders, which involves the employment of surfactants and covalently attached functional groups to overcome the van der Waals attractions and therefore create stable dispersions. There is, however, added complexity in working with aligned CNT arrays. Instead of an unaligned powder, arrays are grown vertically on substrates to lengths of many millimeters. In this morphology, the anisotropic properties of the CNTs can be more adequately utilized, both because of the high level of alignment, but also because in this state there is minimal bundling due to van der Waals attractions.

With that said, traditional functionalization techniques, specifically wet chemistry, are not available to those researchers working with arrays. Strong capillary forces in the array destroy the

structure upon wetting and drying [110]. Less traditional yet effective techniques such as oxidation, plasma, ultraviolet (UV)/ozone and energetic particle bombardment were developed as tools for manipulating surface and wetting properties. Each of these techniques though demonstrated to make CNT arrays wettable, cause varying degrees of damage to the CNT structure in the process. For many applications it is important to maintain the superior physical properties of the CNTs, so it is crucial to cause as little permanent damage as possible. A more detailed explanation of the mechanisms for various oxidation methods and plasma treatments follows.

### 2.5.2.1 Oxidation Methods

Pavese and his colleagues completed one of the more thorough theoretical and experimental works found by this author [111]. By comparing the wetting states of two CNT morphologies, vertically aligned CNT arrays and entangled mats, the effect of structure on contact angle can be elucidated. They found the initial contact angle of the aligned samples to be  $176^\circ$ , while the unaligned mats had a lower angle of  $144^\circ$ . This was explained by comparing the relative amount of surface in contact with the droplet. It is logical to reason that CNT tips have less contact area than CNT sides. This was theoretically confirmed, finding that  $f_{aligned}=0.0027$  and  $f_{mat}=0.21$ . Being the same material, the sample with more relative area in contact with the water droplet had a lower contact angle in agreement with Cassie-Baxter.

Next, they examined two methods of chemical oxidation; acid treatment and application of a bias voltage across the material. Acid treatments are commonly used to functionalize CNTs with oxygen-containing groups like carboxyl (-COOH) and sulfonic (-SO<sub>3</sub>H) acid groups. Although they were able to attach enough polar groups to achieve a wettable state ( $\theta$  decreased from  $176^\circ$  to  $25^\circ$ ), there was a large amount of macroscopic damage to the array. Oxidation induced by bias voltage application yielded a non-uniform distribution of functional groups, and the contact angle varied widely from  $50^\circ$  to  $100^\circ$  on the same sample [111].

Annealing and graphitization are additional methods used by researchers to control the reactivity of CNTs. Ideal CNTs are modeled as being perfect cylinders of C-C bonds, axially arranged in hexagons and heptagons. In reality, especially for CNTs grown via CVD, the walls are full of defects, while the tips and outer walls are terminated with C-H groups and sometimes even layers of amorphous carbon [35], [36]. For researchers, these imperfections are expressed in the underperformance and unpredictability of the material. Therefore, high temperature annealing is used

to graphitize the CNTs while also removing surface terminations. Obviously this has implications for manipulation of surface energy as well.

Mattia and colleagues reported on the effect of annealing temperature on both the wetting properties as well as the electrical conductivity of CNT arrays. CNT samples were annealed under vacuum at temperatures ranging from 900 to 2000°C. It should be noted that in vacuum, a minimum temperature of 1000°C is required to break the bonds of functional end-groups. Using transmission electron microscopy (TEM), it was confirmed that disorder in the CNT wall structure began to decrease at 1500°C and almost perfectly ordered graphite planes were seen at 2000°C.

Disappointingly, the group chose to measure the contact angles on CVD-carbon films instead of the actual CNT arrays. Although the chemical contribution for both systems is still intact, the usefulness of the data is limited for researchers working with arrays. Regardless, the group found that contact angle increased nearly linearly from 44° for as-made films to 77° for samples annealed at 2000°C. When the contact angle was plotted against the graphite crystallite size, the group found that there was an initial steep change in contact angle, and then a leveling off after 1500°C. This was attributed to the initial changes in surface chemistry caused by the breaking of functional group bonds, followed by the substitution of graphite edge sites with graphite planes. Again, these contact angles were grossly underestimated because they did not take into account the geometrical contributions of the array. It is, however, of critical importance to understand the interactions at all levels of the hierarchy.

It is interesting to mention that during environmental scanning electron microscopy (ESEM) characterization of the annealed CNT samples, the group noticed that water had actually condensed on the surface and inside the walls of the more hydrophilic samples. Because of Laplace pressure, the high curvature of the inner interface of the CNTs allowed for condensation inside the tube structure. This group also demonstrated a “pumping” action of sorts by making one end of a CNT more hydrophilic than the other. These results were among early findings that led to much of the interest and excitement in using CNTs for nanofluidic channels. It clearly demonstrates the importance in understanding the mechanisms for wetting, as well as developing methods for controlling wetting behavior as well [112].

Aria et al. [113], used ultraviolet (UV)/ozone, which is a well-known dry-oxidation process, to tune the wettability properties of vertically aligned CNT arrays. The process was successfully demonstrated on SWNTs dispersed in ethanol in earlier work by Banerjee et al [114]. By modifying reaction parameters and reagents, they were able to control the relative proportions of various

functional groups such as carboxylic acids/esters, ketones/aldehydes, and alcohols. Aria adapted the technique for functionalization of CNT arrays, meaning that liquid phase processing was avoided to prevent degradation of the CNT alignment within the array. The samples were subjected to UV radiation for increasing durations of time, which caused local bond breakage to the CNT ends and outer walls. Simultaneously, surrounding ozone oxidized the defective sites to form polar functional groups. These groups allow for hydrogen bonding between the CNT and water, resulting in a wettable structure.

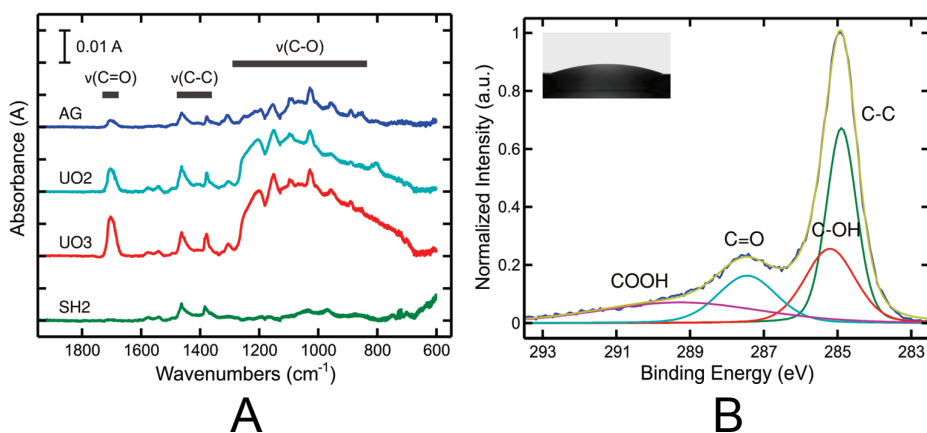


**Figure 2.20** A) FTIR spectra of MWNT arrays with various degrees of oxidation showing oxygen-containing functional groups; B) high-resolution XPS spectra of C 1s peak of UV/ozone treated MWNT array (taken from Aria et al. [113]).

The presence and identity of functional groups was confirmed using FTIR and XPS characterization, which is shown in Figure 2.20. Additionally, SEM verified that repeated treatments do not damage the physical structure of the CNTs or the array. Finally, it is interesting to note that short ( $14 \pm 4\mu\text{m}$ ), MWNT arrays were used on purpose in this work to reduce the time required for treatment. They state that a 1 mm tall array would require 4 hours of UV/ozone treatment in order to attain a wettable state.

### 2.5.2.2 Oxygen Plasma Treatment

The first application of atmospheric plasma to CNTs [115], was to create nanopores, or controlled defects, in pristine MWNTs in order to enhance their performance in hydrogen storage

applications. A line-shaped plasma, powered by a 3kV AC field, was generated with 2% oxygen in helium, and the vertically aligned arrays were treated for 15 minutes. Analysis of the Raman spectra before and after treatment showed that the  $I_G/I_D$  ratio decreased from 1.8 to 1.2, indicating the formation of defects in the MWNTs. In addition to the creation of defects via carbon vacancies, the etched atoms were found to form amorphous structures on the CNT walls.

Ramos et al. [116], first examined the effects of oxygen plasma on the wettability of vertically aligned CNT arrays. The plasma treatment was applied by a pulsed, direct current 700V field with an oxygen flow of 1 sccm at a pressure of 80 mTorr for 2 minutes. Pristine arrays exhibited an average contact angle of  $142^\circ \pm 6$ . After plasma treatment, the arrays were fully wetting as a result of oxygen functionalization of the CNT tips. XPS spectra of pristine and treated arrays (see Figure 2.21), show an increase in the intensity of the O 1s peak as well as a shift and broadening of the C 1s peak, which has been attributed to a chemical shift caused by a highly oxidative environment [117].

The surface tension of as-grown and treated arrays was evaluated by accounting for the polar and dispersive components of wetting. The Owens and Wendt method [118], uses various liquids with different surface tensions and polarities to generate a plot where the slope and y-intercept correspond to the polar and dispersion components of surface tension, respectively. They found that the polar component was more dramatically altered following oxygen plasma, meaning that the physical structure of the CNTs was majorly unaltered. Instead, the observation of a wetting state could be attributed to the change in polarity of the tips of the CNTs due to oxygen functionalization.

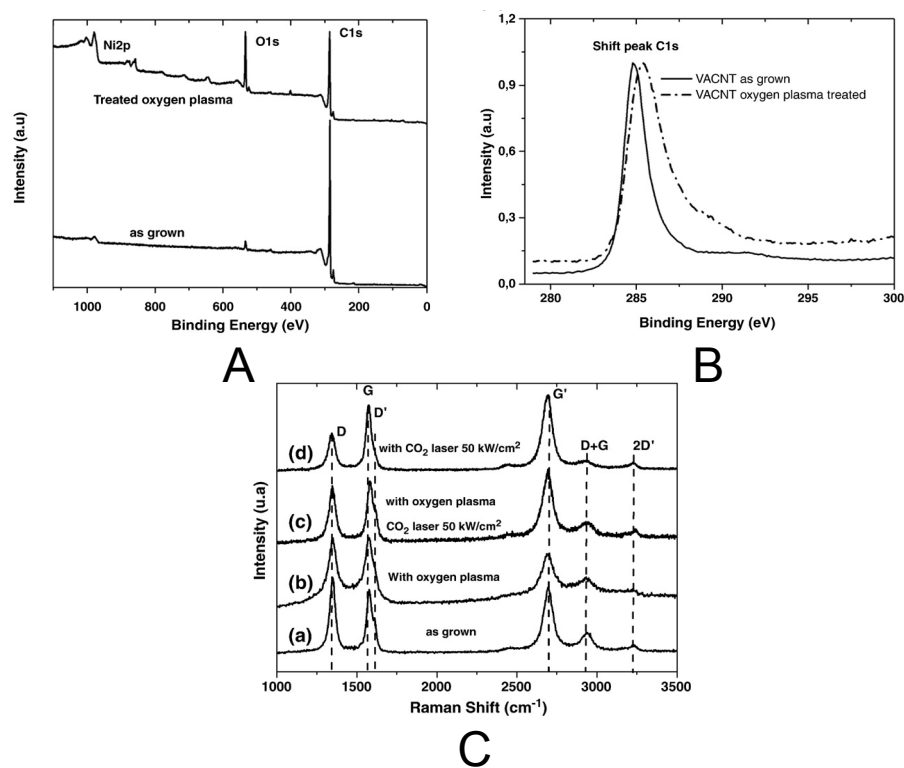


**Figure 2.21** A) XPS survey scan of as-grown and treated vertically aligned CNT arrays; B) high-resolution XPS C 1s peak of as-grown and plasma treated vertically aligned CNT arrays and; C) Raman spectra of pristine and treated arrays (taken from Ramos et al. [116]).

The same research group went to demonstrate full recovery of super-hydrophobicity by treating the wettable arrays using CO<sub>2</sub> laser irradiance [119]. This effect was explained by local heating of the CNTs induced by the laser irradiation. The high rate of heating not only changed the surface roughness of the array, but it also heated the sample enough to evaporate the oxygen terminations on the CNT surface. The effects could also be seen in the changes in the Raman spectra for the different samples. Though oxygen plasma caused a decrease in the  $I_G/I_D$  ratio, CO<sub>2</sub> laser irradiation on pristine CNTs actually increased the ratio, corresponding to a "purification" of the array. Xiaodong et al. previously demonstrated this effect by using laser irradiation to clean amorphous carbon from aligned CNT arrays [120]. The  $I_G/I_D$  ratio of samples that had first been plasma treated, and then laser irradiated remained unchanged between treatments, signifying the presence of permanent CNT surface defects resulting from oxygen plasma etching.

### 3 Experimental

#### 3.1 Equipment Preparation

##### 3.1.1 Construction of Low Pressure Chemical Vapor Deposition Reactor

Chemical vapor deposition is widely regarded as a superior method for the rapid growth of quality CNT arrays. Because of the ability to easily scale up the growth method for large-scale array growth a low-pressure CVD (LP-CVD) system was custom built in house.

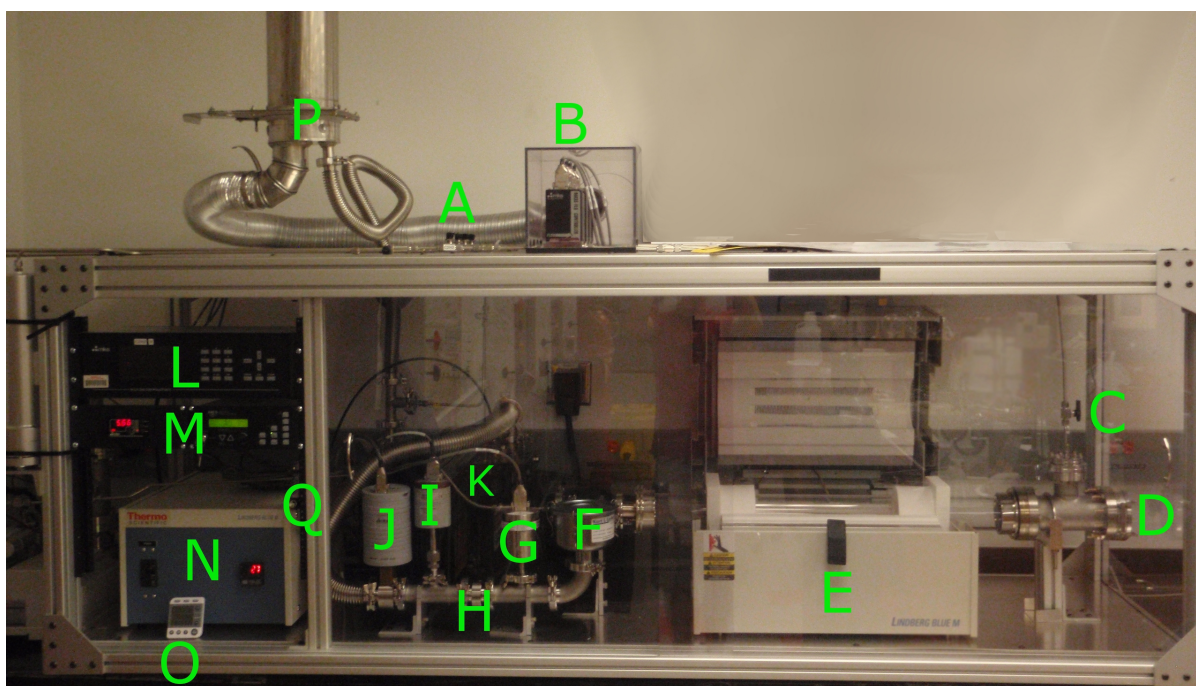


**Figure 3.1** Picture of low-pressure chemical vapor deposition reactor built in-house for chlorine-mediated carbon nanotube synthesis.

The entire assembly is housed inside an extruded aluminum frame that allows for the incorporation of Plexiglas polycarbonate sliding doors. On top of the frame, stainless steel gas lines lead from the gas cylinder cabinet to four, two-way valves (A), which lead to four corresponding mass flow controllers (MFCs) (B), and are mounted in an exhausted box. After the MFCs the four independent gas lines combine into a single one before entering the growth chamber on the right side.

A two-way valve (C), is mounted just above the furnace inlet to protect the gas lines when the furnace assembly is at atmospheric pressure.

The chamber is made of a 76 mm diameter quartz tube, (also referred to as the outer tube), that is fixed on both ends with aluminum fittings. On the right side there is a quick access door (D), with a quartz window that allows for viewing inside the chamber during growth runs. The tube assembly is suspended inside a horizontal tube furnace (E), with a 12-inch central hot zone. A 64 mm diameter quartz tube (also referred to as inner tube), that holds the samples and catalyst is inserted inside the outer tube during growth runs.

Immediately to the left of the primary tube is a particle filter (F), to prevent contamination of the pumping side of the assembly. Parts G and I are separate pressure gauges for measuring upper and lower ranges, respectively. The gauges are separated by the main vacuum valve (H), which allows for manual isolation of the tube assembly from the vacuum pump (K). All gas pumped from the furnace is fed to the main exhaust line (P). To the left of the gauges is the automatic pressure control valve (J). It is a digitally controlled butterfly valve whose position (0% = fully closed, 100% = fully open), is regulated according to the user selected pressure set point.

On the far left side is the electronics rack where the digital flow controller (L), low and mid-range pressure controller and displays (M), and furnace controller (N), are housed.

### ***3.1.2 Establishing Growth-Run Procedure***

A major goal in the design and construction of the LP-CVD system was to eliminate as much variation and unpredictability as possible. Similar care was taken in planning lab and growth procedures. By ensuring that adequate time was spent preparing for runs as well as cleaning up afterwards, greater reliability in array quality could be achieved. A growth template was developed that allowed for the tracking of important information about the furnace performance and experimental results.

Before loading the quartz substrates into the furnace, they were thoroughly cleaned by first burning them in air at 800°C, and then etching them in a dilute hydrofluoric acid (HF) bath for 1.5 hours. Even for brand new substrates, this ensures that all traces of machine grease have been removed as well as any other impurities. Other quartz accessories used during growth such as the sample stage and boat were also burned after every growth run, and then periodically etched as well.

After etching, the quartz was rinsed with deionized (DI) water and then dried with compressed nitrogen gas. The newly etched substrates were placed on the sample stage and then

loaded inside a freshly etched quartz inner tube. The placement of the sample stage was decided based on data taken from repeated growth runs. In order to ensure that the samples will be fully in the growth zone, the leading edge of the platform should be 16 inches from the left side of the tube end.

Iron(II) chloride ( $\text{FeCl}_2$ ) powder was stored in a sealed container inside of a desiccator to ensure minimal exposure to water vapor. Before growth, an appropriate amount of  $\text{FeCl}_2$  powder was weighed and poured into the quartz boat. The boat was then loaded into the center of the inner quartz tube.

Once the substrates and catalyst powder were loaded, the inner tube was carefully slid into the outer quartz tube of the furnace. The trailing edge of the inner tube was pushed flush to the end of the furnace assembly for every growth run to eliminate variability in gas flow profiles inside the tube. After sealing the access door of the furnace, the main vacuum valve was slowly opened to begin pumping the system down.

The system was generally pumped down for at least 2 hours or until the pressure fell below 10 mTorr. Adequate pump down time allows for the removal of most air impurities and water vapor from the system, as excessive impurities can cause variations in growth results. The base pressure of the system was logged for record keeping and the temperature ramp commenced.

The fastest possible ramp rate was used to quickly heat the system to the desired temperature.  $\text{FeCl}_2$  is vaporized around  $550^\circ\text{C}$  in vacuum so the time spent in the vapor phase was kept to a minimum in order to maintain a high concentration of catalyst vapor in the hot zone of the tube.

The vaporization of water from the catalyst powder as well as the vaporization of the catalyst itself causes the base pressure of the reactor to rise during the heating program. The maximum pressure reached during the ramp was recorded to indirectly probe the pumping efficiency of the vacuum pump as well as the degree of hydration of the catalyst powder. The pressure of the system was again noted when the temperature set point was reached. Again, this provides information about the vacuum pump performance, but also about the conditions of the growth environment prior to the sensitive process of CNT nucleation. Currently, little is understood about the requirements for CNT nucleation for CM-LPCVD, but the collection of several key pieces of information over time provides valuable data to not only gauge performance, but also the potential for greater understanding.

Upon reaching the desired growth temperature, the automatic pressure control valve was first closed (position = 0%), before the growth pressure set point was selected. The main reason for this was to provide consistency between growth runs. For each set point, the automatic pressure controller has a corresponding set of feedback control parameters (gain and lead). These parameters were

carefully optimized so that once engaged, the pressure inside the tube quickly met the set point without overshooting. Changing parameters like the gas flow or the starting state of the valve can cause unwanted variation between experiments.

After selecting the desired pressure set point, the appropriate MFCs were simultaneously opened, allowing the growth gases to fill the chamber. Once the pressure rose and stabilized, the growth timer was started.

An additional indicator of the system performance is the position of the automatic control valve during growth. As there is both gas flow and chemical reactions taking place inside the tube, it is normal for the position to change slightly, but it should be similar to other growth runs. If the position is significantly different this could be indication of diminishing pump performance, a clogged filter or an issue with the growth run itself.

Once the growth was completed the flow of gases was stopped, the automatic control valve opened, and the system was purged with Ar gas for two minutes. The furnace-heating program was stopped, and box fans were pointed on the hot zone to promote faster cooling. To prevent oxidation of the CNTs the system was not returned to atmospheric pressure until the temperature fell below 150°C.

The quick access door of the furnace was unlatched and the main pumping valve closed before refilling the tube with Ar gas. The inner tube was carefully removed from the furnace, and transferred to the fume hood. Before removing the sample stage from the inner tube, data was recorded about the “growth profile” of the inner tube. As seen in Figure X, there are various zones along the length of the tube, the most important being the dark black growth zone. The position of this zone relative to the end of the tube, as well as the length of the zone is recorded in the growth template. This information has helped predict the location of the growth zone as well as monitor changes in the growth profile for various experiments. Once the CNT arrays were removed and stored, the inner tube was cleaned by pushing excess growth into a waste container. The outer tube was vacuumed to remove particulate matter, and both tubes were thoroughly cleaned with ethanol.

As mentioned before the inner tube, quartz boat and sample stage were all loaded back in the outer tube and burned at 800°C in air to remove remaining carbonaceous species. Once cooled, the tube was etched in dilute HF for 1.5 hours, rinsed, dried and thus ready for the next growth run.

### 3.1.3 Growth Parameter Optimization

There are many parameters that can affect CNT arrays growth, but temperature, pressure, catalyst weight and gas flow were identified as the most important to control. Initial growth conditions were selected based on those used by Inoue et al. [28]. One gram of FeCl<sub>2</sub> catalyst powder was placed in a quartz boat and the tube was allowed to pump down to an ultimate pressure of 5 mTorr over several hours. The tube was heated to 820°C at a heating rate of 63°C/minute, which was the fastest allowed by the furnace controller.

When the furnace reached the growth temperature, acetylene (C<sub>2</sub>H<sub>2</sub>) gas was flowed at 450 sccm. A digital pressure controller maintained a constant pressure of 8 Torr during the experiment. After 10 minutes, the process was halted by turning off the furnace and purging the system with Ar gas. Box fans were pointed onto the system to speed cooling. When the tube reached 100°C, the inner tube was removed for sample retrieval and cleaning.

During many of the initial experiments, only short array growth (< 0.5mm) was seen, and there were obvious inconsistencies on the quartz substrates themselves. On many samples arrays would start at 0.5mm tall on the leading edge, and taper to bare quartz at the end. This effect was attributed to two main causes. First, the placement of the substrates may have been outside the growth zone inside the tube. Generally, there is a 6" zone of array growth where the center 4" is the tallest and most consistent area. The other cause for array taper was due to gas flow effects inside of the tube during growth. Ideally the gas flow inside the tube would be molecular, but due to the large diameter and chamber pressure, it was perhaps more correct to approximate the flow as viscous or laminar. The more irregular the gas flow is inside the tube, the higher propensity for inconsistencies in array growth throughout the tube cross-section. Lowering the pressure in the system to 4 Torr helped to alleviate this effect.

Initial experiments yielded arrays that grew on either side of the central heating zone in the tube furnace. Taller arrays were also found on the surfaces of the quartz boat. These results led us to believe that the initial selected temperature was too high because the furnace temperature decreases from the center outward to the ends. Also, the thermal mass of the quartz boat is much greater than that of the substrates. This meant that the temperature on and surrounding the boat was lower.

As the growth temperature was lowered from 820°C to 740°C, the two separate growth zones migrated toward the center of the quartz tube and combined. Additionally, lowering the pressure not only eliminated flow effects, but also allowed for the growth of spinnable arrays. This result agrees

with Inoue et al. as they found that arrays grown at 10 Torr adhered strongly to the substrate while those grown at 4 Torr released easily and were spinnable.

Adjusting the  $C_2H_2$  flow became necessary after decreasing the pressure because this also decreases residence time in the furnace. By increasing the flow from 450 to 600 sccm, the height of the arrays increased, nearing the 1 mm range. This was accomplished without suffocating the growth of creating additional flow effects.

Chlorine gas (0.4%  $Cl_2$  in Argon) was added to increase the growth rate and maximum height of the CNTs. For the same set of growth parameters (760°C, 4 Torr, 1g  $FeCl_2$ , 600 sccm  $C_2H_2$ , 10 minutes), the height of the grown arrays doubled upon the addition of 600 sccm of Ar +  $Cl_2$  during growth. Although the exact mechanism was not known at the time, it is now presumed that the  $Cl_2$  gas not only participates in the dehydrogenation of  $C_2H_2$ , but also reacts with Fe catalyst particles to re-form  $FeCl_2$ . Future work will focus on testing the validity of this assumption. Overall, it was determined that the optimal conditions for growth of consistent, 2mm CNT arrays were 1g  $FeCl_2$ , 760°, 2-5 mTorr, 600 sccm  $C_2H_2$ , and 400 sccm Ar +  $Cl_2$  for 20 minutes.

## 3.2 Material Preparation

### 3.2.1 Carbon Nanotube Array Growth

Arrays for this thesis were grown on 25x25 mm and 13x13 mm quartz substrates. They were first burned at 800°C in air for 10 minutes, and then etched in dilute HF for 1.5 hours before being labeled with a diamond scribe and weighed. The substrates were placed on the sample stage and loaded into the inner quartz tube. One gram of  $FeCl_2$  catalyst was poured into a small quartz boat, and loaded into the middle of the inner tube as well.

The system was pumped down until the base pressure was less than 10 mTorr, about 2 hours. Then the furnace was heated to 760°C, and the automatic pressure control set to maintain the growth pressure at 5 Torr. Acetylene and Ar +  $Cl_2$  gases were flowed at 600 and 400 sccm respectively, thus nucleating CNT growth.

After 20 minutes the growth gas flow was stopped and the system was purged with pure Ar for two minutes. The furnace was allowed to cool with the aid of fans until it reached a safe working temperature, around 100°C. The furnace was then returned to atmospheric pressure, and the samples

were retrieved. Before further sample processing, the edges of the sample were carefully cleaned with a razor blade and then weighed again to record mass added from the array growth.

### **3.2.2 Post-Treatments**

As-grown CNT arrays are rarely ready for immediate incorporation into composites and must be post-treated to achieve desirable properties. Not only is there residual catalyst from growth, but untreated CNTs and arrays are also chemically inert and hydrophobic. It is therefore necessary to enhance the properties of the arrays and make them more suitable for eventual composite fabrication. A brief description of the purpose and procedure for each follows.

#### **3.2.2.1 Amorphous Carbon Deposition**

Due to the low density and vast amount of air in a pristine CNT array, they were not dimensionally stable and thus difficult to process further into composites. Previous research has shown that by depositing amorphous carbon to pristine arrays post-growth, the density and compressive strength can be increased. The deposited carbon forms graphitic layers around individual CNTs instead of depositing disordered, amorphous carbon, therefore increasing CNT diameters and bonding between adjacent tubes [121].

Pristine arrays were carefully cleaned with a razor blade to remove overgrowth from the edges of the quartz. The samples were placed on the sample platform and loaded into the middle of the inner tube, which was loaded into the reactor's outer tube. The main vacuum valve was opened and the system was allowed to pump down until the pressure was below 10 mTorr.

After pumping down, the furnace was heated to 800°C. Upon reaching the set point, C<sub>2</sub>H<sub>2</sub> was flowed at 600 sccm, and the automatic pressure control regulated a set point of 30 Torr. After the desired amount of time, the furnace was turned off, C<sub>2</sub>H<sub>2</sub> gas flow was stopped and the tube was purged with Ar gas for 1 minute. At 700°C, the furnace lid was opened and a fan was directed at the hot zone to allow for more rapid cooling. Once cooled, the furnace tube was refilled with Ar gas to return the system to atmospheric pressure. The samples were removed, weighed, and stored for further processing and characterization.

#### **3.2.2.2 Thermal Oxidation**

Research has shown that carbon produced by CVD from hydrocarbon feedstock is hydrophobic as a result of C-H groups that terminate the surface [35–37]. The outermost walls of CNTs grown using CVD are also prone to being coated in disordered amorphous carbon as well. The

nonpolar nature of this surface combined with the surface roughness of the CNT array creates a highly hydrophobic structure, incapable of being wet by polar solvents like water [100], [102]. To enhance the wetting properties of the as-grown arrays, thermal oxidation and atmospheric plasma treatments were used.

Thermal oxidation simply uses thermal energy to break chemical bonds at specific temperatures. By breaking nonpolar C-H and C-C bonds, polar groups from the surrounding atmosphere can reattach and form a more polar, and thus wettable system.

Pristine arrays were placed on a quartz sample stage and loaded into a muffle furnace set to the desired temperature (550, 575 or 600°C). After oxidizing in air for the required time (10, 20 or 30 minutes), the samples were removed from the furnace and allowed to cool on the bench top. Once cool, the samples were stored for further processing and characterization.

### *3.2.2.3 Atmospheric Pressure Oxygen Plasma Etching*

Plasma treatments rely on the generation of a highly reactive species that is capable of etching the target material. A capacitor is filled with a target-specific gas mixture so that when a strong field (either pulsed direct current or alternating current), is applied, the etchant gas is ionized to form a radical. The radical reacts with the sample surface, locally breaking and reforming covalent bonds. In the case of CNT arrays, nonpolar C-H and C-C bonds are broken and replaced with oxygen-containing polar groups, thus increasing the wettability.

The atmospheric plasma treatments for this thesis were conducted in a custom-fabricated system in Dr. Marian McCord's lab with the assistance of Joshua Nowak. The CNT array was placed on a Plexiglas platform and loaded into the middle of the chamber. Once sealed, the chamber was filled with 1% oxygen in helium for 3 minutes. Then the power supply was turned on and a function generator created a 1.67 kHz frequency AC field. The plasma had a milky-white and purple glow, which is characteristic of the gas mixture. After the desired treatment time, the power supply was turned off and the sample chamber was vented to remove excess ozone. The samples were removed and stored for further processing and characterization.

### *3.2.3 Processing of Copper Salts*

Before salts were processed in aqueous solutions, the proposed dehydration and reduction parameters were tested on each in powdered form to verify the effectiveness.

A small quartz boat was filled to the top with the hydrated salt as it was received from the manufacturer. The boat was placed in an oven, and the temperature was increased to 105°C. After one hour, the oven was set to 185°C and again left for one hour. The sample was allowed to cool in air after dehydration, and immediately after it was loaded into the center of the inner quartz tube for the vacuum furnace. The inner tube and sample were inserted into the outer tube, and the furnace was closed and allowed to pump down until the pressure was below 10 mTorr.

After pumping down, H<sub>2</sub> was flowed into the tube assembly at 500 sccm and the pressure was maintained at 95 Torr. The furnace was quickly heated to 300°C, and allowed to dwell for 30 minutes. When the reduction was complete, the furnace was turned off but H<sub>2</sub> continued to flow until the sample had cooled to room temperature. Once cool, the system was purged and refilled with argon to return it to atmospheric pressure. The powder sample was unloaded and stored for characterization.

#### ***3.2.4 Carbon Nanotube - Copper Composite Fabrication***

Once the arrays had been fully post-treated to achieve a wettable state, they were ready for solution infiltration. Super-saturated solutions of each copper salt in (DI) water were prepared. A heat-safe glass container was placed on a heated stir plate with a magnetic stir bar. Approximately 50 mL of DI water was poured into the glass container. The temperature of the hot plate was maintained to keep the solution just below boiling. Salt crystals were slowly added and allowed to fully dissolve. This process was continued until the almost-boiling solution reached a super-saturated state where no additional salt crystals could be dissolved.

Each array was firmly gripped with a pair of tweezers and the magnetic stir bar was temporarily turned off to prevent sample damage. The array was submerged in the salt solution for 10 seconds, gently tapped off to remove excess liquid, and then quickly weighed. After weighing, the sample was allowed to dry in the fume hood for 24 hours to slowly evaporate excess water. Then, the arrays were placed on a scrap piece of quartz on top of a hot plate with a surface temperature of 100°C to further remove excess moisture. Dehydration of the salts was also completed on the hot plate by simply increasing the temperature to 185°C for 2 hours.

The reduction step was completed inside the tube furnace under vacuum. Dehydrated composites were loaded onto a quartz stage, which was loaded into the center of the inner tube. The inner tube was loaded into the outer tube of the furnace, and the system was allowed to pump down until the base pressure was less than 10 mTorr. While the furnace was heating to 300°C, hydrogen (H<sub>2</sub>) gas was flowed at a rate of 500 sccm while the pressure was maintained at 95 Torr. After 1 hour,

the furnace was turned off and the system was allowed to cool under an H<sub>2</sub> atmosphere. Maintaining the H<sub>2</sub> flow during cooling prevented the oxidation of the newly formed metallic copper.

Once the system returned to room temperature, H<sub>2</sub> flow was stopped, and the tube was refilled with argon (Ar) gas to return the system to atmospheric pressure. The composites were removed from the inner tube and weighed to verify copper content.

### **3.3 Material Characterization**

#### **3.3.1 Chemical Structure Analysis**

The graphitic quality and defect density of the CNT arrays was analyzed using a Renishaw Ramascope with a laser wavelength of 514nm. The laser spot was focused using a Renishaw microscope. Each sample was scanned at least 3 times between 100 - 4000 cm<sup>-1</sup>. A Visual Basic Application (VBA), developed by Murphy Carroll, automatically transposed the gathered data into Microsoft Excel, produced plots of the spectra, identified peaks and calculated average G<sub>I</sub>/D<sub>I</sub> ratios.

Qualitative chemical species information was gathered using Elemental Energy Dispersive X-ray Spectroscopy (EDS) on a Hitachi S3200 Variable Pressure Scanning Electron Microscope (VPSEM) fitted with a 4Pi Isis EDS system. Elemental spectra were gathered over an acquisition time of 100 seconds and accompanying images were taken with a beam voltage of 20kV.

Chemical composition of treated CNT arrays was completed using X-ray photoelectron spectroscopy (XPS) on a SPECS XPS system (SPECS Surface Nano Analysis) using a high-resolution PHOIBIS 150 hemispherical analyzer. Freshly post-treated arrays were transported and stored in non-outgassing Fluoroware containers to prevent surface contamination. Measurements were taken at a base pressure of 10<sup>-10</sup> bar with an Mg K $\alpha$  excitation source (1254 eV). Survey scans were taken from 1200 – 1 eV and high-resolution scans were taken of the O 1s peak at 538 – 528 eV. Energy calibration was established by referencing to the carbon C 1s line at 285 eV binding energy.

#### **3.3.2 Micro-Structural Analysis**

Scanning electron microscopy (SEM) was used to image the CNT surface and array morphology. Samples were mounted to the stage using conductive carbon tape and it was not necessary to sputter coat the samples. For higher resolution a FEI Quanta 3D FEG Dual Beam microscope with both Field Emission and Focused Ion Beam columns was used. The beam

acceleration voltage was 2kV. To prevent beam drift, samples were contacted with a small piece of carbon tape, stretching from the top of the sample to the stub.

Transmission electron microscopy (TEM) images were taken using a Hitachi HF2000 Cold Field Emission TEM with a beam voltage of 200kV. A probe sonicator was used to disperse 0.001g of CNTs in 10 mL of DI water. To achieve a more stable dispersion 0.04 g of Triton X-100 surfactant was added. The mixture was pulse sonicated (1 second on, 0.3 seconds off) in an ice bath for 1 hour. Immediately following sonication, a small amount of the dispersion was deposited on holey carbon mesh, Cu TEM grids and then allowed to dry.

### ***3.3.3 Thermal Properties Analysis***

Thermogravimetric analysis (TGA) was used to analyze the oxidation rate of CNT arrays. Tests were conducted in air on a Perkin Elmer Pyris 1 TGA. The furnace was quickly ramped to the set point temperature (550, 575, or 600°), and then let to dwell for 30 minutes while mass loss was monitored as a function of time.

### ***3.3.4 Mechanical Analysis***

The compressive properties of pristine, CVD post-treated and Cu-CNT nanocomposites were measured using an Instron 5544 mechanical tester operated in compression mode. Platens were custom-designed and fabricated to fit securely in the clamp holders to prevent unwanted instrument compliance. The top platen measured 1.25 inches in diameter, while the bottom measured 2 inches, which allowed for total coverage of all arrays tested. The load rate was set to 2 mm/min, and a 2 kN load cell was used for all samples.

### ***3.3.5 Wetting Properties Analysis***

To measure the static contact angle of pristine and post-treated arrays, a Dataphysics OCA 20 contact angle system was used. Live video taken during the measurement allowed for precise calculation of the contact angle by optical measuring software. Before hydrophobic samples could be tested, the syringe needle was first coated with a fluorinated polymer film to prevent the droplet from adhering. The volume for all droplets used was 4  $\mu$ L, which was dispensed at a rate of 1  $\mu$ L/second. Each sample was measured in 4 different locations, while special care was taken to be sure that the same area was not tested twice to prevent distortion of the results. Angle measurements for the right and left side were averaged for each droplet, and then the measurements were averaged for each sample.

## 4 Controlling the Wetting Behavior of Carbon Nanotube Arrays

### 4.1 Background

The superior mechanical [9–11], thermal [14], [15], and electrical [12], [13], properties make CNTs a highly attractive reinforcing material in a variety of composite applications. In order for one to achieve the synergistic goals of matrix and reinforcement phases working seamlessly together, a strong interface through which energy can easily transfer must be present. The quality of a composite's interface is majorly influenced by the mutual wetting of the two phases; without ample wetting the likelihood for adhesion and bonding between phases is low. This is a significant issue for researchers working with CNT reinforcement due to the chemically inert nature of CNT surfaces [35–37]. Various procedures have been developed to modify the CNT structure to allow for the attachment of surface functional groups [122], but these processes are time and energy consuming, and also diminish the superior physical properties of pristine CNTs.

An additional concern for those working with VA-CNT arrays is the increased hydrophobic nature that is caused by high surface roughness [100],[101],[105]. CNT arrays, with their hierarchical micro and nano-sized features exhibit what is known as the Lotus leaf effect where surface chemistry and morphology combine to create a superhydrophobic, self-cleaning material [106]. Overcoming this hydrophobicity has an added layer of complexity if the delicate, aligned structure of the CNT array is to be preserved. Liquid-based chemical oxidation creates significant capillary forces in between adjacent CNTs within the array. Upon drying, the liquid surface tension will drastically disrupt alignment and induce CNT bundling – both of which are bad for eventual composite fabrication.

Gas phase treatments like UV/ozone, thermal oxidation, laser irradiation and atmospheric plasma have been applied in order to create a wettable structure, but also prevent macroscopic damage to the array structure. Each of these methods have demonstrated varied success, but evaluation of the methods in terms of the extent of their detrimental effects on CNT structure and properties is limited. In order for any potential functionalization methods to be not only viable, but also practical considerations of the scalability, time, energy and overall damage to the CNT properties must be critically examined.

## 4.2 Experimental Procedure

Vertically aligned CNT arrays were grown using LP-CVD and a floating catalyst, iron(II) chloride. One gram of catalyst powder was placed in a quartz boat and inserted into the inner quartz tube. 25 x 25mm and 10 x 10mm quartz substrates were burned and etched in dilute HF before being placed on a quartz sample platform which was also inserted into the inner tube. The inner tube was loaded into the outer tube, and the system was allowed to pump down for at least two hours until the pressure was below 10 mTorr.

Growth was commenced by heating the furnace to 760°C. Upon reaching the growth temperature, 600 sccm of acetylene, 133 sccm of chlorine in argon and 267 sccm of pure argon gas were flowed through the system while the pressure was digitally controlled and maintained at 5 Torr. After 20 minutes the growth was stopped by purging the tube with pure argon and cooling the furnace to room temperature. After growth, the arrays were cleaned, weighed, and measured. Baseline Raman spectra and static contact angles were taken on all samples before undergoing wettability treatments. The arrays grew to approximately 1.5 mm in 20 minutes.

The two treatments studied in this work were thermal oxidation and atmospheric plasma. For thermal treatment, the as-made array was placed in a quartz boat and loaded into a muffle furnace set to the desired treatment temperature. The temperatures studied were 550, 575 and 600°C. After 10 minutes, the CNT array was removed from the furnace and allowed to cool to room temperature on the bench top. Then, Raman spectra and contact angle measurements were taken again, taking special care that a new area of the array was tested each time to ensure accuracy. The 10-minute oxidation and Raman/contact angle measurement steps were repeated two more times to total 30 minutes of treatment time for each temperature set point.

For atmospheric plasma treatments, the CNT array was placed on a Plexiglas platform and placed in the plasma chamber. Once sealed, the chamber was filled with 1% oxygen in helium gas for three minutes. A power supply and AC function generator created a 1.67 kHz oscillating field which induced a milky-white plasma throughout the whole chamber. After the desired amount of time (1, 5 or 10 seconds), the power supply was turned off, and the plasma chamber was vented to remove any remaining ozone gas. Immediately following the plasma treatment the arrays were characterized with Raman spectroscopy and static contact angle measurement.

In CNT research, it is common to observe property variability, not only between growth runs, but also even within a single sample. Because of this, extensive efforts were made to reduce sample and characterization variability. To directly compare the effects of the thermal and plasma treatments

on CNT arrays, all of the samples used were synthesized in the same growth run, and the same sample was used for the entire extent of one particular treatment. For example, Array X was thermally oxidized at 550°C for 10 minutes, characterized, and then placed back in the furnace for an additional 10 minutes, when it would again be taken out and characterized. This continued for a total of 30 minutes for each thermally oxidized sample, and up to 30 seconds for the plasma treatments.

Baseline characterization of all arrays was conducted after growth to verify sample-to-sample consistency. This included measurement of array height and weight, SEM imaging, as well as Raman and static contact angle (SCA) measurement. Because variability can even be found within a single array, Raman measurements were taken from at least four different areas for most experiments, and ten locations for the time study. A Visual Basic Application (VBA) script was developed in house to assist with data collection, presentation and analysis. This allowed for rapid identification of the G and D Raman peaks and subsequent calculation of each  $G_1/D_1$  ratio and sample averages. Additionally, multiple SCA measurements were taken for each sample at each stage of treatment. Special care was taken for SCA measurement to avoid placing droplets in areas that had already been tested.

## **4.3 Results and Discussion**

### ***4.3.1 Achieving Array Wettability***

Complete wetting of the CNT arrays was successfully achieved using both thermal oxidation and atmospheric plasma treatments. Though not fully wettable, the array treated at 500°C exhibited a steady decrease in contact angle for each subsequent treatment, starting at 146.2° for as-grown and falling to 137.9°, a 5.7% change after three-10 minute thermal treatments to total 30 minutes. At 575°C, complete wetting was achieved after 30 minutes with the contact angle decreasing from an initial value of 146.3° to 137.4° after 20 minutes. The most aggressive treatment of 600°C yielded a wettable array after only 10 minutes. A summary of the average contact angles measured for each temperature and duration is shown in Figure 4.1. The contact angle of CNT arrays treated with atmospheric oxygen plasma decreased from an initial value of 138.2° to 128.1° after only one second of treatment. Five seconds of plasma was adequate to create a fully wettable array. Figure 4.2 shows images of water droplets taken during SCA measurement of each sample. The decreasing contact angle is visually apparent for increasing temperatures as well as increasing treatment duration.

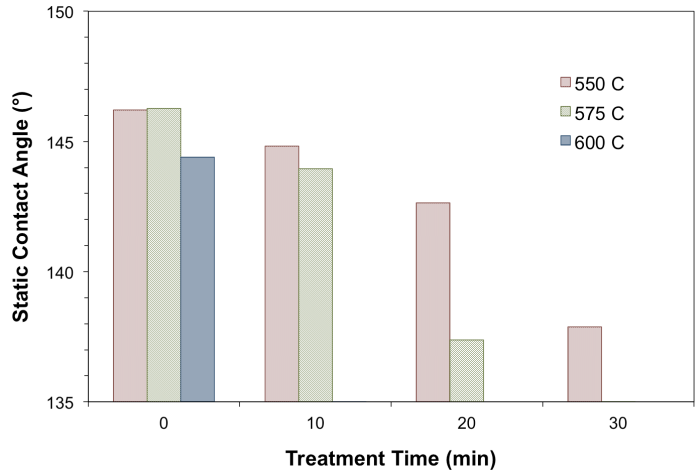


**Figure 4.1** The change in static contact angle as a function of thermal oxidation treatment. Lower contact angles are measured for samples treated at higher temperatures and longer durations. Absence of a data point for a particular time and temperature indicates that wetting occurred.

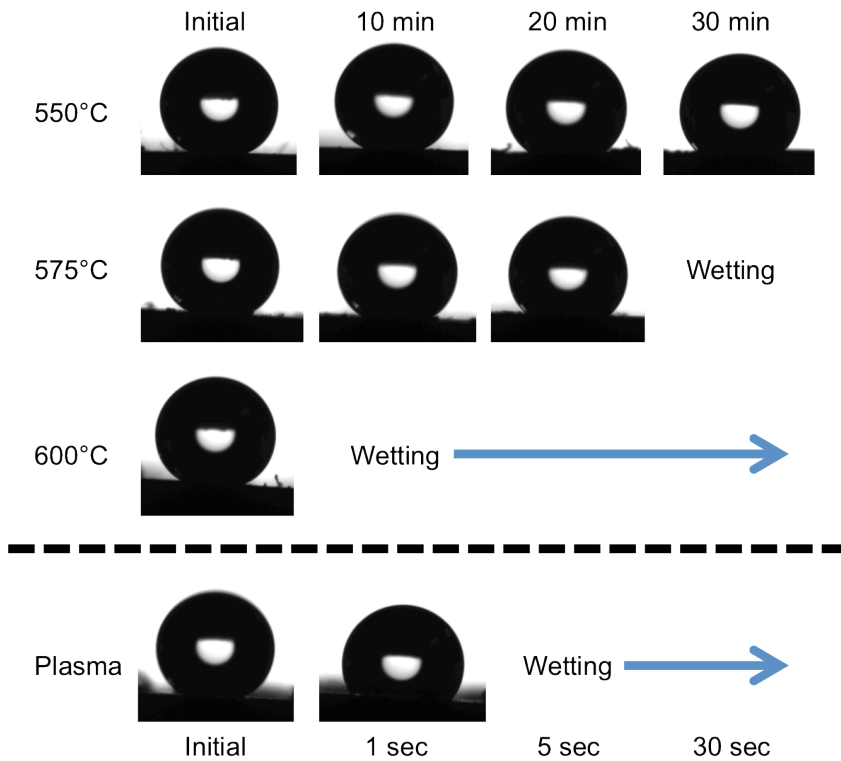


**Figure 4.2** Static contact angles were measured for thermally oxidized and plasma treated CNT arrays. Wetting was achieved at temperatures of 575°C and 600°C, but not at 550°C. Plasma treating CNTs for 5 seconds yielded wettable arrays.

To explain the mechanism by which wetting was achieved, XPS and EDS were used to probe the changes in chemical structure before and after the treatments that successfully created wettable arrays (575°C for 30 minutes, 600°C for 10 minutes, and plasma for 5 seconds). Extended XPS scans of each pristine array were taken to ensure uniformity across all samples. For all three samples, the only measurable signal found was the C 1s peak at 284.5 eV. After both thermal treatments, the extended scan detected the presence of oxygen by the O 1s peak at ~533 eV in addition to the C 1s peak. The before and after XPS spectra for each sample are overlaid in Figure 4.3. High-resolution analysis of the O 1s peaks for the thermally treated samples are shown in Figure 4.4. The peaks at 531 and 536.5 eV correspond to the presence of C=O and surface adsorbed CO, respectively. Signal from adsorbed CO is more prominent on the sample treated at 575°C for 30 minutes. It should be noted that the spectra for all samples after treatment showed the presence of fluorine, which is a fairly common contaminant in a surface sensitive technique like XPS.

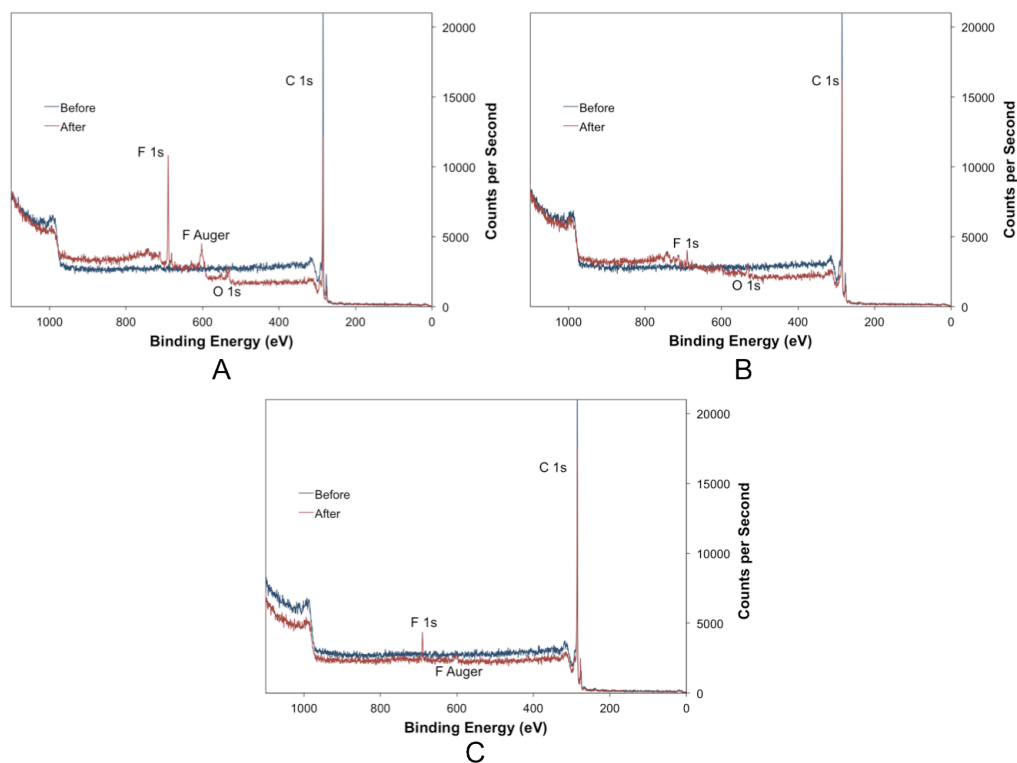


**Figure 4.3** XPS was used to detect chemical changes in CNT arrays before and after treatment: A) 575°C for 30 minutes; B) 600°C for 10 minutes and; C) atmospheric oxygen plasma for 5 seconds. Oxygen was detected for both thermally treated samples, but not for the plasma treated sample.

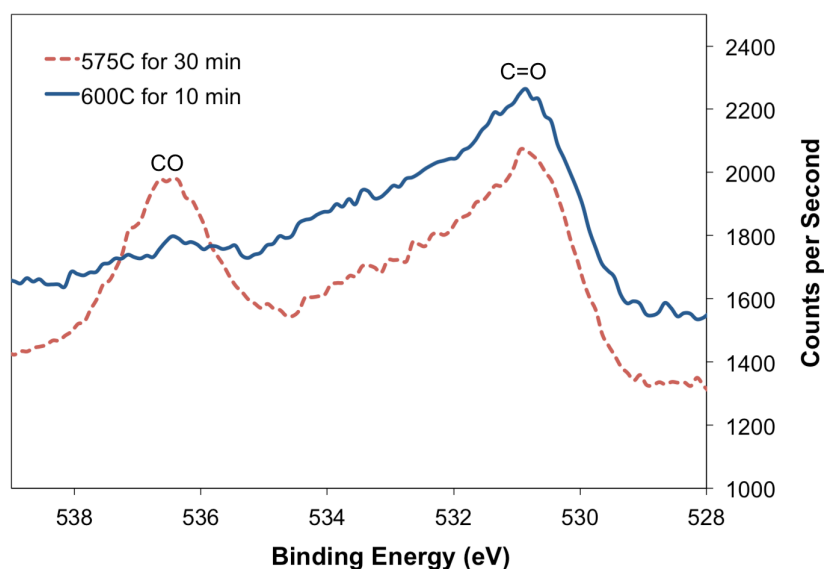


**Figure 4.4** High-resolution XPS scans of the O 1s peaks for the thermally treated samples show the presence of C=O (531 eV) and surface adsorbed CO (536.5 eV) on the CNT arrays.

Though wettable, the plasma treated sample did not exhibit a O 1s peak like the thermally oxidized samples did, so further characterization was required. EDS analysis, shown in Figure 4.5, of a plasma treated array confirmed the increased presence of oxygen compared to the pristine array. There are a few possible explanations for the discrepancy between characterization methods. First, it was later found that the wettability of CNT arrays treated with plasma was not a permanent effect. Other studies have also demonstrated reversible wetting of CNT arrays [113], [116], [119]. First, oxygen-containing functional groups were applied using a gas phase functionalization technique, and then the hydrophobicity was recovered using either CO<sub>2</sub> laser irradiation or vacuum pyrolysis. In the case of the latter, the treatment involved heating the array to 250°C in moderate vacuum (2.5 Torr), for at least 3 hours. This resulted in a reduction in the concentration of polar groups on the CNT surface, and restoration of hydrophobicity of the CNT arrays.

XPS analysis requires at least 8 hours of pumping time for the system to reach ultra-high vacuum, around 10<sup>-9</sup> Torr. It is therefore within reason to expect that functional groups would be removed in these conditions. EDS characterization of the plasma treated arrays was conducted in a variable pressure SEM, which required virtually no pumping time before spectrum acquisition. Additionally, the beam-sample interaction volume from which signal is generated in SEM/EDS is

much larger than that of XPS, which is a highly surface sensitive technique. Given the low density of the CNT arrays and the low concentration of oxygen functional groups, collecting signal from a larger interaction volume made it possible to detect the presence of oxygen in the plasma treated samples. Further characterization of the CNT and array structure using Raman and SEM supported these findings.

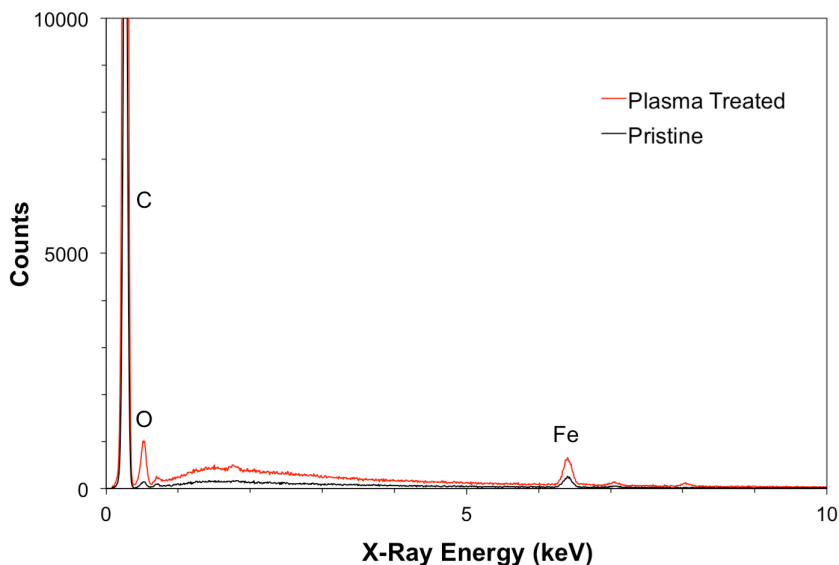


**Figure 4.5** EDS spectra of vertically aligned CNT array after plasma treatment shows an increased concentration of oxygen compared to a pristine sample.

### ***4.3.2 Effect of Treatments on Carbon Nanotube and Array Structure***

To visualize the affect of the wettability treatments on the CNT and vertically aligned array structures, images were taken with SEM before and after treatment. In Figure 4.6, images A and B show the normal morphology of the top of an array. The surface is visually consistent and covered with a randomly coiled network of CNT tips. After treatment the most drastic physical damage is seen on the array treated at 575°C for 30 minutes. The low magnification inset of image C shows the self-assembled, grain-like structure while the high-resolution image (D), shows significant structural damage to individual CNTs. There is less visible damage to the arrays treated at 600°C for 10 minutes (E,F), and plasma (G,H), though plasma treated CNTs are slightly more broken and tightly coiled.

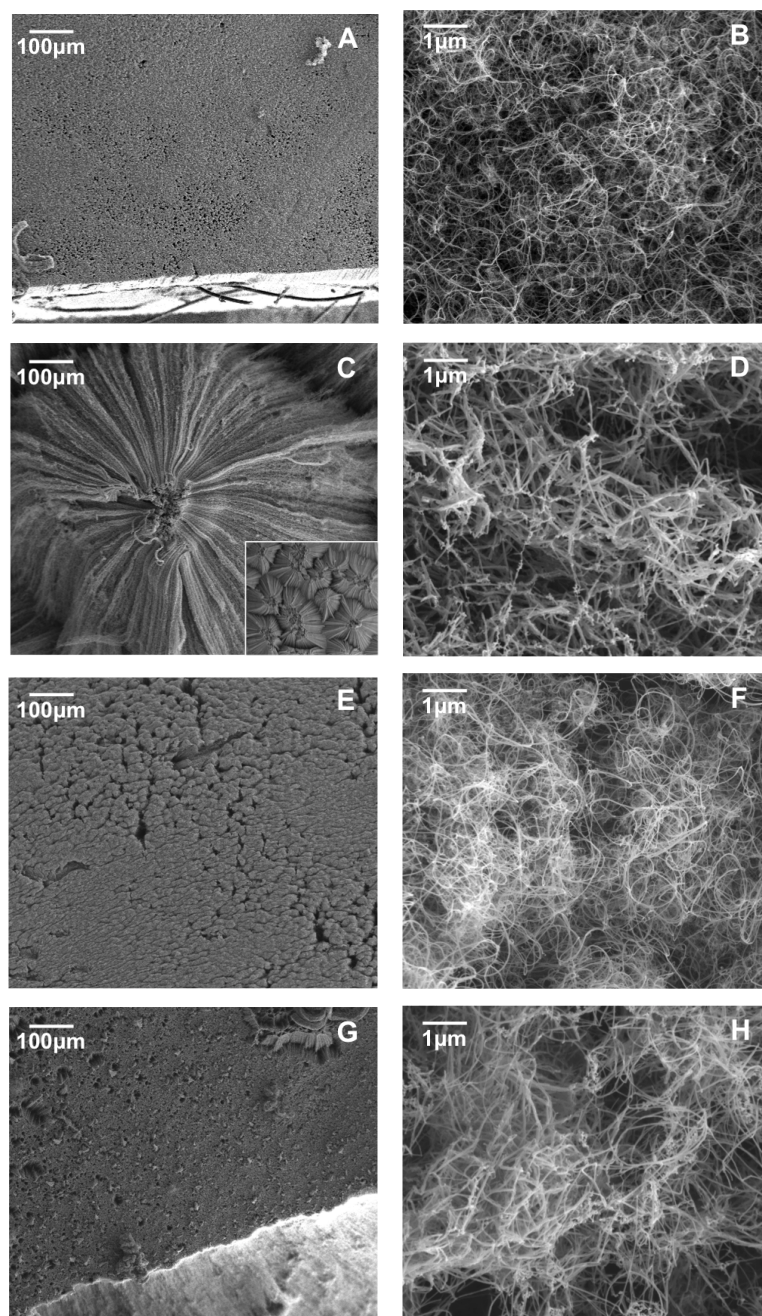


**Figure 4.6** Low and high magnification (left and right, respectively), SEM images of the top surface of CNT arrays: A,B) untreated; C,D) 575°C for 30 minutes; E,F) 600°C for 10 minutes and; G,H) atmospheric oxygen plasma for 5 seconds.

Raman analysis was used to probe the extent of defects incurred as a result of thermal and plasma treatments. Of primary interest are the carbon material disorder induced D-band ( $1350\text{ cm}^{-1}$ ), and the G-band ( $1582\text{ cm}^{-1}$ ), which arises from in-plane vibrations of graphite. It is common to compare the ratio of the intensities of these peaks ( $G_1/D_1$ ), among samples to determine relative defect content even the extent of chemical functionalization [123]. Generally, a lower value for the  $G_1/D_1$  ratio relates to an increase in defect density or disorder, and therefore increased oxidation. Broadening of these bands relates to the functionalization of CNT sidewalls or tips that cause the conversion of  $sp^2$  graphitic bonds to  $sp^3$  amorphous carbon bonds. As defects provide sites for functional groups to bond, it follows that samples with lower  $G_1/D_1$  will be more hydrophilic. Increased defects will also degrade the mechanical, thermal and electrical properties of the CNTs however, so the extent of this damage should be minimized for those seeking matrix property enhancement in composite applications.

The Raman spectra for all thermally treated samples were compared to determine the extent of damage to the CNT bonding structure as a function of temperature and duration (shown in Figure 4.7). The average  $G_1/D_1$  ratio for pristine arrays was 1.75. This value generally decreased for increasing temperatures and treatment duration, though the rate of change appears to level out after 20 minutes for all three cases. The largest change in average  $G_1/D_1$  ratio is seen after 10 minutes at  $600^\circ\text{C}$ , decreasing from 1.7 to 1.38.

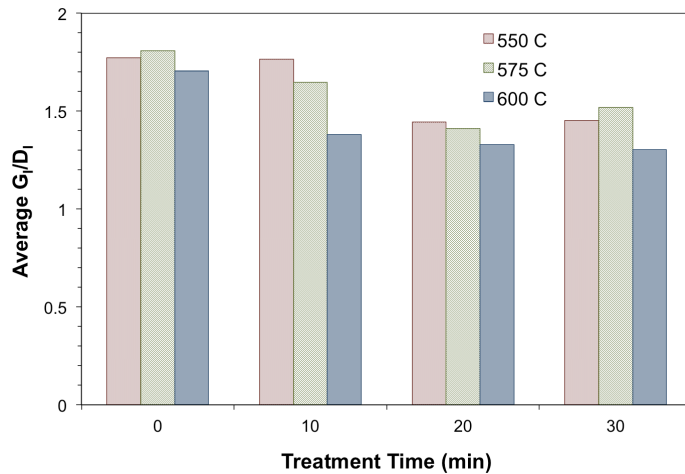


**Figure 4.7** Raman spectra were taken for all thermally oxidized samples to analyze the changes in CNT structure. The average  $G_1/D_1$  ratio generally decreases as a function of temperature and treatment time.

In a CNT array synthesized via thermal CVD, there are two sources of carbon available for oxidation –  $sp^3$  amorphous carbon, and  $sp^2$  graphitic carbon. The activation energy required for the carbon-oxygen oxidation reaction to occur is 34.4 and 69.7 kcal/mol for amorphous carbon and MWNTs, respectively. This means that the oxidation of amorphous carbon will occur at lower temperatures.

The rate of oxidation is an additional factor that should be considered for both carbon systems. Figure 4.8 shows the level of  $CO_2$  evolution (a by-product of carbon oxidation) as a function of temperature for a variety of carbon compounds. By comparing the values of  $CO_2$  evolution at 550, 575 and 600°C for MWNTs and amorphous carbon, the oxidation mechanism and its affect on the  $G_I/D_I$  ratio of thermally treated arrays can be understood. In the case of MWNTs, the level of  $CO_2$  evolution is virtually equal (~1500 ppm) for all three temperatures. Amorphous carbon however, has a very steep slope in the studied range of temperatures. This means that at 550°C, oxidation will take place much more slowly than at 600°C. The difference in  $CO_2$  evolution is significantly large, increasing from ~500 ppm to ~1650 ppm.

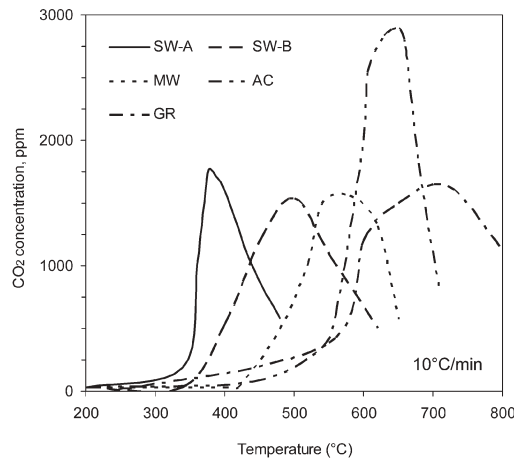


**Figure 4.8** The kinetics of the oxidation of several carbon compounds were studied by monitoring the  $CO_2$  evolution profile as a function of temperature (taken from Brukh et al. [124]).

Knowing this, the rapid decrease in  $G_I/D_I$  ratio after treatment at 600°C for 10 minutes can be attributed to the oxidation of  $sp^3$  hybridized amorphous carbon. Because the rate of reaction is so much faster at this temperature, the excess amorphous carbon left over from CVD synthesis is quickly

reacted, and further reduction in the  $G_I/D_I$  ratio is not seen. Twenty minutes of thermal treatment at 550 and 575°C is long enough to remove amorphous carbon in those samples, as evidenced by the stability of the  $G_I/D_I$  ratio between 20 and 30 minutes.

This is not to say that all oxidation is complete. Although more stable than amorphous carbon, the walls of MWNTs are simultaneously being oxidized, which results in the conversion of  $sp^2$  bonds to  $sp^3$  bonds – and thus the formation of new amorphous carbon. Newly formed amorphous carbon is subsequently oxidized at a rate determined by the temperature of the system. The  $G_I/D_I$  ratio does not continue to drop despite the oxidation of MWNT walls. MWNTs can have in excess of 40 walls, which would take a significant amount of time to oxidize at temperatures less than 750°C. Even if one wall is consumed by oxidation, there are 39 more underneath it before the graphitic nature of the sample is lost.

The consumption of these walls and amorphous carbon does lead to mass loss. Analysis with TGA provided a direct comparison of the physical changes in thermally treated arrays. The system was quickly ramped to the temperature set point (550, 575 or 600°C), and then let to dwell for 30 minutes. The time required for the ramp was 5 minutes. As can be seen in Figure 4.9, total mass loss after 30 minutes was greatest for the 600°C set point. It is interesting to compare the mass loss at the wettable states of 575°C for 30 minutes and 600°C for 10 minutes. The plot shows that the mass loss for the former treatment is over 5% while 600° for 10 minutes only results in a loss of ~2%.

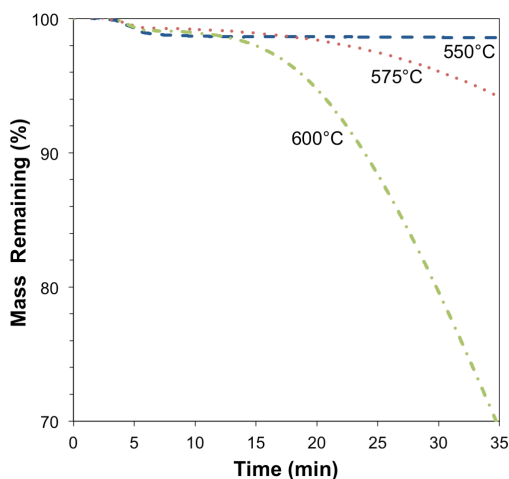


**Figure 4.9** Thermogravimetric analysis (TGA) was used to compare mass loss as a function of treatment temperature (550, 575 and 600°C), and time.

Raman analysis of arrays treated with plasma showed much less dramatic changes in the  $G_I/D_I$  ratio compared to thermally treated samples, as shown in Figure 4.10. Previous research in the plasma functionalization of vertically aligned CNT arrays found that the ratio could actually be increased due to the plasma interaction with defect-ridden CNT tips, effectively reducing the defect density [116]. In fact, there are competing reactions due to the simultaneous conversion of  $sp^2$  to  $sp^3$  carbon as a result of functionalization [123]. A virtually unchanging  $G_I/D_I$  ratio signifies a consistent defect density, regardless of plasma treatment time.

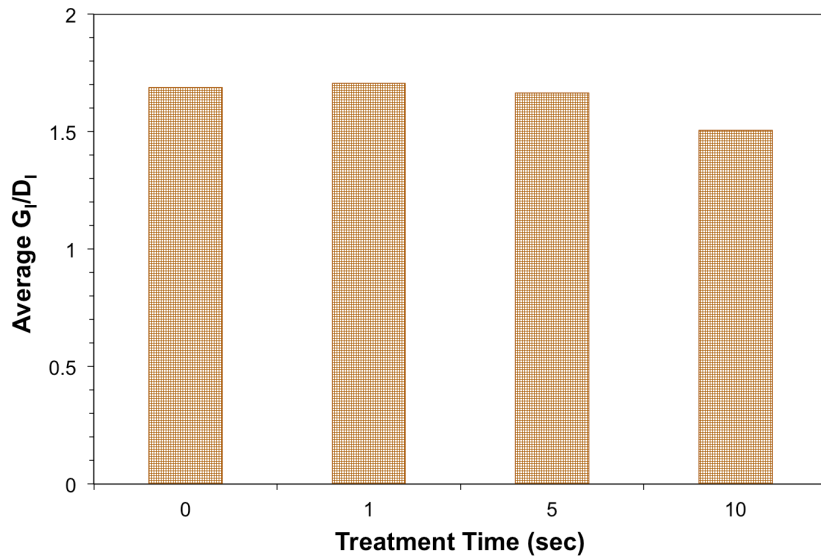


**Figure 4.10** Raman spectra were taken for all plasma treated samples to determine the effect of treatment time on CNT structure. A virtually constant  $G_I/D_I$  ratio signifies no change in defect density.

Figure 4.11 shows the average  $G_I/D_I$  ratios of each treatment that successfully created wettable arrays. Because the motivation of this thesis is the fabrication Cu-CNT composites with enhanced physical properties, it is beneficial to choose a functionalization treatment that creates both an easily wettable reinforcement, but which has also maintained its superior properties. It is evident from the Raman analysis of the wettable samples that arrays treated with atmospheric plasma are virtually unchanged in terms of defect density when compared to pristine arrays. An additional

benefit is how quickly the treatment can be completed. In total, the preparation for and the plasma treatment itself takes 5 minutes.

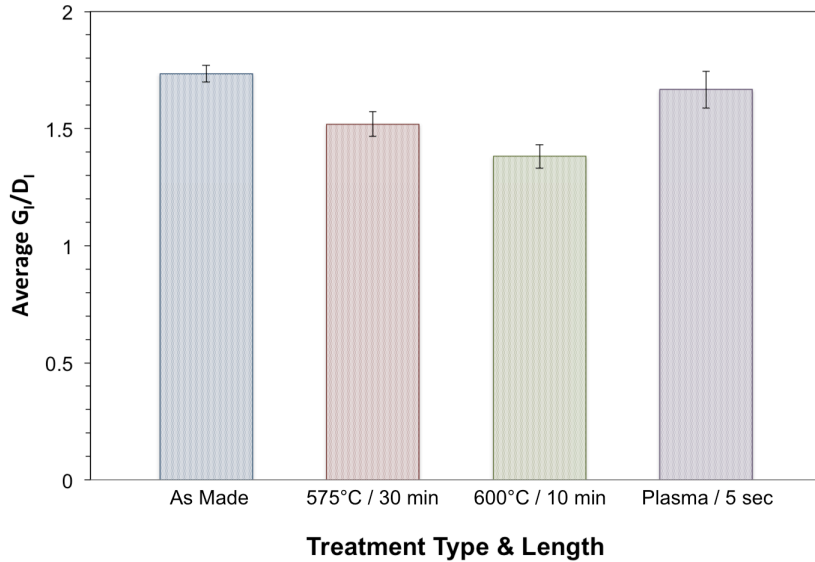


**Figure 4.11** Raman spectra were collected to compare average  $G_1/D_1$  ratios for all treatments that successfully yielded a wettable CNT array.

### 4.3.3 *Effect of Time on Array Wetting Properties*

As previously mentioned, it was discovered that the hydrophilicity achieved via plasma treatment were not permanent. A study was conducted to determine the amount of time before hydrophobicity was restored to the arrays. As a basis for comparison, a thermally treated sample was tested simultaneously.

Following the same procedures as before, the baseline contact angles and Raman spectra were taken for both samples before being treated. One array was treated with oxygen plasma for 1 minute, while the other was thermally oxidized at 575°C for 30 minutes. Immediately following treatment, 10 Raman spectra were collected from each sample in different areas to ensure consistency. At designated time intervals each of the arrays were checked for wettability, and 10 additional Raman spectra were collected. After 72 hours, hydrophobicity was restored to the plasma

treated sample, with an average contact angle of  $143^\circ$ , only  $3^\circ$  lower than its baseline value, as shown in Figure 4.12. Hydrophobicity was not restored to the thermally oxidized sample.



**Figure 4.12** CNT array wettability achieved via plasma treatment will last for 72 hours if left exposed to atmosphere. The measured contact angle after 72 hours was  $143^\circ$ , only  $3^\circ$  lower than the pristine array before treatment.

Figures 4.13 shows the results from Raman characterization during the time study. The horizontal, grey dotted line signifies the average  $G_1/D_1$  ratio of the sample before plasma treatment (2.06). Upon treatment the  $G_1/D_1$  ratio decreases slightly to an average value of 1.85, but then increases back up to 1.97 after 72 hours when the sample becomes hydrophobic again. The observed trend line is a linear fit for all of the data points taken in this study. The positive slope verifies the general increase of  $G_1/D_1$  ratio as a function of time.

The same was not true for the thermally oxidized array. Figure 4.14 shows the drastic decrease in  $G_1/D_1$  ratio from an average of 1.95 for the untreated array (horizontal, grey dotted line), to 1.39 after 30 minutes of thermal oxidation at  $575^\circ\text{C}$ . The fitted trend line of the data does not show any change in the  $G_1/D_1$  ratios as a function of time, indicating that thermal oxidation resulted in only permanent damage to the CNT array.

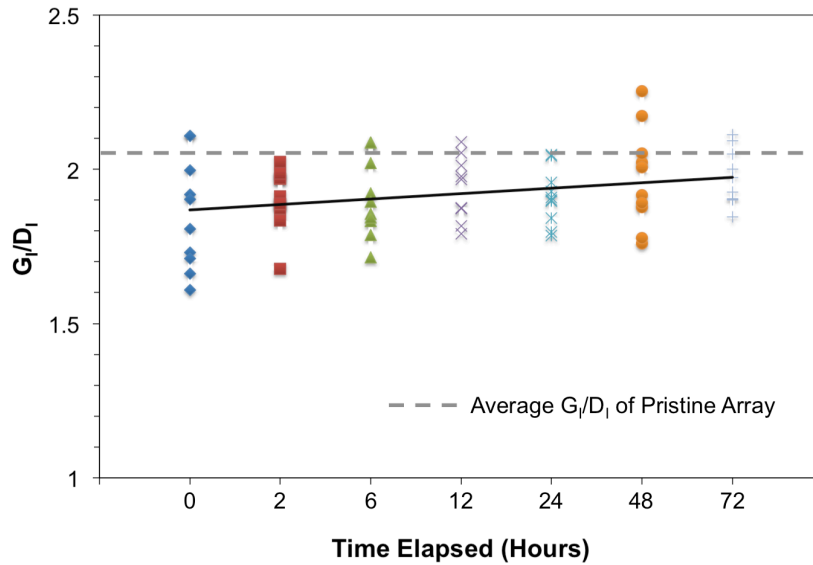


**Figure 4.13** Raman spectra taken before plasma treatment (horizontal grey line), are compared to spectra taken after treatment as a function of time. The  $G_1/D_1$  ratios increase linearly over 72 hours, when hydrophobicity was restored to the array.

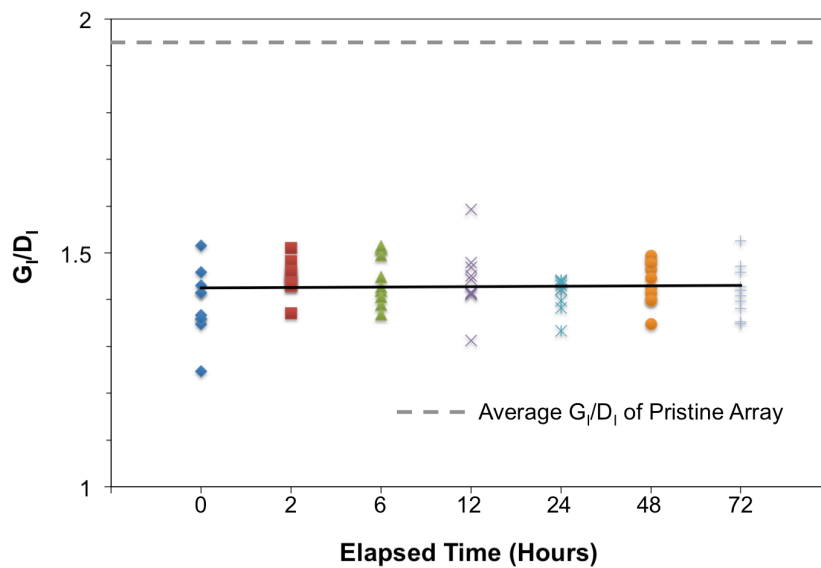


**Figure 4.14** Raman spectra taken before thermal oxidation treatment (horizontal grey line), are compared to spectra taken after treatment as a function of time. The  $G_1/D_1$  ratios remain unchanging after 72 hours of testing.

Other studies on controlling the wettability of CNT arrays have shown recovery of hydrophobicity after plasma functionalization [116]. Treatment with laser irradiation caused rapid, localized heating of the CNTs, and vaporized the attached functional groups. Raman analysis of the irradiated arrays showed a narrowing of bands, which they correlated to the removal of functional groups, but no significant change in the  $G_1/D_1$  ratio. This indicated that the plasma treatment invoked permanent defects in the CNTs, which was not recoverable.

In the case of this research however, the changes to the array are not permanent and can be reversed as easily as letting the sample sit out on the bench top for a few days. Additionally, as evidenced by the XPS results from Section 4.3.1, the recovery process could be sped up through application of vacuum or heating. Most importantly, these results show that a wettable array can be quickly prepared for subsequent composite fabrication without sacrificing the pristine CNT structure.

#### **4.4 Conclusions**

The ability to control the wetting of vertically aligned CNT arrays was demonstrated through thermal oxidation and atmospheric pressure, oxygen plasma treatments. In the former method, the static contact angle of pristine arrays was decreased by increasing temperature and treatment duration, where full wetting was achieved at 575°C for 30 minutes and 600°C for 10 minutes. Atmospheric pressure plasma treatments of 5 seconds also yielded wettable arrays. In both cases, the mechanism of wetting was determined to be the attachment of polar, oxygen-containing functional groups to the surfaces of CNTs. Raman and SEM characterization of wettable arrays showed that thermal oxidation caused significant damage to the array structure as well as permanent defects to the CNT walls. The array wettability achieved by plasma treatments however, was found to be temporary. After 72 hours in atmosphere, wettable arrays returned to their original hydrophobic state with little difference in measured contact angle compared to measurements taken before plasma treatment. Analysis of Raman spectra revealed a small decrease in the  $G_1/D_1$  ratio immediately following plasma treatment, but it was also found to recover over time, signifying a lack in permanent damage to the CNT bonding structure. Atmospheric plasma treatments were therefore established as a viable method for the rapid functionalization of CNT arrays to improve reactivity and wetting, without sacrificing their superior physical properties.

## **5 Method for Fabrication of High Mass Fraction, Aligned Carbon Nanotube - Copper Composites**

### **5.1 Background**

The power electronics of today, with their ever-increasing current density and heat production, have surpassed the heat dissipation capabilities of traditional thermal management materials like elastomers, greases, ceramics and metal alloys. It is crucial that new technologies be developed for the further acceleration and miniaturization of power electronics to continue.

The reliability of circuits is dependent on surrounding operating temperatures. It has been shown that by decreasing the operating temperature of electronic circuits by 10-15°C, the lifespan of the device can be doubled [125]. This is especially important in the field of solid-state lighting as difficulty with thermal management is a leading constraint to widespread consumer adoption. Light emitting diodes (LEDs) are considered to be a promising alternative to energy-consuming incandescent light bulbs. High operating temperatures and overheating hamper LED performance, however, as rapid degradation of light output is accompanied by increased temperature [126]. Many of the failure modes of white LEDs, such as contact bonding degradation and thermal mismatch, are linked directly to the heat dissipation ability of the device and its electronic packaging. Due to this fact, leading researchers in the field have identified thermal management as the most important aspect for device performance and reliability improvement [127]. Reducing operating temperatures will not only extend the life of the device, but also allow it to work more efficiently.

Carbon materials such as diamond and graphite are known to have exceedingly high thermal conductivities due to the uninhibited lattice vibrations used for phonon conduction. These materials, however, are also very expensive and difficult to work with in a commercial setting [35], [128]. CNTs have recently emerged as a highly thermally conductive material. Theoretical and measured thermal conductivities for MWNTs are 6000 W/m-K [15] and 3000 W/m-K [129] respectively. The reason for high conductivity is due to the ballistic transport of phonons along the axis of the CNT structure. The more regular and defect free the CNT, the less opportunity there is for phonon scattering into the bulk material, which is present as heat [130].

CNT reinforced composite materials provide a potential solution to the rapidly evolving thermal and mechanical issues that plague today's electronics. Their high thermal conductivity matched with their superior mechanical and electrical properties match the heat dissipation needs of

power electronics while also providing mechanical enhancement and density reduction. As a result, there is considerable interest in developing CNT-based thermal management materials [131–136].

CNTs have been used widely to improve the conductivity of non-conducting materials like polymers and ceramics, but because of high interfacial resistance between phases, phonon conduction is poor and conductivity enhancement of the resulting composite is minimal. To decrease the contact electrical resistance of these materials, many researchers have fabricated CNT-reinforced copper composites, with varying success in improving thermal conductivity beyond that of pure copper (See Section 2.3.2). These fabrication routes tend to be experimentally complex and time-consuming, but more importantly, the CNTs are randomly aligned, poorly dispersed, short ( $< 10\mu\text{m}$ ), and only found in small volume fractions. Among these methods, however, Molecular Level Mixing (MLM) shows promise as a viable processing route for certain composite applications.

The MLM process was developed as a method for the deposition of thin metal films or nanoparticles to the surfaces of CNTs [54]. CNT powders are first functionalized for many hours in a bath of concentrated acid. This allows for chemical oxidation of the CNT walls and the attachment of functional groups. The groups serve two purposes in the MLM method. First, the charge interactions aid in overcoming the van der Waals forces that usually cause CNTs to agglomerate. Also, upon the addition of a copper salt to the CNT dispersion, the negatively charged functional groups provide sites for the positively charged  $\text{Cu}^{2+}$  cations to associate, thus encouraging homogenous dispersion of CNTs and Cu. In effect, this “locks” the ions in place at a molecular level. The mixture is then dried, and then calcinated or oxidized to form a powdery mixture of CNTs and  $\text{CuO}$ . Finally, hydrogen reduction converts  $\text{CuO}$  to metallic Cu. Though improvements in CNT dispersion and composite homogeneity have been demonstrated, the current MLM method still does not solve all issues.

To address these issues, a simple and novel processing route has been developed that allows for the fabrication of Cu composites reinforced with high mass fraction, 2 mm long, dispersed, and aligned CNTs. The process bears similarities to the Molecular Level Mixing method, (discussed in detail in Section 2.3.2.3), with three key differences: 1) the CNT precursor, 2) gas phase functionalization, and 3) super-saturated copper salt solutions. First, instead of using CNT powders as the reinforcement precursor, 2 mm long vertically aligned CNT arrays are grown in-house and used. Arrays obviously make the goal of CNT alignment straightforward, but maintaining the structure throughout processing can be challenging. Measures must be taken to ensure the dimensional stability of the array during processing, so the affect of amorphous carbon deposition is investigated. Additionally, wet-chemistry processes will generally destroy the array structure and CNT alignment

due to liquid surface tension and capillary forces. The second difference involves the replacement of acid functionalization with atmospheric oxygen plasma etching. This process serves as the method by which CNT arrays are made wettable, but also to provide sites for  $\text{Cu}^{2+}$  cation association. Finally, using super-saturated salt solutions instead of low solute concentrations maximizes the copper content in this processing method. Copper salts were selected on a basis of their solubility in water, and the temperature of the solution is increased near boiling to maximize the amount of dissolved salt. This chapter discusses the details of this modified MLM processing route and evaluates the physical and chemical properties of the resulting composites.

## 5.2 Experimental Procedure

Vertically aligned carbon nanotube arrays (VACNTs) were grown using chlorine mediated low-pressure chemical vapor deposition (CM-LPCVD). They were grown on 13 x 13 x 1 mm or 25 x 25 x 1 mm quartz substrates, which were first burned to remove residual oils and then etched in a dilute HF bath. Before loading into the furnace, the weight of each individual substrate was measured and recorded. One gram of iron chloride ( $\text{FeCl}_2$ ) catalyst powder was loaded into a quartz boat, and placed underneath the platform holding the samples. The tube was sealed and allowed to pump down for two hours until the pressure fell below 10mTorr.

After pumping down, the heating program was started. When the furnace reached 760°C, acetylene, argon + chlorine and pure argon gases were flowed at 600 sccm and 133 and 267 sccm respectively. The pressure was digitally maintained at 3 Torr for the duration of the growth. After 20 minutes, the reactor was purged with pure argon, and the furnace was cooled to room temperature. Once the samples were removed, they were carefully cleaned, weighed again, and stored for further processing and characterization.

Amorphous carbon deposition was the first post-treatment in a succession of two that was used to prepare the as-grown arrays for composite fabrication. This treatment provides increased structural integrity to the low-density CNT arrays, but too much carbon deposition can lead to degradation of composite properties. To determine the optimal length of deposition, multiple samples were made with different lengths of CVD treatments (5, 30 and 60 minutes), and compared against an untreated control array. To conduct the post-treatment, array samples were again loaded into the CVD furnace and pumped down to low pressure. Then the reactor was heated to 800°C and acetylene gas was flowed at 600 sccm. The pressure was digitally controlled to maintain 30 Torr during the course

of the experiment. After the designated time the system was purged with argon gas and cooled to room temperature. Once cool, the samples were retrieved and weighed to record the mass added.

Following amorphous carbon deposition, the arrays were still hydrophobic and therefore an additional post treatment was needed to make them wettable for composite fabrication. Based on results from Chapter 4, the arrays were treated with atmospheric plasma to increase surface reactivity without damaging the bonding structure or properties of the CNT arrays. The treatment was conducted for 60 seconds with 1% oxygen at 1.37 kHz frequency. The combination of these post-treatments yielded arrays which were not only hydrophilic, but also dimensionally stable during composite fabrication.

To fabricate the composites, a super-saturated solution of copper salt (sulfate, nitrate or chloride) and DI water was made in a glass jar with a lid. The solution was placed on a magnetic stirrer/hotplate set to 225°C. Once the solution neared boiling, the post-treated arrays were fully submerged in the salt solution for 20 seconds, then quickly removed and weighed to record the amount of solution added. The arrays were then placed on top of another hot plate, and allowed to dry at 50°C for 24 hours. Before removing the samples from the hot plate, the temperature was increased to 100°C for 30 minutes. The dried composites were then placed on a quartz sample platform, loaded into the CVD furnace, and pumped down for two hours. To begin the dehydration and reduction processes, the temperature was increased to 185°C for 30 minutes, and then increased to 300°C. During the final ramp, hydrogen gas was flowed over the samples at 500 sccm and then pressure was set to 95 Torr. After 30 more minutes, the furnace was turned off and allowed to cool to room temperature. To prevent oxidation, the samples remained in a hydrogen atmosphere until cool. Then, the samples were removed from the furnace, weighed and stored for further characterization.

### **5.3 Results and Discussion**

There are two mechanisms by which stability is achieved in composites fabricated via the modified MLM processing route. First, the density of the array can be increased using reinforcement from amorphous carbon deposition. This treatment has been shown to increase the compression strength of CNT arrays, even providing strain recovery and foam-like properties [121]. Additionally, the benefit of using a super-saturated copper solution instead of a less saturated one is two-fold. Not only will it ensure maximum copper content in the resulting composite, but also the extensive

reinforcing network that forms upon crystallization of the salt solution during cooling provides structural stability to the otherwise fragile CNT array.

To demonstrate these effects, pristine and 30 minute CVD post-treated arrays were plasma treated to make them fully wettable, and then dipped in pure DI water for 20 seconds. Figure 5.1 shows images taken before the dip and the resulting morphology changes incurred during drying. Immediately after dipping, the top surface of the pristine array began to “bubble” and pop as a result of the densification of CNTs caused by the force of surface tension from water and capillary action from drying. The array self-assembled into a cellular structure made of hollow pores and walls made of densified CNT bundles.

Though considerably more dense than a pristine array, the CVD post-treated sample still exhibited significant physical damage upon wetting. Instead of forming tiny pores, areas of the array consolidated and large cracks formed.

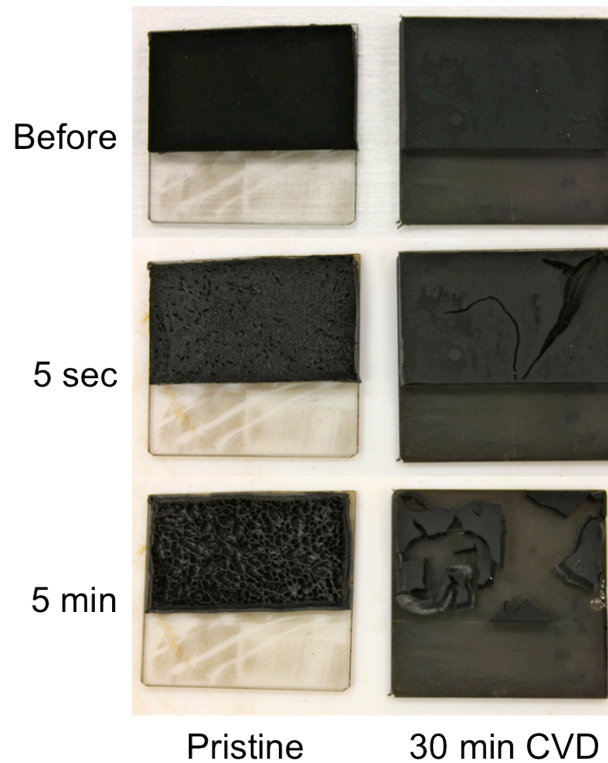


**Figure 5.1** Pristine and CVD post-treated arrays were dipped in pure DI water to show the effects from surface tension and capillary forces on the physical morphology of the sample. Both samples were destroyed by capillary drying forces.

These effects, shown in the following sections, are demonstrated to varying degrees in composite fabrication as a function of amorphous carbon deposition and copper content in the supersaturated solution. Conversely, the array structure can be over-stabilized from extensive amorphous carbon deposition. Treatments exceeding 2 hours resulted in a water-impermeable array, even after intense plasma etching. A cooperative balance of these factors must be found in order to maximize copper content and composite performance.

### 5.3.1 *Effect of Amorphous Carbon Deposition on Composite Fabrication*

Amorphous carbon has an important role in the resultant composite properties and performance. The low-density structure of carbon nanotube arrays makes them highly attractive in composites, but also very fragile. Amorphous carbon deposition has been demonstrated by our lab [121], as a viable method for increasing the compressive strength and recoverability of CNT arrays. It was shown that CNTs undergoing amorphous carbon post-treatment experienced radial diameter growth due to the assembly of additional graphitic walls on the CNT surface. This process also increases surface roughness, decreasing the potential for CNT agglomeration and bundling.

For this thesis, CNT arrays were treated using a procedure adapted for the LP CVD system. Following deposition, the inner and outer quartz tubes of the CVD reactor were coated in an opaque, black film. Analysis of the film's Raman spectrum revealed both amorphous carbon and graphitic signals. The existence of a G peak indicates the presence of  $sp^2$  carbon-carbon bonding. Though the  $G_1/D_1$  ratio was only 1.07 the graphitic nature of the film was confirmed. These results are shown in Figure 5.2.

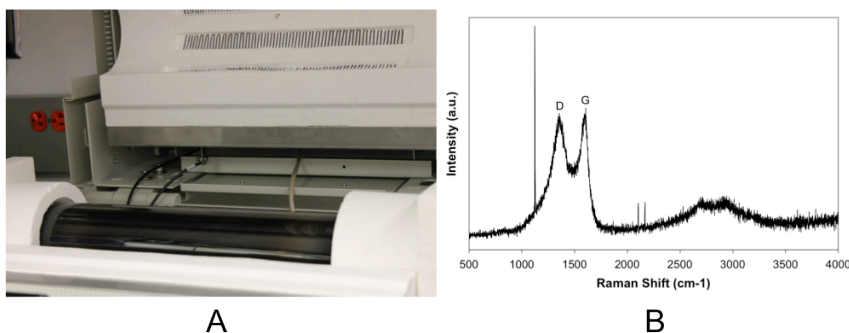


**Figure 5.2** After amorphous carbon CVD an opaque black film formed on the inner and outer tube walls of the LP CVD reactor (A). Analysis of the Raman spectrum of the film scraped from the tube wall revealed the presence of graphitic C-C bonding (B).

To measure the difference in CNT diameter before and after carbon deposition, high-resolution SEM micrographs were analyzed using Image J software. A sample treated for 30 minutes showed an obvious increase in average CNT diameter, from 43.5 to 63.4 nm, as shown in Figure 5.3.

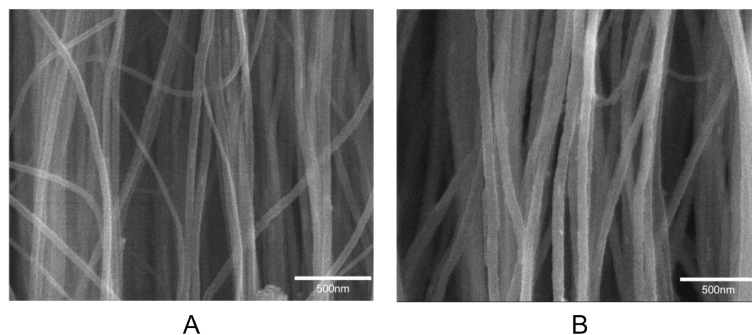


**Figure 5.3** Cross-section SEM micrographs of A) pristine CNT array and, B) CNT array with 30 minutes of CVD amorphous carbon deposition.

Next, various deposition times were tested (A = 60, B = 30, C = 5, and D = 0 minutes) to determine the optimal treatment for composite fabrication. Though highly stable array structures were formed with more extensive deposition times (exceeding 2 hours), the sample was impervious to water infiltration even after intense plasma treatment. Following deposition, the arrays were weighed so mass added and density could be calculated. Figure 5.4 shows the relationship for both values; as deposition time increases, the amount of mass added as well as density increases linearly. Depositing carbon for only 5 minutes yields a notable 6% increase in mass and density. The longest treatment of 60 minutes resulted in nearly two-fold increase in density compared to the pristine array.

The graphitic quality of CVD post-treated arrays was analyzed by comparing the Raman spectra of samples treated for different deposition times. The average graphitic to disorder intensity ratio ( $G_I/D_I$ ), decreased from 1.99 for untreated arrays to 0.96 for arrays deposited with amorphous carbon for 60 minutes. This value is not surprising since the array weight increased by almost 200% due solely to the addition of amorphous carbon in the form of disordered, graphitic walls to the CNTs. This overlay is shown in Figure 5.5.

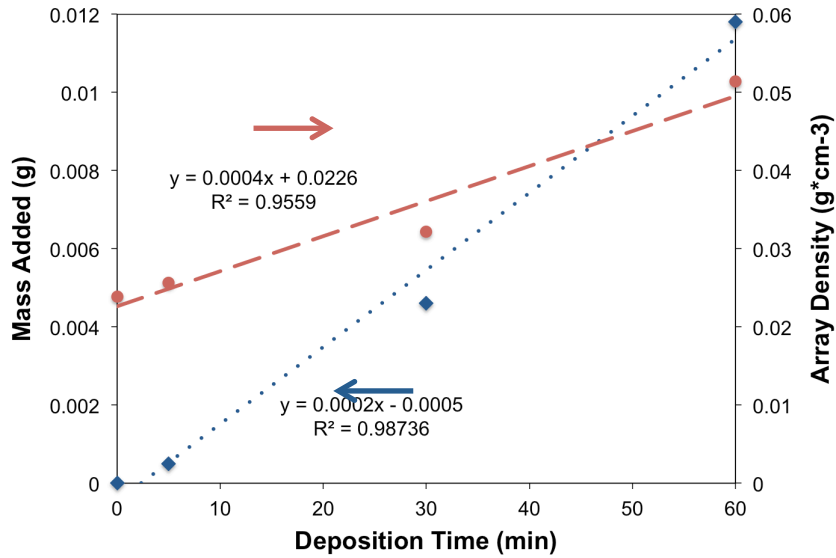


**Figure 5.4** Linear relationships between mass of deposited amorphous carbon (left axis) and array density (right axis) as a function of treatment duration.

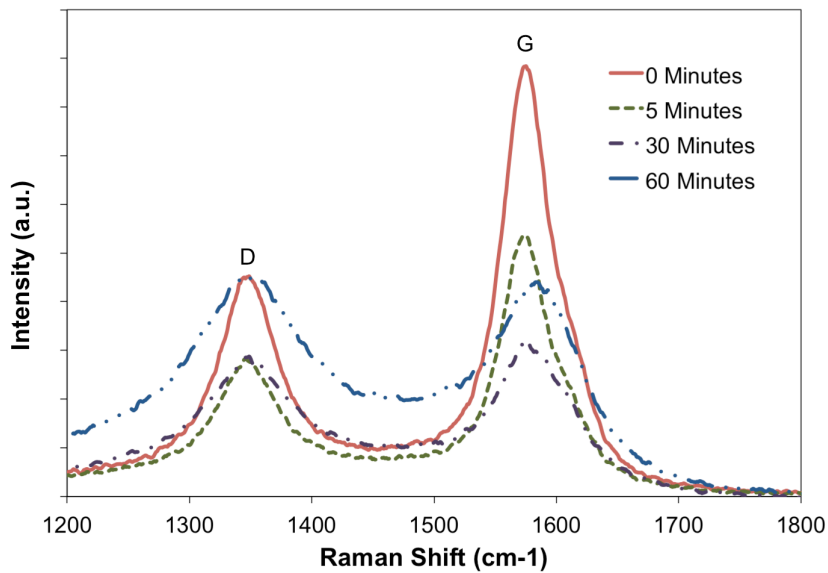


**Figure 5.5** Raman analysis of CNT post-treated arrays as a function of deposition time. The ratio of graphitic signal to disorder ( $G_I/D_I$ ), decreased from 1.99 for a pristine array to 0.97 for an array treated for 60 minutes.

Copper-CNT composites were fabricated with each sample using the modified MLM process to determine the effectiveness in maintaining dimensional stability. Each sample (60, 30, 5 and 0 minutes), was treated with atmospheric plasma for 1 minute to ensure full wetting regardless of CVD treatment. After dipping the arrays in super-saturated copper(II) nitrate aqueous solution, the wet pick-up of the 4 samples differed based on treatment time. Sample B, with 30 minutes of deposition, absorbed the most salt solution (0.6 g) while the pristine array only picked up 0.38 g. The arrays were placed on a hot plate at 50°C so they could slowly dry in atmosphere. Previous experiments using faster drying methods yielded cracked arrays and a high concentration of Cu at the top surface of the array. This was attributed to the rapid movement of uncrystallized solution upward through the array due to capillary action where it then deposited on top of the sample. During slow drying, the arrays treated for 30 and 60 minutes remained stable while the untreated and 5-minute samples cracked to form pores and leached out solution. Figure 5.6 shows the arrays during drying on the hot plate.

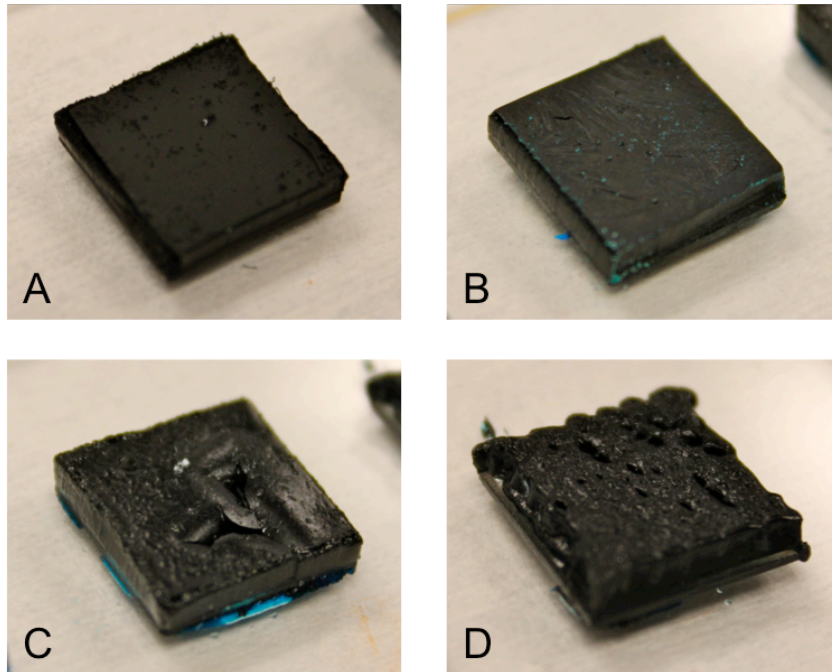


**Figure 5.6** CNT arrays with varying amounts of amorphous carbon deposition: A) 60 min; B) 30 min; C) 5 min and; D) 0 min (pristine array), after dipping in supersaturated copper(II) nitrate - DI water solution.

**Table 5.1** The measured physical properties of CNT-Cu composites during fabrication from copper nitrate solution. Four samples were tested to compare effectiveness of amorphous carbon deposition in maintaining CNT array stability during processing.

Sample	Treatment Time (min)	Array Weight (g)	Initial Density (g/cm <sup>3</sup> )	CVD Weight (g)	Weight Post-CVD (g)	Density Post-CVD (g/cm <sup>3</sup> )	Copper Weight (g)	Composite Density (g/cm <sup>3</sup> )
A	60	0.0062	0.0177	0.0118	0.018	0.0514	0.1053	0.3523
B	30	0.0067	0.0191	0.0046	0.0113	0.0322	0.1307	0.4043
C	5	0.0082	0.0242	0.0005	0.0087	0.0256	0.1175	0.3721
D	0	0.0073	0.0239	0	0.0073	0.0239	0.0748	0.2687

Following dehydration and reduction, Sample A remained the most stable, though the resulting copper content was lower than both Samples B and C. During the reduction step cracks formed in Samples B and C, though more significantly in the latter. This is due to the volume change from recrystallization during the conversion of CuO to Cu. Water vapor is expelled upon reduction, and capillary forces from this expulsion can also cause CNT bundling and array cracking. Images of each composite during the processing steps can be found in Figure 5.7. The weights and densities of the samples during each step of composite fabrication can be found in Table 5.1.

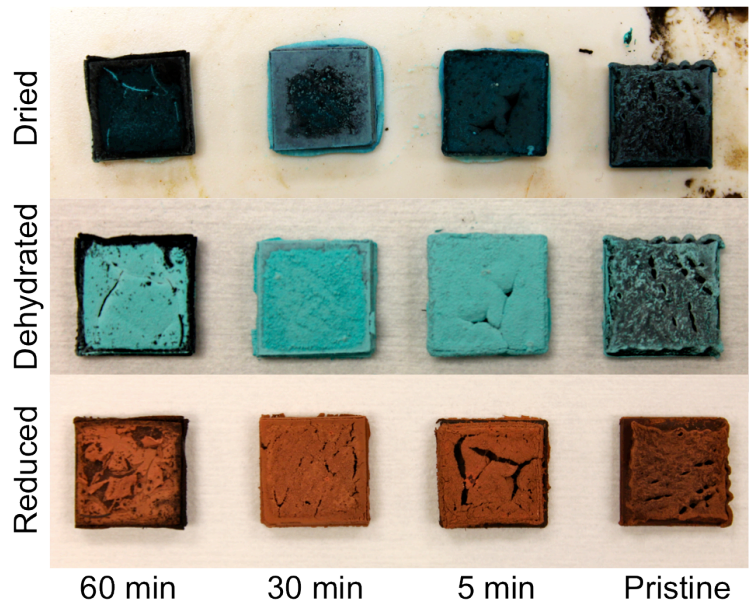


**Figure 5.7** The effect of amorphous carbon deposition is evident throughout all steps of composite fabrication: wetting, drying, dehydration, and reduction.

### 5.3.2 Compression Properties of CVD Post-Treated Arrays and Cu-CNT Composites

Compressive properties of CNT post-treated and Cu-CNT composite arrays were tested on an Instron mechanical tester. Custom platens were designed and fabricated out of aluminum to provide complete, parallel coverage of the entire array. Compressive stress was accordingly calculated based on the array area (13x13 mm). Figure 5.8 shows the platen assembly and mounted array.

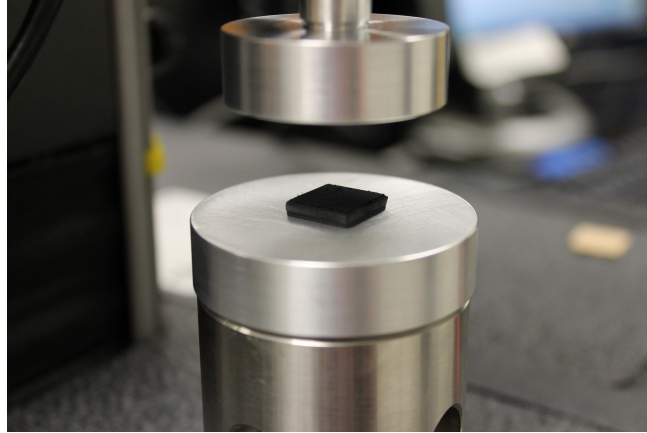


**Figure 5.8** An Instron operating in compression mode was used to measure the mechanical properties of arrays treated with amorphous carbon as well as Cu-CNT composites.

First, the effect of CVD post-treatment to pristine arrays was studied as a function of deposition time. The treatment lengths studied were 0, 5, 30 and 60 minutes. The pristine arrays were grown on 13x13 mm quartz substrates in the same growth run to ensure sample consistency. The arrays were weighed after growth and the baseline density was calculated to be  $0.0235 \text{ g/cm}^3$ . After CVD treatment, the densities of the samples increased linearly with increased treatment times, as shown in Figure 5.9. The individual calculated densities for each sample are shown in Table 5.2.

Before compression, the height of each array was measured by first zeroing the platens and then placing the array on the sample stage. The top platen was slowly lowered until contact was made with the top of the array. The instrument-measured height included the thickness of the quartz substrate, so 1 mm was subtracted from all measurements. Each sample was tested at a compressive load rate of 2 mm/min. Figure 5.10 shows the overlay of compressive stress-strain curves for the four amorphous carbon deposition times tested, both with (B) and without copper (A).

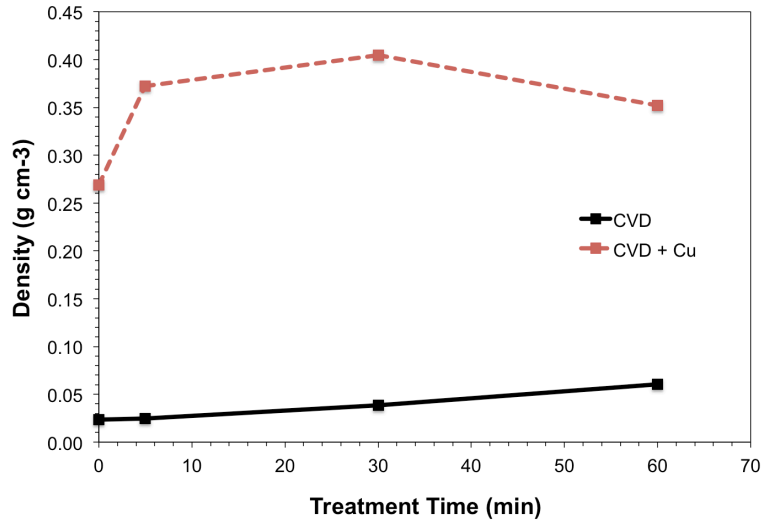


**Figure 5.9** Values for density were calculated based on array volume and weight after CVD treatment and composite fabrication. Array density varied as a function of CVD treatment time and copper content.

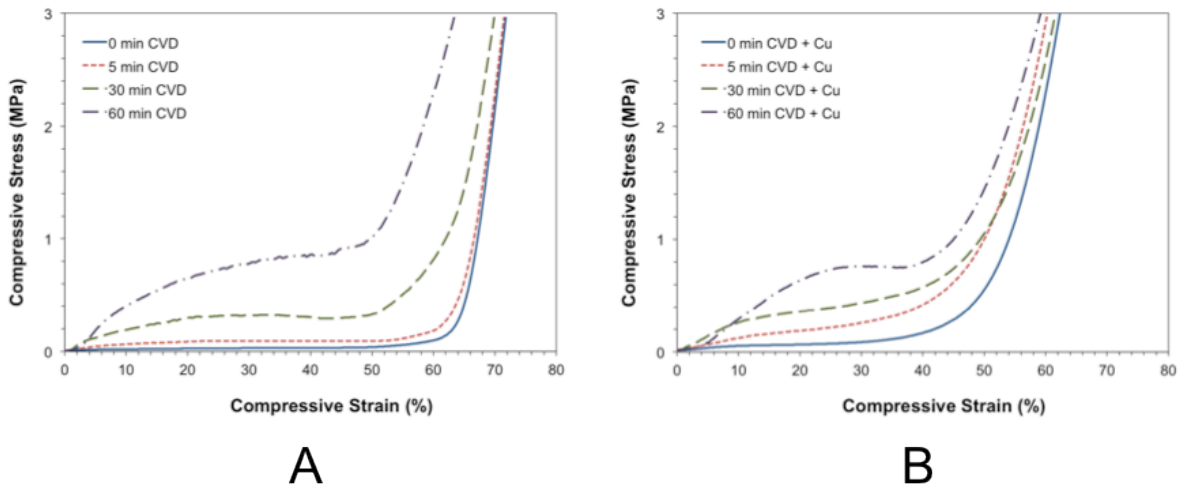


**Figure 5.10** The compression properties of CNT arrays treated were measured as a function of A) amorphous carbon deposition time, and B) combined amorphous carbon deposition and copper content.

The value of compressive stress was determined from the plateau of the compression stress-strain curve. Because the arrays were still mounted on the quartz substrates, a rapid increase in slope is seen where the array becomes fully compressed. The strain value at which this occurs for each sample decreases as a function of deposition time, indicating the filling of free volume in the array by amorphous carbon. Although the maximum compressive stress of the 5 min CVD sample is slightly larger than the pristine sample (0.09 vs. 0.04 MPa), there is a more significant increase seen in arrays treated for longer durations. Arrays treated for 30 and 60 minutes had maximum compressive stress values of 0.32 and 0.85 MPa, respectively. This corresponds to a 20-fold improvement in compressive strength, while also retaining an ultra-low density of 0.06 g/cm<sup>3</sup>. Values for specific stress were also calculated by dividing the maximum compressive stress by the final density of the array. The 60-minute CVD treated sample measured 14.03 MPa/(g/cm<sup>3</sup>), which is competitive with other high performance, low-density foams.

Upon removal of the load, the pristine array exhibited negligible recovery. Samples deposited with amorphous carbon however, exhibited partial (5 min CVD) and full (30 and 60 min CVD), recovery after unloading, a phenomenon that has been seen in previous work in this lab, but achieved using a different deposition method [121]. Interestingly, CNT-Cu composites with more than 5 minutes of CVD treatment also exhibited total recovery after unloading

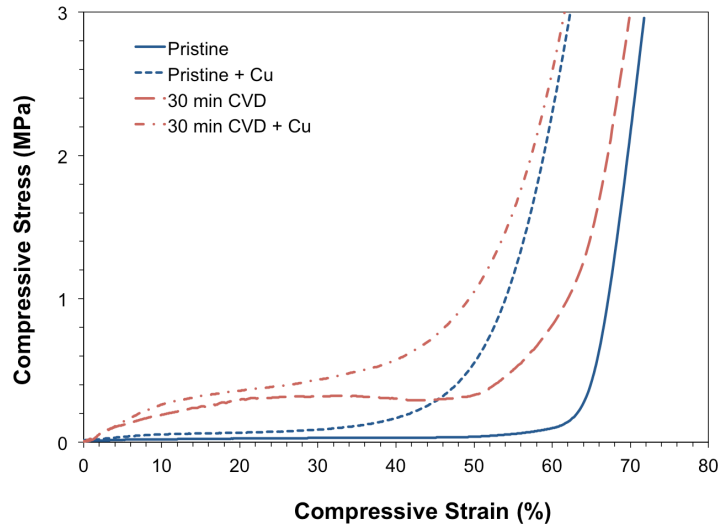
The compressive properties of the CNT-Cu composites were also measured using the same technique. The densities of the resulting composites, shown in Figure 5.9 and Table 5.2, did not follow a similar linear trend as the CVD post-treated arrays, since samples treated for durations greater than 30 minutes did not absorb as much copper salt solution (see Section 5.3.2). Significant improvement of compressive strength was measured for the untreated and 5 min CVD treated composites compared to arrays without Cu, each exhibiting ~3-fold increase. Due to the added mass from Cu however, the specific stress values were actually lower than the CVD treated arrays of the same deposition length. The compressive strength of the 30 min CVD treated composite increased by 66%. Lastly, the maximum stress measured for the composite treated for 60 minutes was actually lower than the array without copper, decreasing from 0.85 to 0.76 MPa. A summary of the densities and compressive strengths of all the samples tested can be found in Table 5.2.

Figure 5.11 shows the compression stress-strain curves for pristine and 30 min CVD post-treated arrays, both with and without copper. The compressive strength of the arrays is enhanced through the addition of Cu, but more significantly so from amorphous carbon deposition. The degree of filling due to copper content is shown by the reduction in final strain for both pristine and 30 min

CVD sample sets. The larger difference in final strain values of the pristine array with and without Cu is indicative of more free volume in the array, and therefore less Cu content. This correlation agrees with the results of Section 2.3.2, which showed that a 30 min CVD treated array added 0.13 g of Cu while a pristine array only added 0.07 g.

**Table 5.2** The density and maximum specific stress were calculate for each CNT array and CNT-Cu composites to determine the affect of amorphous carbon deposition duration.

Sample	Initial Density (g cm-3)	Density Post-CVD (g cm-3)	Composite Density (g cm-3)	Max Stress (MPa)	Max Specific Stress (MPa/g cm-3)
0 min CVD	0.0235	0.0235		0.0428	1.8224
5 min CVD	0.0236	0.0245		0.0947	3.8705
30 min CVD	0.0247	0.0386		0.3212	8.3248
60 min CVD	0.0236	0.0605		0.8493	14.0302
0 min CVD + Cu	0.0239	0.0239	0.2687	0.1882	0.7004
5 min CVD + Cu	0.0242	0.0256	0.3721	0.4020	1.0804
30 min CVD + Cu	0.0191	0.0322	0.4043	0.5335	1.3194
60 min CVD + Cu	0.0177	0.0514	0.3523	0.7616	2.1619

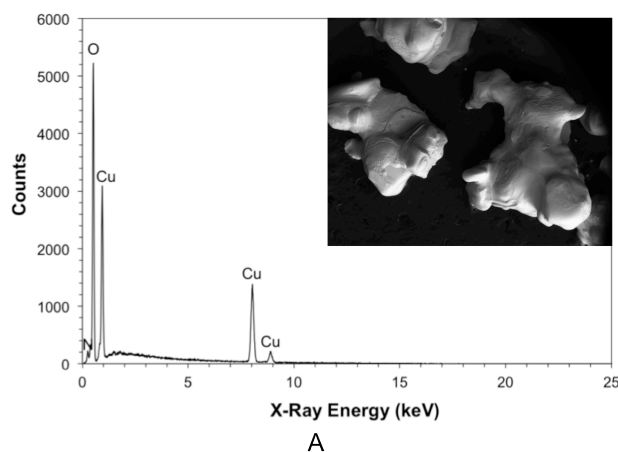


**Figure 5.11** Comparison of compression stress-strain curves for CNT arrays with and without copper and amorphous carbon.

The compression properties of CNT arrays are enhanced through the addition of amorphous carbon via CVD post-treatments. The radial growth of individual CNTs improves their resistance to buckling and bending. At long deposition times, this resistive force can be greater than the van der Waals forces that would normally cause CNT sticking and permanent deformation of the array, as was shown in the compression testing of pristine CNT arrays. The addition of copper nanoparticles is likely to disturb the alignment of CNTs as well as provide sites for stress concentration. This causes premature buckling of the array, especially if the nanoparticles are inhomogeneously distributed in location and size.

### 5.3.3 Chemical Validation of Powdered Salt Reduction to Copper

Before incorporation into the CNT arrays, each copper salt was dissolved, dried, dehydrated and reduced using the proposed procedure. After each step, a small sample of the powder was taken and analyzed using SEM and EDS. Figure 5.12 shows example SEM micrographs and EDS spectra from the different processing states of copper(II) nitrate: hydrated salt, dehydrated salt (copper oxide), and reduced salt (copper). The same data was taken for copper(II) sulfate and copper(II) chloride, and those spectra can be found in Appendix A.



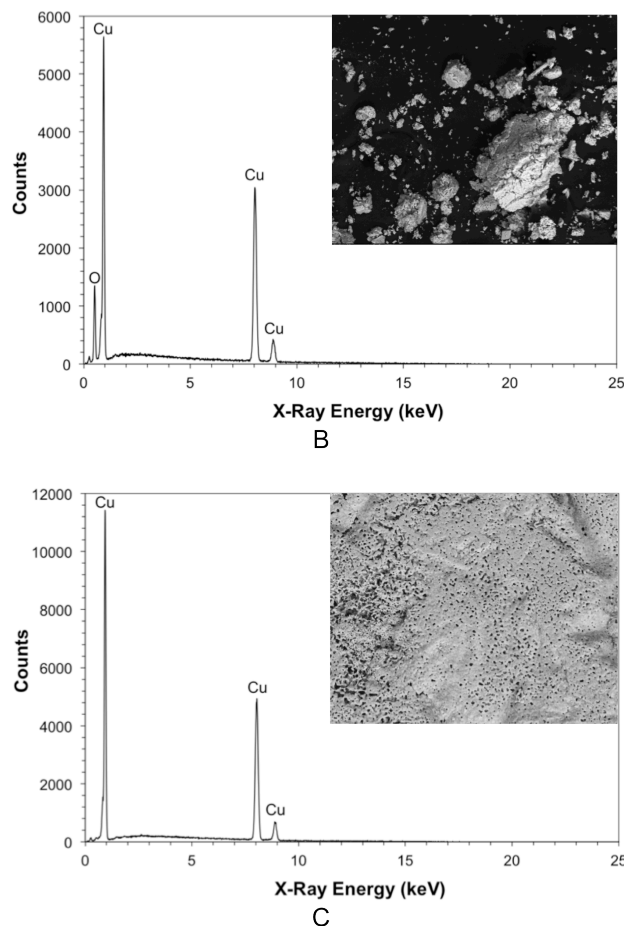


**Figure 5.12** EDS spectra and accompanying SEM micrograph insets for the three processing steps for copper(II) nitrate: A) hydrated salt, B) copper oxide, and C) metallic copper.

### 5.3.4 Copper Content Based on Salt Properties

The resulting copper content in the composites is strongly influenced by the properties of the salt solution. First, the solubility limit of each salt increases with higher solution temperatures. For instance, copper(II) sulfate has a solubility of 18 g/100mL water at 25°C. This value is more than doubled (43.5 g/100 mL water) by increasing the temperature to 100°C. For this reason it is beneficial to prepare super-saturated solutions near boiling.

Additionally, the individual properties of each salt will dictate the maximum solubility at elevated temperature. At 100°C, copper(II) nitrate has the highest solubility (71 g/100 mL water), followed by copper(II) chloride (52.7 g/100 mL water). Secondary factors that govern the density of Cu ions in solution include the size of the ions themselves and their respective charges, the degree of

coordination of Cu ions with ligands, as well as pH. These factors can be confounding and it is difficult to directly elucidate their contribution to final copper content in the composite. To determine the optimal system, composites were fabricated using the modified MLM process with each salt as a precursor.

Based on previous findings, pristine arrays were CVD post-treated for 30 minutes to stabilize the array structure before composite processing. As a result, the few cracks that did develop upon solution infiltration quickly "healed" and closed due to the structural reinforcement provided by the carbon CVD treatment. Figure 5.13 shows digital images of each composite after both drying and reduction processes. Visual differences are apparent among the samples as each salt exhibits its characteristic color upon drying. After reduction, some variance in appearance remains in the resulting copper morphology.

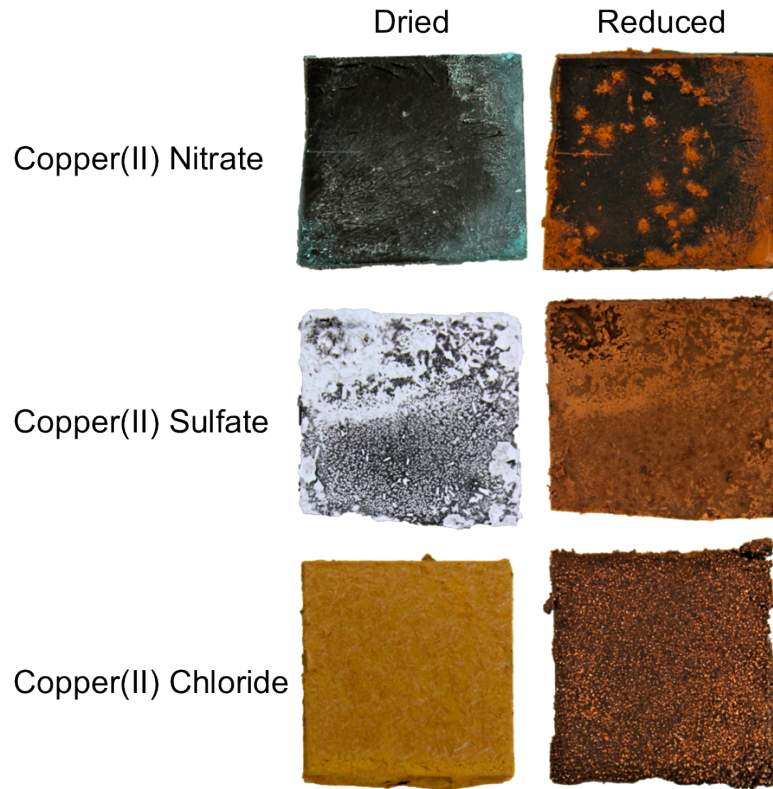


**Figure 5.13** Copper composites were fabricated using a modified molecular level mixing processing route using  $\text{Cu}(\text{NO}_3)_2$ ,  $\text{CuSO}_4$ , and  $\text{CuCl}_2$  as precursors. Images were taken after drying (left), and hydrogen reduction (right).

Similar to the previous experiment in Section 5.3.2, weight measurements were taken throughout the fabrication process to gauge the performance of each salt. The final measured values of copper content were compared against calculated values, which were based on the salt concentration in super-saturated solutions and the wet pick-up of each array. These results can be found in Table 5.3.

**Table 5.3** Measured and calculated values for determination of theoretical and actual copper content based on salt precursor.

Sample	Array + CVD Weight (g)	Wet Pick-Up (g)	Calculated Salt Content (g)	Calculated Cu Content (g)	Measured Cu Content (g)
Copper(II) Nitrate	0.07	1.93	1.37	0.46	0.38
Copper(II) Sulfate	0.07	1.37	0.59	0.24	0.21
Copper(II) Chloride	0.08	1.62	0.85	0.43	0.30

To calculate the copper content based on the wet-pick up of salt solution, knowledge of solution concentration and molar mass of the solute are required. The values used for this thesis are found in Table 5.4. An example calculation for copper(II) nitrate follows.

Solution wet pick-up: 1.93 g

Mass fraction solute in aqueous solution @ 100°C: 0.71

$$\text{Mass solute} = (1.93 \text{ g})(0.71) = 1.37 \text{ g}$$

Molar mass of copper(II) nitrate: 187.55 g mol<sup>-1</sup>

Molar mass of copper: 63.55 g mol<sup>-1</sup>

Molar fraction of copper in copper(II) nitrate: 0.34

$$\text{Mass of copper in infiltrated solute} = (1.37 \text{ g})(0.34) = 0.4659 \text{ g}$$

**Table 5.4** Physical parameters used in copper content calculation.

<b>Salt</b>	<b>Mass Fraction Solute in Aqueous Solution @ 100C</b>	<b>Molar Mass (g/mol)</b>	<b>Mass Fraction Cu</b>
Copper(II) Nitrate	0.71	187.55	0.34
Copper(II) Sulfate	0.44	159.61	0.40
Copper(II) Chloride	0.53	127.68	0.50

Copper(II) nitrate had the highest measured copper content based on the amount of solution-wet pick up. Differing from the calculated value by 0.06 g, or about 13%, there was little loss of salt solution due to leaching or vaporization. The measured and predicted values for copper(II) chloride however, differed by over 30%. This is likely due to its high propensity to thermally degrade to CuCl, which can vaporize at relatively low temperatures. Evidence in support of this is the presence of opaque, white rings, which were left on the ends of the quartz tube after reduction. Even though there was considerable mass loss due to vaporization, copper(II) chloride still provided a higher resulting copper content when compared to copper(II) sulfate. Although the calculated and measured values for content were close, the composite made with copper(II) sulfate precursor resulted in only 0.21 g of copper due to its lower relative solubility.

SEM characterization revealed the microscopic differences between the composites. Composites made from copper nitrate and sulfate retained the stiff, foam-like physical properties of the CNT arrays deposited with amorphous carbon. Slicing the samples with a razor blade was very easy because thin sections cleanly “cracked” and separated from the remaining array. Visually, a red coppery color can be seen throughout the array. Low magnification images of the cross-sections for copper nitrate (inset of Figure 5.14A) and sulfate (inset of Figure 5.15A) showed light and dark contrasting regions dispersed throughout. The areas of contrast in the cross-section are most visible in the copper sulfate composite. Closer inspection revealed that these areas are filled with densely packed copper nanoparticles. The size distribution of the particles reduced from copper nitrate is much smaller. Image B in Figure 5.14 shows CNTs at the top of the composite that are densely and homogeneously “decorated” with Cu nanoparticles. The number of particles found in the copper nitrate sample appeared greater, as should be expected since it contains nearly double the mass of copper contained in the copper sulfate composite. Compared to copper nitrate, composites made from copper sulfate resulted in a much wider size distribution of particles, ranging from a few nanometers to

several microns. It is interesting to compare the Cu particle size in the CNT composites with those of the powders discussed earlier in Section 5.3.3. Even though the powders were solubilized in a supersaturated solution and processed similarly to the composites, the particles within the array are much smaller than the characterized powders. This is likely due to the greatly increased number of nucleation sites provided by the functionalized CNTs.

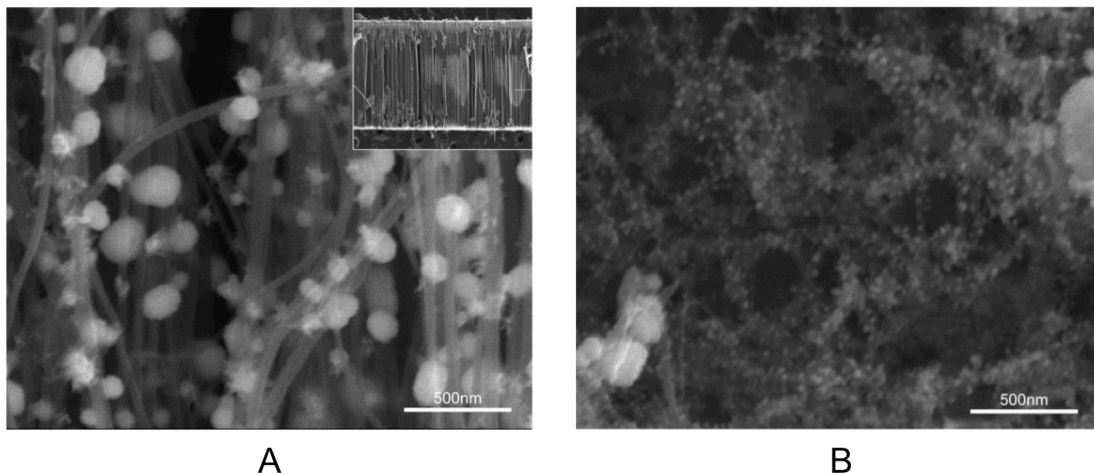


**Figure 5.14** A Cu-CNT composite made from copper(II) nitrate was characterized with SEM. Micrographs show A) cross-section with low magnification inset and; B) top surface.

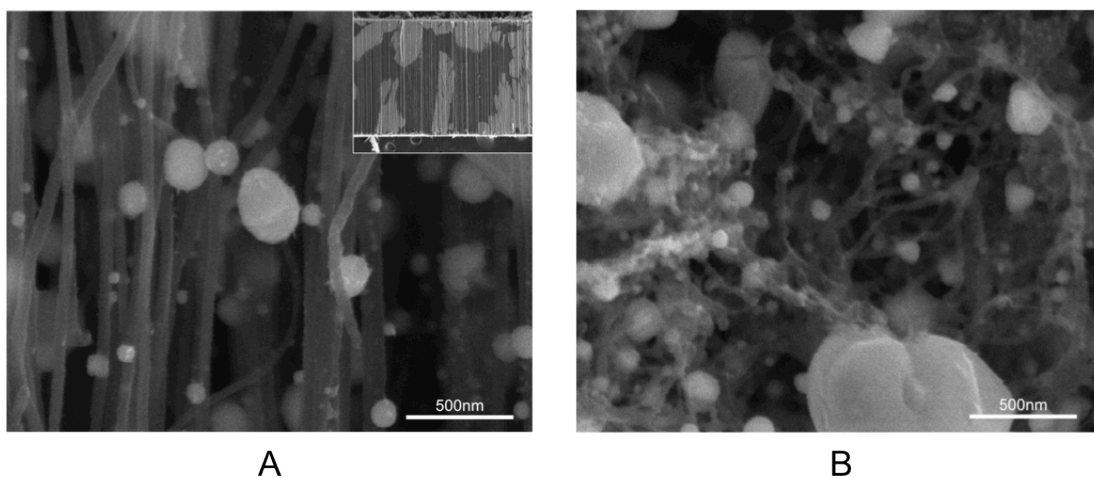


**Figure 5.15** A Cu-CNT composite made from copper(II) sulfate was characterized with SEM. Micrographs show A) cross-section with low magnification inset and; B) top surface.

Composites made from copper chloride were markedly different in appearance as well as mechanical response. As shown in the inset of Figure 5.16A, a clean cross-section was not possible to attain using the same technique as the other two composites. The sample deformed in a highly ductile fashion instead of breaking cleanly.

The high magnification cross-section shows an obvious lack of copper nanoparticles, as was seen in the previously imaged composites. There are areas of brighter contrast on the CNTs themselves and also a few very large copper particles dispersed throughout the array. The relative lack of visible copper was surprising given the large mass (0.3 g) that was added in processing. Image B of Figure 5.16 shows the top surface of the composite. There are several rigid and straight segments of copper that appear to be conformally coating both individual CNTs and also CNT bundles.

Closer analysis of the high magnification images shows additional differences in the CNTs themselves that were not seen in the other composites. Many hollow ends and core-shell structures can be seen, as well as what appears to be “unwrapped” CNTs. These observations are not characteristic of any CNTs seen in these experiments thus far, and therefore warranted additional characterization.

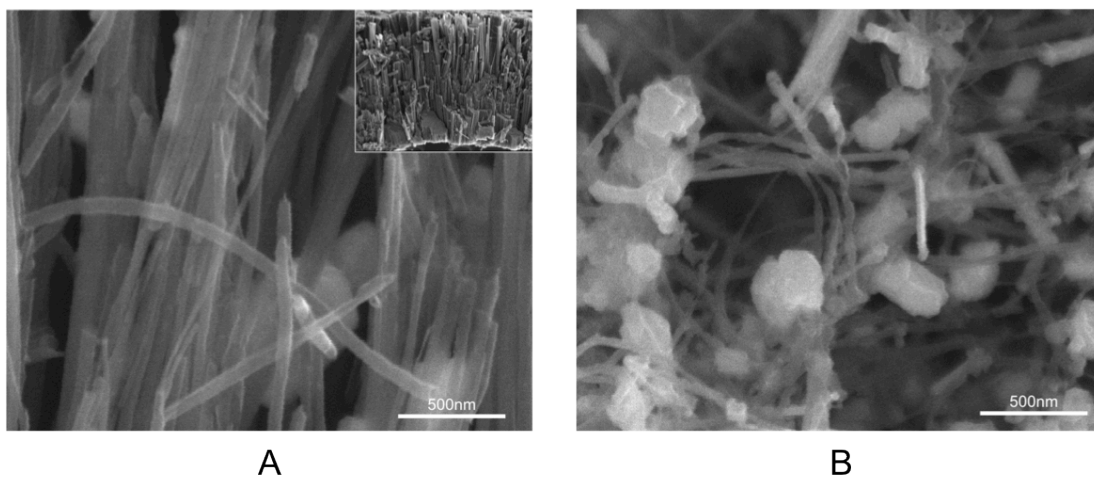


**Figure 5.16** A Cu-CNT composite made from copper(II) chloride was characterized with SEM. Micrographs show A) cross-section with low magnification inset and; B) top surface.

A back-scattered electron (BSE) detector was used to gain visual information about the distribution of copper and CNTs within the reduced copper chloride composite. The evolution of

contrast in BSE detection is purely based on the atomic size ( $Z$ ) of the material in question. Higher  $Z$  elements are physically larger, and therefore probabilistically more likely to participate in elastic collisions with incoming primary electrons from the beam. Bright areas on a BSE image correspond to high  $Z$  elements simply because there is more received signal compared to the few elastic collisions caused by smaller elements. This method provides an easy means for locating high  $Z$  copper within a low  $Z$  carbon background.

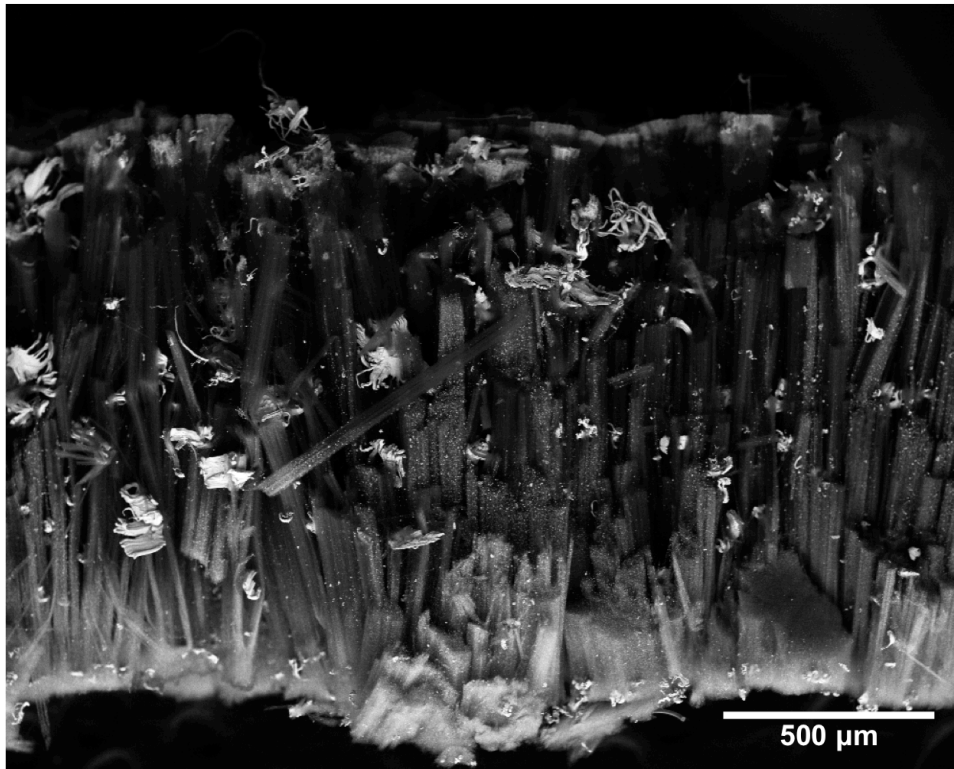


**Figure 5.17** SEM micrograph taken using a back-scattered electron (BSE) detector. Bright areas correspond to high  $Z$  elements (copper), while low contrast corresponds to low  $Z$  elements (carbon).

As can be seen in the low magnification image of the cross section (Figure 5.17), there are indeed concentrated areas of copper near the top and bottom of the array in the form of particles. Additionally, there are large masses of “fibrous” copper that were not originally apparent using only secondary electron (SE) detection. Image A in Figure 5.18 highlights one such area where the

transition between CNT bundle to Cu-coated bundle can be seen. Several smaller coated bundles and CNTs are shown as well.

There is convincing visual evidence that an entirely different mechanism takes place which results in the coating of CNTs and bundles in Cu instead of the particle nucleation seen with copper nitrate and sulfate. Copper chloride compounds have previously been used as precursors for Cu deposition through low pressure CVD, [98], [99] and Atomic Layer Epitaxy (ALE) [97]. These compounds are used because they are able to be vaporized at temperatures as low as 300°C. The opaque, white coating on the inner quartz tube post-reduction was supporting evidence of this in experiments. In the procedure used to fabricate these composites, the tube reactor was pumped to low vacuum, in the mTorr range, before heating. The sample dwells at 185°C for 30 minutes before increasing the temperature to 300°C and introducing hydrogen for reduction. This procedure lends itself to the vaporization and re-deposition of  $\text{CuCl}_2$  throughout the composite, first accumulating on individual CNTs, and at higher concentrations coating entire bundles to make large CNT-Cu structures. As this was an unexpected result, the procedure has not been optimized for preferential deposition and coating of individual CNTs, but preliminary results indicate the potential to do so.

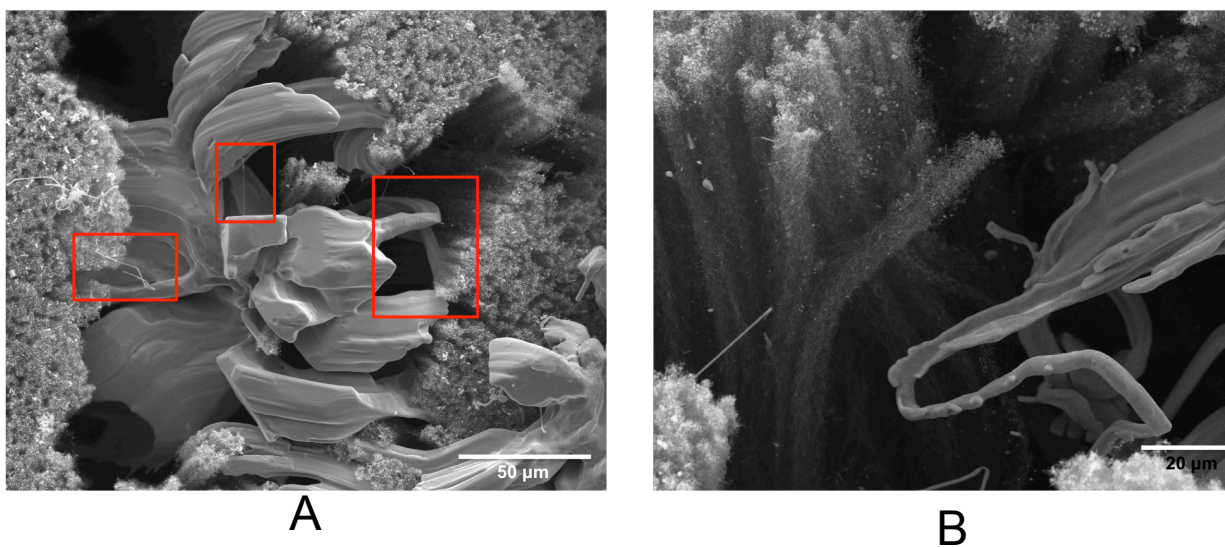


**Figure 5.18** SEM micrographs of A) large copper structure with highlighted areas of copper coated CNTs and CNT bundles, and B) fibrous copper-CNT structures.

Finally, EDS was used to confirm the successful conversion of the salts to metallic copper and also to gauge the distribution throughout each array's cross-section. These results are shown in Figure 5.19. The spectra for all three composites indicated the full conversion of the copper salts to metallic copper, though trace amounts of oxygen were detected in the composite made from copper sulfate. For both copper nitrate (Figure 5.19B), and copper sulfate (Figure 5.19D), there was a higher concentration of Cu at the top and bottom of the cross-section compared to the middle. Because of the randomly distributed light and dark areas that were visible in the cross-sections of these samples (visible in the inset SEM micrographs), the increased detection of Cu merely depended on the selection of probe area. Drawing a straight line from the top to the bottom of either array will yield the sampling of both light and dark areas. The distribution of Cu within the copper chloride-derived composite differed in that the highest copper signal was found at the bottom of the array only. This result agrees with the BSE SEM image taken of the cross-section where the majority of bright area was found at the bottom of the array indicating a relatively high concentration of copper.

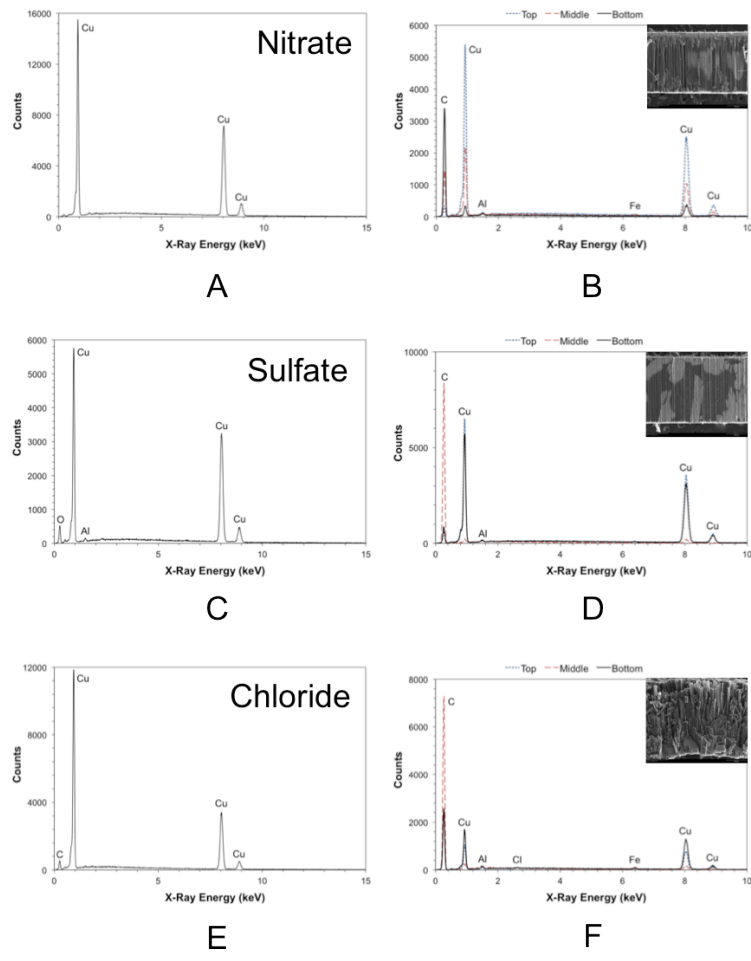


**Figure 5.19** EDS spectra taken from the top surfaces (A, C, E) of each composite (nitrate, sulfate and chloride) were used to confirm the presence of pure copper. Additionally, spectra were taken from the cross-section (B, D, F) at the top, middle and bottom of each sample to probe the relative distribution of copper throughout the thickness of the composite.

## 5.4 Conclusions

Once the CNT arrays were made wettable, it became apparent that measures needed to be taken to provide structural and dimensional stability to prevent array warping and cracking during composite fabrication. Amorphous carbon was shown to deposit conformally on individual CNTs resulting in the radial growth of CNT diameters. This improved the CNT's resistance to buckling and also created a more dense and interconnected array structure. Deposition times of 30 and 60 minutes yielded stable arrays during composite fabrication, but the former was able to take up more copper

solution, resulting in higher copper content. The compressive strength of CVD treated arrays and composites increased with the addition of both amorphous carbon and copper, but the affect of CVD treatment was more prominent. It was also found that arrays and composites that were treated for over 5 minutes exhibited foam-like recovery upon unloading. Finally, fabrication of Cu-CNT composites was successfully achieved using all three salts: copper nitrate, copper sulfate and copper chloride. Super-saturated salt solutions maximized the resulting copper content in the composites, but the highest copper content was achieved using copper nitrate due to its high solubility. SEM characterization of the composites shows a high level of interaction between phases through Cu nanoparticle attachment to the CNT surfaces. In samples made with copper chloride, there was evidence of coated individual CNTs and bundles. Further optimization of either morphology could improve Cu distribution and enhance the interesting mechanical properties for a variety of applications.

## REFERENCES

- [1] E. Esquivel and L. Murr, "A TEM analysis of nanoparticulates in a Polar ice core," *Materials Characterization*, vol. 52, no. 1, pp. 15-25, Mar. 2004.
- [2] L. E. Murr, J. J. Bang, E. V. Esquivel, P. A. Guerrero, and D. A. Lopez, "Carbon nanotubes, nanocrystal forms, and complex nanoparticle aggregates in common fuel-gas combustion sources and the ambient air," *Journal of Nanoparticle Research*, no. 1998, pp. 241-251, 2004.
- [3] L. V. Radushkevich and V. M. Lukyanovich, "Carbon structure formed under thermal decomposition of carbon monoxide on iron," *Soviet Journal of Physical Chemistry*, vol. 26, pp. 88-95, 1952.
- [4] M. Hillert and N. Lange, "The structure of graphite filaments," *Zeitschrift für Kristallographie*, vol. 111, pp. 24-34, 1959.
- [5] M. L. Lieberman, C. R. Hills, and C. J. Miglionico, "Growth of Graphite Filaments," *Carbon*, vol. 9, pp. 633-635, 1971.
- [6] R. T. K. Baker, R. B. Thomas, and R. J. Waite, "Formation of Filamentous Carbon from Iron, Cobalt and Chromium Catalyzed of Acetylene Decomposition," *Journal of Catalysis*, vol. 30, pp. 86-95, 1973.
- [7] S. Iijima, "Helical Microtubules of Graphitic Carbon," *Nature*, vol. 354, 1991.
- [8] W. Marx and A. Barth, "Carbon Nanotubes - A Scientometric Study," *Physica Status Solidi (B)*, vol. 2351, no. 10, pp. 2347 - 2351, 2008.
- [9] M. M. J. Treacy, T. W. Ebbesen, and J. M. Gibson, "Exceptionally high Young's modulus observed for individual carbon nanotubes," *Nature*, vol. 381, no. 6584, pp. 678-680, Jun-1996.
- [10] E. W. Wong, P. E. Sheehan, and C. M. Lieber, "Nanobeam Mechanics: Elasticity, Strength, and Toughness of Nanorods and Nanotubes," *Science*, vol. 277, pp. 1971-1975, Sep. 1997.
- [11] M. F. Yu, O. Lourie, M. J. Dyer, K. Moloni, T. F. Kelly, and R. S. Ruoff, "Strength and Breaking Mechanism of Multiwalled Carbon Nanotubes Under Tensile Load," *Science*, vol. 287, pp. 637-640, Jan. 2000.
- [12] T. W. Ebbesen, H. J. Lezec, H. Hiura, J. W. Bennett, H. F. Ghaemi, and T. Thio, "Electrical conductivity of individual carbon nanotubes," *Nature*, vol. 382, pp. 54-56, Jul. 1996.
- [13] S. J. Tans et al., "Individual single-wall carbon nanotubes as quantum wires," *Nature*, vol. 386, pp. 474-477, 1997.
- [14] J. Hone, M. H. G. Wichmann, C. Piskoti, and a. Zettl, "Thermal conductivity of single-walled carbon nanotubes," *Physical Review B*, vol. 59, no. 4, p. R2514-R2516, Jan. 1999.
- [15] S. Berber, Y. Kwon, and D. Tomanek, "Unusually high thermal conductivity of carbon nanotubes," *Physical review letters*, vol. 84, no. 20, pp. 4613-6, May 2000.

- [16] A. R. Harutyunyan et al., "Preferential growth of single-walled carbon nanotubes with metallic conductivity.," *Science (New York, N.Y.)*, vol. 326, no. 5949, pp. 116-20, Oct. 2009.
- [17] R. M. Sundaram, K. K. K. Koziol, and A. H. Windle, "Continuous Direct Spinning of Fibers of Single-Walled Carbon Nanotubes with Metallic Chirality," *Materials Science*, pp. 1-5, 2011.
- [18] Z. Wang, R. Gao, P. Poncharal, W. de Heer, Z. Dai, and Z. Pan, "Mechanical and electrostatic properties of carbon nanotubes and nanowires," *Materials Science and Engineering: C*, vol. 16, pp. 3-10, Oct. 2001.
- [19] C. F. Powell, J. H. Oxley, and J. M. Blocher, *Vapor Deposition*. New York: John Wiley & Sons, 1966, p. 725.
- [20] M. Chhowalla et al., "Growth process conditions of vertically aligned carbon nanotubes using plasma enhanced chemical vapor deposition," *Journal of Applied Physics*, vol. 90, no. 10, pp. 5308-5317, 2001.
- [21] Y. Y. Wei, G. Eres, V. I. Merkulov, and D. H. Lowndes, "Effect of catalyst film thickness on carbon nanotube growth by selective area chemical vapor deposition," *Applied Physics Letters*, vol. 78, no. 10, pp. 1394-1396, 2001.
- [22] P. E. Nolan, D. C. Lynch, and A. H. Cutler, "Carbon Deposition and Hydrocarbon Formation on Group VIII Metal Catalysts," *Journal of Physical Chemistry B*, vol. 102, no. 98, pp. 4165-4175, 1998.
- [23] H. T. Ng et al., "Growth of Carbon Nanotubes: A Combinatorial Method To Study the Effects of Catalysts and Underlayers," *The Journal of Physical Chemistry B*, vol. 107, no. 33, pp. 8484-8489, Aug. 2003.
- [24] R. Sen, A. Govindaraj, and C. N. R. Rao, "Carbon nanotubes by the metallocene route," *Chemical Physics Letters*, vol. 267, pp. 276-280, 1997.
- [25] K. Kuwana and K. Saito, "Modeling CVD synthesis of carbon nanotubes: Nanoparticle formation from ferrocene," *Carbon*, vol. 43, no. 10, pp. 2088-2095, Aug. 2005.
- [26] G. F. Zou et al., "Highly aligned carbon nanotube forests coated by superconducting NbC.," *Nature communications*, vol. 2, p. 428, Jan. 2011.
- [27] S. Boncel, K. K. K. Koziol, K. Z. Walczak, A. H. Windle, and M. S. P. Shaffer, "Infiltration of highly aligned carbon nanotube arrays with molten polystyrene," *Materials Letters*, vol. 65, no. 14, pp. 2299-2303, Jul. 2011.
- [28] Y. Inoue, K. Kakihata, Y. Hirono, T. Horie, A. Ishida, and H. Mimura, "One-step grown aligned bulk carbon nanotubes by chloride mediated chemical vapor deposition," *Applied Physics Letters*, vol. 92, no. 21, p. 213113, 2008.
- [29] T. Laude et al., "FeCl<sub>2</sub> as catalyst in nanotube CVD synthesis," in *Fullerene-Nanotubes General Symposium*, 2004.

- [30] H. Hou, A. K. Schaper, Z. Jun, F. Weller, and A. Greiner, "Large-Scale Synthesis of Aligned Carbon Nanotubes Using FeCl<sub>3</sub> as Floating Catalyst Precursor," *Chemistry of Materials*, vol. 15, no. 2, pp. 580-585, 2003.
- [31] T. Laude, H. Kuwahara, and K. Sato, "FeCl<sub>2</sub>-CVD production of carbon fibres with graphene layers nearly perpendicular to axis," *Chemical Physics Letters*, vol. 434, no. 1-3, pp. 78-81, Jan. 2007.
- [32] K. Kosugi, M. J. Bushiri, and N. Nishi, "Formation of air stable carbon-skinned iron nanocrystals from FeC<sub>2</sub>," *Applied Physics Letters*, vol. 84, no. 10, p. 1753, 2004.
- [33] V. Jourdain, H. Kanzow, M. Castignolles, A. Loiseau, and P. Bernier, "Sequential Catalytic Growth of Carbon Nanotubes," *Chemical Physics Letters*, vol. 364, pp. 27-33, 2002.
- [34] S. R. Bakshi, D. Lahiri, and A. Agarwal, "Carbon nanotube reinforced metal matrix composites – a review," *International Materials Reviews*, vol. 55, no. 1, pp. 41-64, Jan. 2010.
- [35] H. O. Pierson, *Handbook of Carbon, Graphite, Diamond and Fullerenes: Properties, Processing and Applications*. Park Ridge, NJ: Noyes Publishing, 1993.
- [36] H. O. Pierson, *Handbook of Chemical Vapor Deposition*, 2nd ed. Norwich, NY: Noyes Publishing, 1999.
- [37] E. G. Shafrin and W. A. Zisman, "Constitutive Relations in the Wetting of Low Energy Surfaces and the Theory of the Retraction Method of Preparing Monolayers," *Journal of Physical Chemistry*, vol. 64, pp. 519-524, 1960.
- [38] E. Dujardin, T. W. Ebbesen, H. Hiura, and K. Tanigaki, "Capillarity and Wetting of Carbon Nanotubes," *Science*, vol. 265, no. 5180, pp. 1850-1852, 1994.
- [39] J. P. Tu, Y. Z. Yang, L. Y. Wang, X. C. Ma, and X. B. Zhang, "Tribological properties of carbon-nanotube-reinforced copper composites," *Tribology Letters*, vol. 10, no. 4, pp. 225-228, 2001.
- [40] W. X. Chen, J. P. Tu, L. Y. Wang, H. Y. Gan, Z. D. Xu, and X. B. Zhang, "Tribological application of carbon nanotubes in a metal-based composite coating and composites," *Carbon*, vol. 41, pp. 215-222, 2003.
- [41] S. Dong, J. Tu, and X. Zhang, "An investigation of the sliding wear behavior of Cu-matrix composite reinforced by carbon nanotubes," *Materials Science and Engineering A*, vol. 313, no. 1-2, pp. 83-87, Aug. 2001.
- [42] C. Kim et al., "Strengthening of copper matrix composites by nickel-coated single-walled carbon nanotube reinforcements," *Synthetic Metals*, vol. 159, no. 5-6, pp. 424-429, Mar. 2009.
- [43] K. Kim, S. I. Cha, and S. Hong, "Microstructures and tensile behavior of carbon nanotube reinforced Cu matrix nanocomposites," *Materials Science and Engineering: A*, vol. 430, no. 1-2, pp. 27-33, Aug. 2006.

- [44] H. Li, A. Misra, Y. Zhu, Z. Horita, C. C. Koch, and T. G. Holesinger, "Processing and characterization of nanostructured Cu-carbon nanotube composites," *Materials Science and Engineering: A*, vol. 523, no. 1–2, pp. 60–64, Oct. 2009.
- [45] Q. Ngo et al., "Thermal Interface Properties of Cu-filled Vertically Aligned Carbon Nanofiber Arrays," *Nano Letters*, vol. 4, no. 12, pp. 2403–2407, Dec. 2004.
- [46] Q. Ngo et al., "Thermal Conductivity of Carbon Nanotube Composite Films," *Materials Research Society Symposium*, vol. 812, pp. 1–6, 2004.
- [47] K. Male, S. Hrapovic, Y. Liu, D. Wang, and J. Luong, "Electrochemical detection of carbohydrates using copper nanoparticles and carbon nanotubes," *Analytica Chimica Acta*, vol. 516, no. 1–2, pp. 35–41, Jul. 2004.
- [48] N. Ferrer-Anglada, V. Gomis, Z. El-Hachemi, U. D. Weglikovska, M. Kaempgen, and S. Roth, "Carbon nanotube based composites for electronic applications: CNT-conducting polymers, CNT-Cu," *Physica Status Solidi (a)*, vol. 203, no. 6, pp. 1082–1087, May 2006.
- [49] Y. Chai, K. Zhang, M. Zhang, P. C. H. Chan, and M. M. F. Yuen, "Carbon Nanotube/Copper Composites for Via Filling and Thermal Management," *2007 Proceedings 57th Electronic Components and Technology Conference*, pp. 1224–1229, May 2007.
- [50] Y. L. Yang et al., "Single-walled carbon nanotube-reinforced copper composite coatings prepared by electrodeposition under ultrasonic field," *Materials Letters*, vol. 62, no. 1, pp. 47–50, Jan. 2008.
- [51] Y. Sun and Q. Chen, "Diameter dependent strength of carbon nanotube reinforced composite," *Applied Physics Letters*, vol. 95, no. 2, p. 021901, 2009.
- [52] S. Arai, Y. Suwa, and M. Endo, "Cu/Multiwalled Carbon Nanotube Composite Films Fabricated by Pulse-Reverse Electrodeposition," *Journal of The Electrochemical Society*, vol. 158, no. 2, p. D49, 2011.
- [53] W. M. Daoush, B. K. Lim, C. B. Mo, D. H. Nam, and S. H. Hong, "Electrical and mechanical properties of carbon nanotube reinforced copper nanocomposites fabricated by electroless deposition process," *Materials Science and Engineering: A*, vol. 513–514, pp. 247–253, Jul. 2009.
- [54] S. I. Cha, K. T. Kim, S. N. Arshad, C. B. Mo, and S. H. Hong, "Extraordinary Strengthening Effect of Carbon Nanotubes in Metal-Matrix Nanocomposites Processed by Molecular-Level Mixing," *Advanced Materials*, vol. 17, no. 11, pp. 1377–1381, Jun. 2005.
- [55] K. Kim, S. Cha, and S. Hong, "Hardness and wear resistance of carbon nanotube reinforced Cu matrix nanocomposites," *Materials Science and Engineering: A*, vol. 449–451, pp. 46–50, Mar. 2007.
- [56] L. Xu, X. Chen, W. Pan, W. Li, Z. Yang, and Y. Pu, "Electrostatic-assembly carbon nanotube-implanted copper composite spheres," *Nanotechnology*, vol. 18, pp. 1–4, Oct. 2007.
- [57] K. T. Kim, S. I. Cha, T. Gemming, J. Eckert, and S. H. Hong, "The role of interfacial oxygen atoms in the enhanced mechanical properties of carbon-nanotube-reinforced metal matrix nanocomposites.," *Small*, vol. 4, no. 11, pp. 1936–40, Nov. 2008.

- [58] T. W. Clyne, "A simple development of the shear lag theory appropriate for composites with a relatively small modulus mismatch," *Materials Science and Engineering: A*, vol. 122, no. 2, pp. 183-192, Dec. 1989.
- [59] P. J. Withers, W. M. Stobb, and O. B. Pedersen, "The Application of the Eshelby Method of Internal Stress Determination to Short Fiber Metal Matrix Composites," *Acta Metallurgica*, vol. 37, no. 11, pp. 3061-3084, 1989.
- [60] S. Shenogin, L. Xue, R. Ozisik, P. Keblinski, and D. G. Cahill, "Role of thermal boundary resistance on the heat flow in carbon-nanotube composites," *Journal of Applied Physics*, vol. 95, no. 12, pp. 36-44, 2004.
- [61] A. K. Galwey and M. E. Brown, *Thermal Decomposition of Ionic Solids*. 1999.
- [62] V. K. Van and F. Habashi, "Kinetics of Reduction of Solid Copper Sulphate by Hydrogen and Carbon Monoxide," *The Canadian Journal of Chemical Engineering*, vol. 52, pp. 369-373, 1974.
- [63] F. Habashi and R. Dugdale, "The Reduction of Copper Sulfate and its Application in Hydrometallurgy," *Metallurgical Transactions*, vol. 4, pp. 29-30, 1973.
- [64] F. Habashi and R. Dugdale, "The Reduction of Sulfide Minerals by Hydrogen in the Presence of Lime," *Metallurgical Transactions*, vol. 4, no. 65-71, 1973.
- [65] N. Jacinto, S. N. Sinha, M. Nagamori, and H. Y. Sohn, "An equilibrium study of the hydrogen reduction of copper sulfates," *Metallurgical Transactions B*, vol. 14, no. 1, pp. 136-139, Mar. 1983.
- [66] H. Y. Sohn and S. K. Kim, "Intrinsic kinetics of the hydrogen reduction of copper sulfate: Determination by a nonisothermal technique," *Metallurgical Transactions B*, vol. 16, no. 2, pp. 397-401, Jun. 1985.
- [67] K. Yu and H. Liang, "Attempt at preparing Cu by direct hydrogen reduction of Cu<sub>2</sub>S slurry," *Materials Letters*, vol. 58, no. 24, pp. 3045-3048, Sep. 2004.
- [68] D. W. Lee, G. H. Ha, and B. K. Kim, "Synthesis of Cu-Al<sub>2</sub>O<sub>3</sub> Nano Composite Powder," *Scripta Materialia*, vol. 44, pp. 2137-2140, 2001.
- [69] S. Luidold and H. Antrekowitsch, "Hydrogen as a reducing agent: Thermodynamic possibilities," *Jom*, vol. 59, no. 10, pp. 58-62, Oct. 2007.
- [70] O. Sohnel and P. Novotny, *Densities of Aqueous Solutions of Inorganic Substances*. Amsterdam: Elsevier, 1985.
- [71] *Handbook of Chemistry and Physics*, 90th ed. Cleveland, Ohio: Chemical Rubber Company Press, 2010, p. CH. 8, pp. 122.
- [72] E. M. Crowther and J. R. H. Coutts, "A Discontinuity in the Dehydration of Certain Salt Hydrates," *Proceedings of the Royal Society A: Mathematical, Physical and Engineering Sciences*, vol. 106, no. 736, pp. 215-222, Aug. 1924.

- [73] J. R. H. Coutts, E. M. Crowther, B. a. Keen, and S. Oden, "An Automatic and Continuous Recording Balance. (The Oden-Keen Balance)," *Proceedings of the Royal Society A: Mathematical, Physical and Engineering Sciences*, vol. 106, no. 735, pp. 33-51, Jul. 1924.
- [74] W. E. Garner and M. G. Tanner, "The Dehydration of Copper Sulphate Pentahydrate," *Journal of the Chemical Society (Resumed)*, vol. 0, pp. 47-57, 1930.
- [75] J. Hume and J. Colvin, "The Dehydration of Copper Sulphate Pentahydrate," *Proceedings of the Royal Society A: Mathematical, Physical and Engineering Sciences*, vol. 132, no. 820, pp. 548-560, Aug. 1931.
- [76] H. W. Richardson, "Copper Compounds," *Ullman's Encyclopedia of Industrial Chemistry*, no. Ii. Wiley-VCH Verlag GmbH & Co., pp. 273-301, 2012.
- [77] V. A. J. Hegedus and K. Fukker, "Thermoanalytischer Beitrag zur Zersetzung und Reduktion der Sulfate.," *Zeitschrift für anorganische und allgemeine Chemie*, vol. 284, pp. 20-30, 1956.
- [78] A. K. Vijh, "A thermochemical approach to the gas-phase reduction of metal sulphates," *Journal of Materials Science*, vol. 13, pp. 2413-2417, 1978.
- [79] S. Gordon and C. Campbell, "Differential Thermal Analysis of Inorganic Compounds," *Analytical Chemistry*, vol. 27, no. 7, pp. 1102-1109, 1955.
- [80] T. Cseri, S. Bekassy, G. Kenessey, G. Liptay, and F. Figueras, "Characterization of metal nitrates and clay supported metal nitrates by thermal analysis," *Thermochimica Acta*, vol. 288, pp. 137-154, 1996.
- [81] J. Ghose and A. Kanungo, "Studies on the thermal decomposition of  $\text{Cu}(\text{NO}_3)_2 \cdot 3\text{H}_2\text{O}$ ," *Journal of Thermal Analysis*, vol. 20, pp. 459-462, 1981.
- [82] J. Mu and D. D. Perlmutter, "Thermal decomposition of carbonates, carboxylates, oxalates, acetates, formates, and hydroxides," *Thermochimica Acta*, vol. 49, pp. 207-218, 1981.
- [83] T. J. Taylor, D. Dollimore, and G. A. Gamlen, "Deaquation and denitration studies on copper nitrate trihydrate," *Thermochimica Acta*, vol. 103, pp. 333-340, 1986.
- [84] P. Wang, V. Majidi, and J. a. Holcombe, "Copper atomization mechanisms in graphite furnace atomizers," *Analytical Chemistry*, vol. 61, no. 23, pp. 2652-2658, Dec. 1989.
- [85] B. V. L'vov and A. V. Novichikhin, "Mechanism of thermal decomposition of hydrated copper nitrate in vacuo," *Spectrochimica Acta Part B: Atomic Spectroscopy*, vol. 50, no. 12, pp. 1459-1468, Oct. 1995.
- [86] J. G. Jackson, A. Novichikhin, R. W. Fonseca, and J. a. Holcombe, "Mass spectral studies of thermal decomposition of metal nitrates: an introduction to the discussion of two mechanisms," *Spectrochimica Acta Part B: Atomic Spectroscopy*, vol. 50, no. 12, pp. 1423-1426, Oct. 1995.
- [87] J. G. Jackson, R. W. Fonseca, and J. A. Holcombe, "Mass spectral studies of thermal decomposition of metal nitrates," *Spectrochimica Acta Part B: Atomic Spectroscopy*, vol. 50, no. 12, pp. 1449-1457, 1995.

- [88] I. V. Morozov, K. O. Znamenkov, Y. M. Korenev, and O. a. Shlyakhtin, "Thermal decomposition of  $\text{Cu}(\text{NO}_3)_2 \cdot 3\text{H}_2\text{O}$  at reduced pressures," *Thermochimica Acta*, vol. 403, no. 2, pp. 173-179, Jul. 2003.
- [89] W.-ping Dow, Y.-piao Wang, and T.-jen Huang, "Yttria-Stabilized Zirconia Supported Copper Oxide Catalyst," *Journal of Catalysis*, vol. 160, pp. 155-170, 1996.
- [90] M. Fernandez-Garcia, I. Rodriguez-Ramos, P. Ferreira-Aparicio, and A. Guerrero-Ruiz, "Tracking Down the Reduction Behavior of Copper-on-Alumina Catalysts," *Journal of Catalysis*, vol. 178, pp. 253-263, 1998.
- [91] C. R. A. Wright and A. P. Luff, "Researches on some Points in Chemical Dynamics," *Journal of the Chemical Society*, vol. 33, pp. 1-27, 1878.
- [92] C. R. A. Wright, A. P. Luff, and E. H. Rennie, "Determination of Relations Existing between Rate of Reduction of Copper Oxide by Hydrogen, Time, and Temperature," *Journal of the Chemical Society*, vol. 35, pp. 475-524, 1879.
- [93] R. Pease, "The Reduction of Copper Oxide by Hydrogen," *Journal of the American Chemical Society*, pp. 820-826, 1921.
- [94] J. A. Rodriguez, J. Y. Kim, J. C. Hanson, M. Perez, and A. I. Frenkel, "Reduction of  $\text{CuO}$  in  $\text{H}_2$ : in situ time-resolved XRD studies," *Catalysis Letters*, vol. 85, pp. 247-254, 2003.
- [95] M. A. Mohamed and S. A. Halawy, "Non-Isothermal Kinetic and Thermodynamic Study for the Dehydration of Copper(II) Chloride Dihydrate and Nickel Chloride Hexahydrate," *Journal of Thermal Analysis*, vol. 41, pp. 147-159, 1994.
- [96] H. W. Kohlschütter, "Über den Mechanismus der Haarsilberbildung auf Silbersulfid," *Zeitschrift für Elektrochemie und angewandte physikalische Chemie*, vol. 38, no. 6, pp. 345-353, 1932.
- [97] P. Martensson and J.-O. Carlsson, "Atomic Layer Epitaxy of Copper on Tantalum," *Chemical Vapor Deposition*, vol. 3, no. 1, pp. 45-50, 1997.
- [98] N. Bourhila, N. Thomas, J. Palleau, J. Torres, C. Bernard, and R. Madar, "Thermodynamic and experimental study of Cu-LPCVD by reduction of copper chloride," *Applied Surface Science*, vol. 91, no. 1-4, pp. 175-181, Oct. 1995.
- [99] R. Madar, C. Bernard, J. Palleau, J. Torres, L. M. G. P. E. Bp, and S. Martin, "Thermodynamic analysis of copper CVD using  $\text{CuCl}$  as precursor," *Microelectronic Engineering*, vol. 19, pp. 571-574, 1992.
- [100] A. Marmur, "Wetting on Hydrophobic Rough Surfaces: To Be Heterogeneous or Not To Be?," *Langmuir*, vol. 19, no. 20, pp. 8343-8348, Sep. 2003.
- [101] J. Bico, U. Thiele, and D. Quere, "Wetting of textured surfaces," vol. 206, pp. 41-46, 2002.
- [102] K. K. S. Lau et al., "Superhydrophobic Carbon Nanotube Forests," *Nano Letters*, vol. 3, no. 12, pp. 1701-1705, Dec. 2003.

- [103] R. N. Wenzel, "Resistance of Solid Surfaces to Wetting by Water," *Industrial and Engineering Chemistry*, vol. 28, no. 8, pp. 988-994, 1936.
- [104] A. B. D. Cassie and S. Baxter, "Wettability of Porous Surfaces," *Physics*, no. 5, pp. 546-551, 1944.
- [105] A. Lafuma and D. Quéré, "Superhydrophobic states.," *Nature materials*, vol. 2, no. 7, pp. 457-60, Jul. 2003.
- [106] A. Otten and S. Herminghaus, "How plants keep dry: a physicist's point of view.," *Langmuir : the ACS journal of surfaces and colloids*, vol. 20, no. 6, pp. 2405-8, Mar. 2004.
- [107] D. Xu, H. Liu, L. Yang, and Z. Wang, "Fabrication of superhydrophobic surfaces with non-aligned alkyl-modified multi-wall carbon nanotubes," *Carbon*, vol. 44, no. 15, pp. 3226-3231, Dec. 2006.
- [108] A. Misra, J. Giri, and C. Daraio, "Hydrogen evolution on hydrophobic aligned carbon nanotube arrays.," *ACS nano*, vol. 3, no. 12, pp. 3903-8, Dec. 2009.
- [109] Y. Zhang et al., "A double-layered carbon nanotube array with super-hydrophobicity," *Carbon*, vol. 47, no. 14, pp. 3332-3336, Nov. 2009.
- [110] M. Yu, H. H. Funke, J. L. Falconer, and R. D. Noble, "High density, vertically-aligned carbon nanotube membranes.," *Nano letters*, vol. 9, no. 1, pp. 225-9, Jan. 2009.
- [111] M. Pavese, S. Musso, S. Bianco, M. Giorcelli, and N. Pugno, "An analysis of carbon nanotube structure wettability before and after oxidation treatment," *Journal of Physics: Condensed Matter*, vol. 20, no. 47, p. 474206, Nov. 2008.
- [112] D. Mattia, M. P. Rossi, B. M. Kim, G. Korneva, H. H. Bau, and Y. Gogotsi, "Effect of Graphitization on the Wettability and Electrical Conductivity of CVD-Carbon Nanotubes and Films," *The Journal of Physical Chemistry B*, vol. 110, no. 20, pp. 9850-9855, May 2006.
- [113] A. I. Aria and M. Gharib, "Reversible Tuning of the Wettability of Carbon Nanotube Arrays: The Effect of Ultraviolet/Ozone and Vacuum Pyrolysis Treatments," *Langmuir*, vol. 27, no. 14, pp. 9005-9011, Jul. 2011.
- [114] S. Banerjee and S. S. Wong, "Rational Sidewall Functionalization and Purification of Single-Walled Carbon Nanotubes by Solution-Phase Ozonolysis," *Journal of Physical Chemistry*, vol. 106, pp. 12144-12151, 2002.
- [115] K. S. Han et al., "Atmospheric-pressure plasma treatment to modify hydrogen storage properties of multiwalled carbon nanotubes," *Applied Physics Letters*, vol. 86, no. 26, p. 263105, 2005.
- [116] S. C. Ramos, G. Vasconcelos, E. F. Antunes, a. O. Lobo, V. J. Trava-Airoldi, and E. J. Corat, "Wettability control on vertically-aligned multi-walled carbon nanotube surfaces with oxygen pulsed DC plasma and CO2 laser treatments," *Diamond and Related Materials*, vol. 19, no. 7-9, pp. 752-755, Jul. 2010.

- [117] T. Okpalugo, P. Papakonstantinou, H. Murphy, J. Mclaughlin, and N. Brown, "Oxidative functionalization of carbon nanotubes in atmospheric pressure filamentary dielectric barrier discharge (APDBD)," *Carbon*, vol. 43, no. 14, pp. 2951-2959, Nov. 2005.
- [118] D. K. Owens and R. C. Wendt, "Estimation of the Surface Free Energy of Polymers," *Journal of Applied Polymer Science*, vol. 13, pp. 1741-1747, 1969.
- [119] S. C. Ramos, G. Vasconcelos, E. F. Antunes, a. O. Lobo, V. J. Trava-Airoldi, and E. J. Corat, "Total re-establishment of superhydrophobicity of vertically-aligned carbon nanotubes by Co2 laser treatment," *Surface and Coatings Technology*, vol. 204, no. 18-19, pp. 3073-3077, Jun. 2010.
- [120] X. Bai, D. Li, D. Du, H. Zhang, L. Chen, and J. Liang, "Laser irradiation for purification of aligned carbon nanotube films," *Carbon*, vol. 42, no. 10, pp. 2125-2127, 2004.
- [121] P. D. Bradford, X. Wang, H. Zhao, and Y. T. Zhu, "Tuning the compressive mechanical properties of carbon nanotube foam," *Carbon*, vol. 49, no. 8, pp. 2834-2841, Jul. 2011.
- [122] V. Mittal, *Surface Modification of Nanotube Fillers*. Weinheim: Wiley-VCH Verlag GmbH & Co., 2011.
- [123] A. G. Souza Filho, A. Jorio, G. G. Samsonidze, G. Dresselhaus, R. Saito, and M. S. Dresselhaus, "Raman spectroscopy for probing chemically/physically induced phenomena in carbon nanotubes," *Nanotechnology*, vol. 14, pp. 1130-1139, 2003.
- [124] R. Brukh and S. Mitra, "Kinetics of carbon nanotube oxidation," *Journal of Materials Chemistry*, vol. 17, no. 7, p. 619, 2007.
- [125] R. Viswanath, V. Wakharkar, A. Watwe, and V. Lebonheur, "Thermal Performance Challenges from Silicon to Systems," *Intel Technology Journal*, vol. 3, pp. 1-16, 2000.
- [126] A. Poppe, G. Molnar, and T. Temesvolgyi, "Temperature dependent thermal resistance in power LED assemblies and a way to cope with it," *2010 26th Annual IEEE Semiconductor Thermal Measurement and Management Symposium (SEMI-THERM)*, pp. 283-288, Feb. 2010.
- [127] F. Wu, W. Zhao, S. Yang, and C. Zhang, "Failure modes and failure analysis of white LEDs," *2009 9th International Conference on Electronic Measurement & Instruments*, vol. 4, pp. 978-981, Aug. 2009.
- [128] P. Schelling and P. Keblinski, "Thermal expansion of carbon structures," *Physical Review B*, vol. 68, no. 3, pp. 1-7, Jul. 2003.
- [129] P. Kim, L. Shi, A. Majumdar, and P. McEuen, "Thermal Transport Measurements of Individual Multiwalled Nanotubes," *Physical Review Letters*, vol. 87, no. 21, pp. 19-22, Oct. 2001.
- [130] Y. Gogotsi, *Nanotubes and Nanofibers*. Boca Raton, FL: CRD Press, Taylor & Francis Group, 2006.
- [131] M. J. Biercuk, M. C. Llaguno, M. Radosavljevic, J. K. Hyun, A. T. Johnson, and J. E. Fischer, "Carbon nanotube composites for thermal management," *Applied Physics Letters*, vol. 80, no. 15, pp. 2767-2769, 2002.

- [132] H. Huang, C. H. Liu, Y. Wu, and S. Fan, "Aligned Carbon Nanotube Composite Films for Thermal Management," *Advanced Materials*, vol. 17, no. 13, pp. 1652-1656, Jul. 2005.
- [133] Z. Xu and M. J. Buehler, "Nanoengineering heat transfer performance at carbon nanotube interfaces.," *ACS Nano*, vol. 3, no. 9, pp. 2767-75, Sep. 2009.
- [134] W. Lin, R. Zhang, K.-S. Moon, and C. P. Wong, "Synthesis of High-Quality Vertically Aligned Carbon Nanotubes on Bulk Copper Substrate for Thermal Management," *IEEE Transactions on Advanced Packaging*, vol. 33, no. 2, pp. 370-376, 2010.
- [135] K. Chu et al., "Fabrication and effective thermal conductivity of multi-walled carbon nanotubes reinforced Cu matrix composites for heat sink applications," *Composites Science and Technology*, vol. 70, no. 2, pp. 298-304, Feb. 2010.
- [136] Y. Chai, M. Sun, Z. Xiao, Y. Li, M. I. N. Zhang, and P. C. H. Chan, "Pursuit of Future Interconnect Technology with Aligned Carbon Nanotube Arrays," *IEEE Nanotechnology*, pp. 11-13, 2011.

## APPENDIX

**Appendix A. Chemical structure validation of copper(II) sulfate and copper(II) chloride using Energy Dispersive Spectroscopy (EDS)**

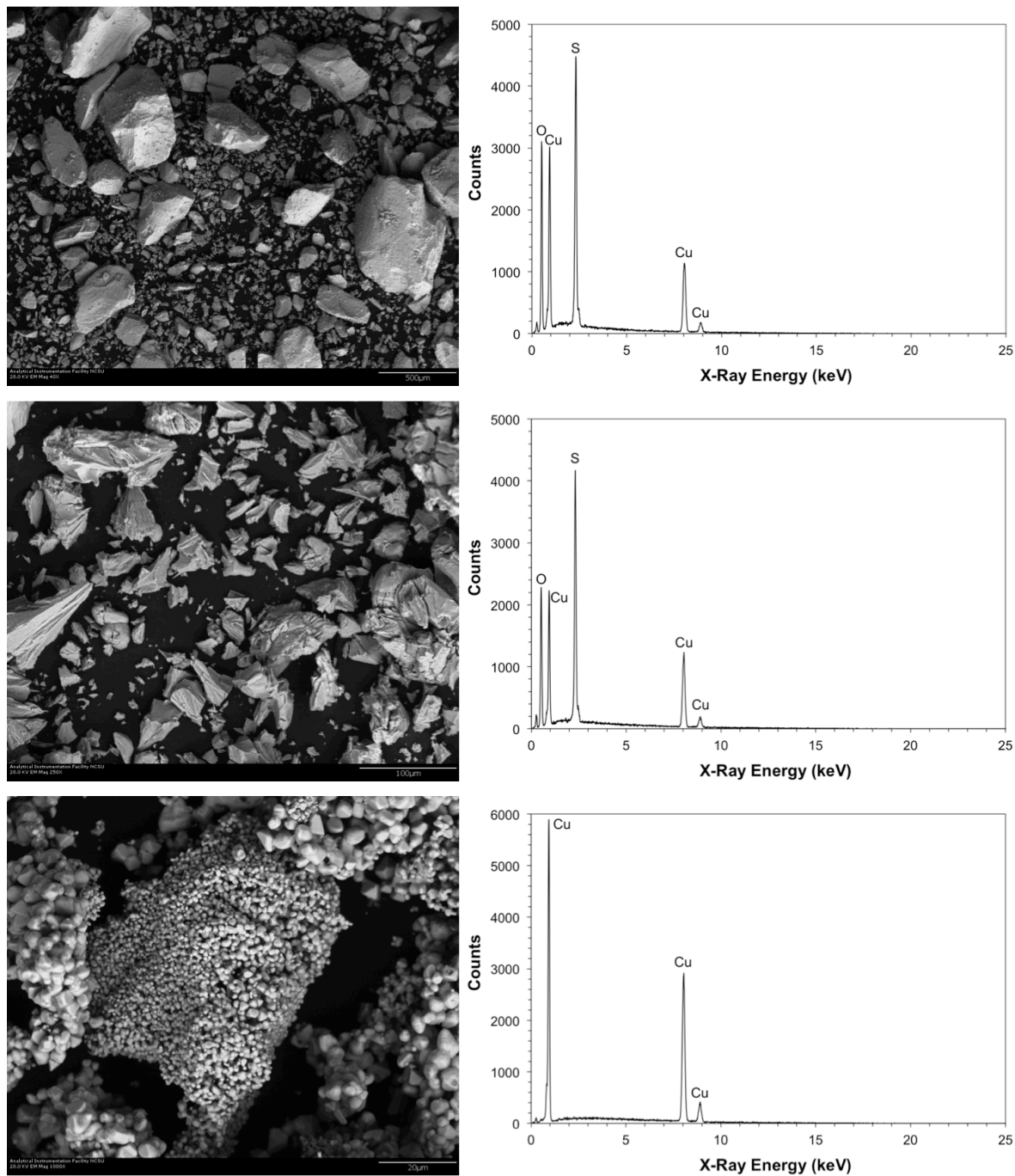


**Figure A.1** SEM micrographs and EDS spectra of copper(II) sulfate powders during the stages of processing: hydrated (top), anhydrous (middle), and metallic copper (bottom). Results confirm total conversion from copper(II) sulfate to pure copper upon reduction.

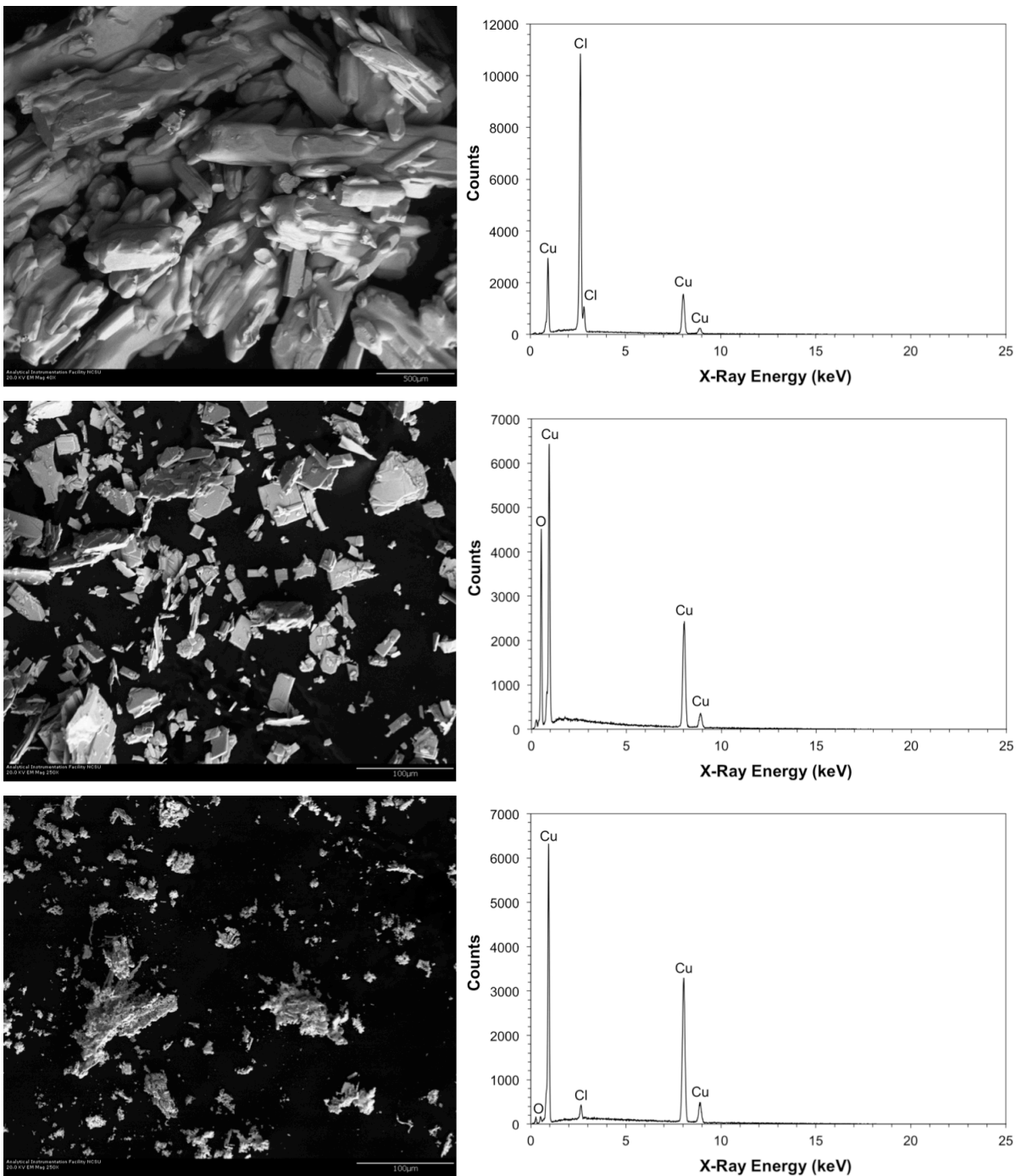


**Figure A.2** SEM micrographs and EDS spectra of copper(II) chloride powders during the stages of processing: hydrated (top), anhydrous (middle), and metallic copper (bottom). Results confirm conversion from copper(II) chloride to pure copper with trace amounts of chlorine and oxygen.